ENABLING WEARABLE HEMODYNAMIC MONITORING USING MULTIMODAL CARDIOMECHANICAL SENSING SYSTEMS

A Dissertation
Presented to
The Academic Faculty

by

Venu G. Ganti

In Partial Fulfillment
of the Requirements for the Degree
Doctor of Philosophy in
Bioengineering

Georgia Institute of Technology
December 2021

ENABLING WEARABLE HEMODYNAMIC MONITORING USING MULTIMODAL CARDIOMECHANICAL SENSING SYSTEMS

Approved by:

Dr. Omer T. Inan, Advisor
School of Electrical and Computer Engineering
Georgia Institute of Technology

Dr. David H. Frakes
School of Biomedical Engineering
Georgia Institute of Technology

Dr. Jin-Oh Hahn
School of Mechanical Engineering
University of Maryland, College Park

Dr. Rishikesan Kamaleswaran
Department of Biomedical Informatics
Georgia Institute of Technology and Emory University

Dr. Animesh Tandon
Department of Pediatric Cardiology
Cleveland Clinic Children's Hospital

Date Approved: December 1, 2021

[To Mom, Dad, and Tej for your unwavering support.]

ACKNOWLEDGEMENTS

The story of my life up till this point has been one of somehow being fortunate enough to be surrounded by such preeminent people whom I manage to absorb a fraction of. Therefore, I would be remiss not to recognize them.

Throughout this arduous journey filled with doubt I am privileged to have had the greatest possible advisor and mentor, Dr. Omer Inan, in my corner for my entire professional career since I was 18 years old. In the fall of 2013, I came to Georgia Tech as a freshman undergraduate electrical engineering major craving real-world experience out of desperation and fear that I would never find my calling. I began researching with Omer a semester later and his boisterous attitude, personable nature, and exciting work led to me becoming engrossed in a field that I have now spent eight years in and hopefully many more to come. Most importantly, in addition to all the free coffee, I can never repay him for introducing me to this fascinating area of research in which not a single day feels like 'work' and through which I can challenge myself daily to improve beyond limits previously unimaginable. I consider you a friend, hope we can continue working together, and will forever miss that loud guffaw and voice echoing through the halls of TSRB.

Thank you to all my committee members: Drs. David Frakes, Rishikesan Kamaleswaran, Jin-Oh Hahn, and Animesh ("Aashoo") Tandon. I am delighted for the opportunity to meet and receive feedback from all of you whose research and vision I admire and level of achievements I aspire to attain. Aashoo, with whom I have had the utmost pleasure of learning from for a considerable part of my doctoral career, I thank

you for your patience, wisdom, and enthusiasm. As a bioengineer, I believe the success of my work lies ultimately in its ability to impact healthcare and improve quality of life. Therefore, the opportunity to work closely with a cardiologist who sees the promise that our work has is priceless, for it convinces me that we are on the right path and allows me to truly understand the clinical problem. I hope we can all work together in the future.

To my other collaborators, Neicey Johnson and Deborah Cherry, I thank you for the invaluable opportunity to work with your nonprofit, Visions, on conducting research in diverse populations, which is important for the translation of this, and all, work. I commend your selflessness, applaud you both for your direct impact on medically underserved populations, and am honored to have been a part of one of your endeavors.

Thank you, Dr. Mozziyar Etemadi, for the opportunity to intern in your lab at Northwestern, that wonderful summer in Chicago at a crossroads during my degree, where I was able to learn an incredible amount despite not producing much output in return. I must thank J. Alex Heller for his incredible patience while getting bombarded with my questions, infinite wisdom, and humor, all while making me feel extremely welcome. Thank you to all the other amazing members of the Etemadi lab and their inspirational work focused on bringing together clinicians and engineers to improve the efficiency of healthcare so doctors can spend more time with their patients—something I deeply resonate with.

To Laura Paige, the best academic advisor I have ever had, and truly the heart and soul of the bioengineering program. I thank you for your endless help, such as calling me

at 9 p.m. the night before my proposal—during recruitment weekend—to make sure I had all the necessary forms, and genuine interest in my achievements.

My fellow IRLers, although Omer is responsible for fostering the fun and collaborative atmosphere within our lab, every single one of you over its entire history—which I am honored to have witnessed till this point—are responsible for maintaining it. To all the incredible more senior graduate students, I thank you for setting wonderful examples of what it takes to perform on a high-level and for your patience in helping me in those early years where I struggled and was less independent. Thank you, Andrew Carek. Thank you, Caitlin Teague. Thank you, Nicholas Bolus. Thank you, Oludotun Ode. Thank you, Sinan Hersek. Thank you, Daniel Whittingslow. Thank you, Hyeon Ki Jeong. Thank you, Samer Mabrouk. Thank you, Jon Zia. Thank you, Nil Gurel. Thank you, Md Mobashir ("Mobasaur") Shandhi. Thank you, Mohsen Safaei. Thank you, Beren Semiz. Thank you, Nordine Sebkhi. Thank you, Brandi Nevius. Thank you, Daniel Hochman. Thanks to the current generation of IRLers, some of whom I do not know as well, but are all entertaining and brilliant: Hewon Jung, Jacob Kimball, Göktuğ Ozmen, Asim ("Gazilla") Gazi, Sungtae An, Kristy Richardson, Sevda Gharehbaghi, David Lin, Arpan Bhavsar, John Berkebile, J. Antonio Sánches-Pérez, Mohammad Nikbakht, Christopher Nichols, Emily Moise, Tamara Lambert, Maddie Miller, Trask Crane, Cem Yaldiz, Farhan Rahman, Afra Nawar, and Thomas Contis. To those of you I mentored, I hope I was able to help in some capacity, whether it be related to technical work or simply through advice on this long degree process. I wish you all the best in your future endeavors and cannot wait to see the incredible achievements you have ahead of you.

As with a lab of our size, and the time I have spent as a member, there are a few people who I need to thank even more. To the first generation of first floor IRLers Andrew, Caitlin, Nick, and Dotun I was fortunate to be surrounded by such talented, disciplined, and hilarious engineers. To Daniel and Hyeon Ki, whom I learned an incredible amount from in my early years. I enjoyed our conversations which kept me alert during our extremely long and secluded cadaver studies, along with the physically demanding exercise of flexing and extending a cadaveric leg. To my African brother, Samer, Visca Barça and thank you for your wisdom, humor, and friendship and for making sure I crossed the finish line, even if at times your constant pestering was a bit much. To the absolute units, Brandi and Göktuğ, I am thankful for their creativity, help, and the countless delusional and delirious hours we spent together as part of a much-needed social time, especially during the pandemic. I must thank Hewon for her creativity, tranquility, and ability to always laugh at my horrible jokes, I hope we can attend many more football games together. Thank you, Jacob, for our discussions on the right path we should take with our research and all the assistance, enthusiasm, and inspirational sticky note advice you brought to work daily. To Asim, the savant whose selflessness and affability is unlike any other, I cherish our many philosophical discussions and I, along with the people at Aviva, cannot wait to see what you have in store. Thank you, Michael, when you arrived on the scene and joined our team, I knew it would be over *Vince Carter motion*. It was an honor being able to work with someone as talented, professional, inquisitive, and friendly as you, even if it was for such a short time. To my superstar undergrad, Adith Srivatsa, just like a little brother I guess you just had to one-up me and join the lab the moment you got onto campus, one semester before

I did. Thank you, for I have learned more from teaching you than you probably learned from me; you'll make an incredible doctor—both kinds. Last, but not least, thank you Andrew for serving as a catalyst in a much-needed time in my degree, setting high expectations, and challenging me daily. It may not have been easy at first to keep up with such a talented engineer, but nothing that amounts to something incredible ever is. I look forward to the opportunity to keep learning from and working with you, as well as our camaraderie and enjoyable nights whether it be at a music festival or coding firmware on a Saturday night, eating Taco Bell, and watching NBA All-Star Weekend.

There is no way that I can express my gratitude for all the amazing friendships I have made throughout these 8.5 years at Georgia Tech and in Atlanta. You incredible people from Smith Hall, Chi Psi, GTRI, GTL, and more are responsible for my well-being and allowed me to relax, smile, and laugh over the years. Thank you for assuring me that my decision to come and stay in this city was the right choice and making this a second home.

Finally, most of all, I would like to thank my family. I want to thank my grandparents who instilled values in me and my parents for upholding those—I hope I can pass them down myself. Thank you, Amma, for being the most inspirational person I know, hearing your voice always calms me down, Nanagaru, for teaching me how to enjoy the simpler things in life and take things in my stride, and to you both for sending me to the best schools possible no matter the hardship. Thank you, Annaya, the smartest person I know, for always testing the waters as the first-born, serving as a role model, and your uplifting encouragement. I hope we can eventually live together again in same city, but most importantly that we never grow apart.

TABLE OF CONTENTS

LIST OF TABLES

LIST OF FIGURES

(LEDs) and MAX86141 analog-front-ends (AFEs), and the ADS1291 ECG AFE. E, Sternum PPG board with three pairs of SFH7060 PDs/LEDs and MAX86140 AFEs. F, Ensemble averaged waveforms from a single 30-second recording. G, Recordings during a 10-minute walk outside where 30-second measurements were taken four times. To take a complete measurement, subjects place a finger or thumb on the wrist electrode. When there is no contact with the electrode and watch is on the wrist, the watch reduces power by lowering the sample rate and only turning on certain sensors.

photoplethysmogram (PPG) sensors. Study protocol tasks in chronological order with duration and mean (SD) of mean arterial pressure (MAP) values for each task. Sample filtered signals from the participant with the lowest signal-to-noise ratio (SNR) signals (n=37): a hypertensive, high BMI, older Black female. In order from top to bottom: electrocardiogram (ECG), SCG, infrared PPG, red PPG, green PPG signals measured from the wearable system (blue) and the synchronized ECG, and arterial blood pressure (ABP) signals measured by the reference system (purple). Systolic blood pressure (SBP; top) and diastolic blood pressure (DBP; bottom) plotted across the full protocol for participant 37, with rest periods (green) and perturbations used to modulate blood pressure (BP) (red) highlighted in chronological order, and the location where the reference finger-cuff continuous BP system was paused during the exercise indicated.

from sensor input to model estimation of stroke volume (SV)—for wearable (blue), demographic (green), and CMR (purple) data.

LIST OF SYMBOLS AND ABBREVIATIONS

ABP   Arterial blood pressure

AFE   Analog front end

AO   Aortic valve opening

BMI   Body mass index

BP   Blood pressure

BPF   Bandpass filter

BSA   Body surface area

CO   Cardiac output

CHD   Congenital heart disease

CMR   Cardiovascular magnetic resonance

CV   Cross-validation

DBP   Diastolic blood pressure

ECG   Electrocardiogram

EF   Ejection fraction

HR   Heart rate

IEEE   Institute for Electronics and Electrical Engineers

IR   Infrared

LCOS   Low cardiac output syndrome

LED   Light-emitting diode

MAD   Mean absolute difference

MAP   Mean arterial pressure

ML   Machine learning

MUA	Medically underserved area
NICCOM	Noninvasive continuous cardiac output monitor
PCC	Pearson correlation coefficient
PCG	Phonocardiogram
PE	Percent error
PEP	Pre-ejection period
PPG	Photoplethysmogram
PTT	Pulse transit time
PWV	Pulse wave velocity
RMSE	Root-mean-square error
SBP	Systolic blood pressure
SCG	Seismocardiogram
SD	Secure digital
SNR	Signal-to-noise ratio
SV	Stroke volume
USB	Universal serial bus
VET	Ventricular ejection time

SUMMARY

Hemodynamic parameters such as blood pressure and stroke volume are instrumental to understanding the pathogenesis of cardiovascular disease. Unfortunately, the monitoring of these hemodynamic parameters is still limited to in-clinic measurements and cumbersome hardware precludes convenient, ubiquitous use. To address this burden, in this work, we explore seismocardiogram-based wearable multimodal sensing techniques to estimate blood pressure and stroke volume. First, the performance of a multimodal, wrist-worn device capable of obtaining noninvasive pulse transit time measurements is used to estimate blood pressure in an unsupervised, at-home setting. Second, the feasibility of this wrist-worn device is comprehensively evaluated in a diverse and medically underserved population over the course of several perturbations used to modulate blood pressure through different pathways. Finally, the ability of wearable signals—acquired from a custom chest-worn biosensor—to noninvasively quantify stroke volume in patients with congenital heart disease is examined in a hospital setting. Collectively, this work demonstrates the advancements necessary towards enabling noninvasive, longitudinal, and accurate measurements of these hemodynamic parameters in remote settings, which offers to improve health equity and disease monitoring in low-resource settings.

CHAPTER 1.   INTRODUCTION

1.1   Motivation

Cardiovascular disease (CVD) is the leading killer worldwide [1]. This comes as no surprise, as the heart is responsible—through phases of electrical conduction, mechanical contraction, and hemodynamic pulsation—for delivering the vital nutrients necessary to sustain life. Fortunately, these essential processes offer a plethora of rich and unique information that can be used to holistically assess cardiovascular health. For example, as illustrated in Figure 1, in disease states (e.g., hypertension and heart failure) these physical mechanisms and downstream hemodynamic parameters—such as blood pressure (BP) and stroke volume (SV)—are disrupted before adverse events ensue [2]. Though these fluctuations can be tracked to diagnose exacerbations in clinical status, current standard of care hinges on the century-old approach of obtaining these infrequent measurements in-clinic. This paradigm of the measurement being anchored to the clinical setting and requiring persons to proactively visit a medical professional to determine their clinical status is unaccommodating, costly, and ineffective [3]–[6]. Hence, we observe remarkable disparities in detection and treatment across socioeconomic status, race, and geographic location: with populations lacking regular access to care having nearly half the awareness of their clinical status and enduring up to quadruple the rates of subsequent cardiac events [7]–[9]. Therefore, technologies enabling frequent, reliable, and accurate measurements of clinical parameters in ambulatory settings promise to reduce the global burden of CVD and offer an opportunity to advance health equity [10], [11]. Leveraging the ubiquity of

1

smartphones and digital health technologies equipped with highly sensitive, miniaturized sensors can prove essential to this remote monitoring movement [12].
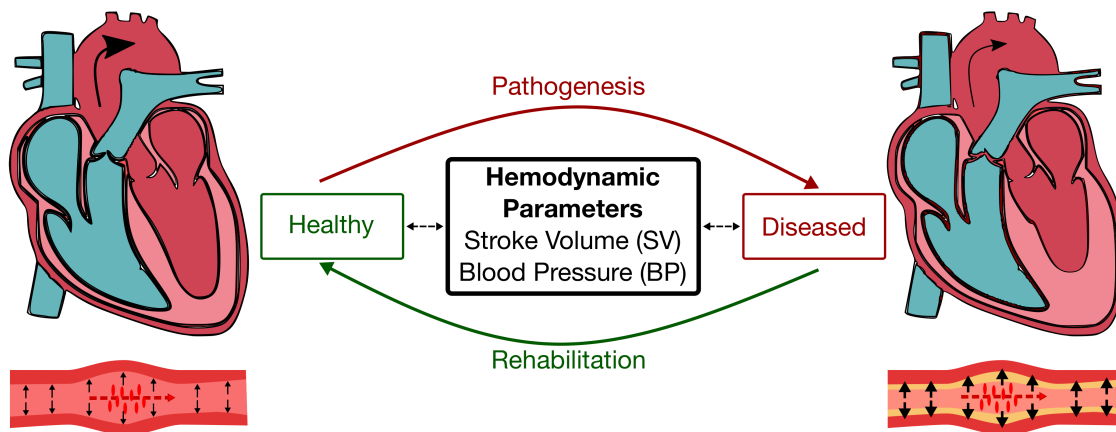
Figure 1. Connection between hemodynamic parameters and cardiac health. Illustration of a healthy (left) versus diseased (right) heart and artery shown with alterations in left ventricle wall thickness and arterial diameter resulting in differences in the stroke volume of blood ejected (SV) by the heart and blood pressure (BP) in the artery.

1.1.1 Blood Pressure Monitoring

Office BP measurements have long been the cornerstone of hypertension diagnosis and management. However, these single-point measurements are susceptible to either appreciable short-term fluctuations in BP or inadvertent errors caused by the measurement setting and procedure (i.e., white-coat hypertension) [4]. Furthermore, the natural variability in daily BP requires an emphasis to be placed on taking multiple measurements, which has been shown to decrease risk, reduce hospitalizations, and improve diagnostic accuracy [13]. Ubiquitous monitoring provides a holistic evaluation that accounts for

organic changes in BP such as sleep, circadian rhythm, stress, nervous system activity, vasomotor tone, physical activity, and time of day [13].

Existing wearable devices that incorporate noninvasive BP methodologies offer an affordable and efficient means to track BP out-of-office [14]. Unfortunately, they commonly employ inconvenient techniques (i.e., oscillometry and tonometry) that demand imparting uncomfortable forces on blood vessels to achieve accurate readings [15]–[17]. These inconveniences fail to empower users to take control of their health, posing a significant challenge towards the widespread routine monitoring of BP. Instead, strategies that compute the pulse transit time (PTT)—a measure of arterial stiffness—present a convenient alternative for BP estimation [18].

The PTT, the time the pressure wave propagates along a length of the arterial tree, is a cuff-less surrogate for BP and can be acquired noninvasively [18]. In practice, to acquire noninvasive PTT requires a combination of sensors—typically either an accelerometer, force sensor, light-emitting diode (LED) and photodiode (PD), electrode, or ultrasonic transceiver—placed proximally and distally along the arterial tree and computed from fiducial points in the captured seismocardiogram (SCG), ballistocardiogram (BCG), photoplethysmogram (PPG), impedance cardiogram (ICG), impedance plethysmogram (IPG), or arterial BP waveform (ABP), respectively [19], [20].

While the main advantage of PTT lies in the ability to conveniently measure BP outside of the office, most studies, including those seen in two recent meta-analyses of PTT-based technologies, limit their analysis to a controlled lab environment and do not explore its feasibility in an at-home setting [14], [18]. Specifically, though most of these studies

3

validate the use of PTT, measurements at-home face additional challenges that may affect accuracy due to the inherent nature of capturing unregulated changes in BP in a completely unsupervised setting.

In addition, despite the inherent convenience of these sensing modalities, they are naturally of concern when used in populations with intrinsic mechanical, optical, and electrical barriers—stemming from higher melanin levels and body fat percentages. To our best knowledge, noninvasive PTT-based BP estimation has yet to be examined in a diverse population—a gap in our scientific understanding that presents a formidable obstacle towards its adoption. Specifically, some medically underserved areas (MUA), which stand to benefit the most from remote monitoring [21], have high Black and Latino populations with higher melanin content and obesity rates compared to Whites [22]. Recent notable data from the Centers for Disease Control and Prevention (CDC) further stress these concerns by exposing that non-Hispanic Blacks not only suffer significantly higher hypertension prevalence than non-Hispanic Whites, but also witness significantly lower hypertension control rates [23], [24]. Affordable remote monitoring options have the responsibility to combat not only social determinants of health, such as access to healthcare and income, but also—in turn—the existing health disparities that are byproducts of them.

As a result, there exists a glaring hole in PTT-based BP monitoring: that this technology has yet to be tested in the settings where, and on the populations for whom—it may be the most valuable. Until addressed, continuing practice of this BP monitoring paradigm will only exacerbate existing health disparities.

1.1.2   Stroke Volume Monitoring

Congenital heart disease (CHD) affects approximately 40,000 births per year in the United States alone, a quarter of whom suffer from critical cases that require surgery or other interventions in the first year of life. Even more disturbingly, only 69% of those presenting with these critical types of CHD reach adulthood [25], [26]. While advancements in cardiac care and surgery have significantly improved the CHD survival rate from a few decades ago, these treatments are not curative by nature. Hence, the growing population of patients with CHD are at high risk of clinical deterioration, either sudden or gradual. Specifically, low cardiac output syndrome (LCOS) is the leading cause of post-CHD surgery death, while the development of heart failure is the leading cause of mortality amongst adult CHD patients [27], [28]. Fortunately, routine assessment of key hemodynamic parameters such as ejection fraction, stroke volume (SV), and cardiac output (CO)—the percentage and volume of blood pumped out by the heart per heartbeat and volume per minute—has been shown to inform prognosis and guide interventions, reducing overall mortality [29]. Since these parameters assess the ability of the heart to pump blood effectively to meet oxygen demand, they are hallmark indicators of left ventricular dysfunction [30] when depressed—a strong predictor of major adverse cardiac events [31]. Thus, the development of technologies allowing continuous, noninvasive, and inexpensive measurement of SV and CO represents a critical need in CHD; such technologies could be used in both inpatient and outpatient settings to improve outcomes.

Existing SV and CO measurement methods are suboptimal, especially in children and those with CHD. Thermodilution-based pulmonary artery catheterization is accurate, but is not commonly used in children due to the large size of catheters and inaccuracies in patients with shunts [32]. Transesophageal Doppler echocardiography is less invasive but

often cannot be used continuously, angle-dependent and therefore less accurate, bulky, and requires a trained professional [33]. Cardiovascular magnetic resonance (CMR) imaging—a noninvasive technique widely considered as the gold standard in children and those with CHD because of high accuracy and excellent reproducibility [34]—is not feasible for continuous SV monitoring because of the inability to be performed at bedside or in the outpatient setting. Therefore, noninvasive continuous CO monitoring (NICCOM) technologies have been developed that estimate SV from models utilizing demographic information combined with either the impedance cardiogram or the finger arterial pressure waveform, obtained through bioimpedance and the vascular unloading technique, respectively [33], [35]–[38]. However, these approaches are obtrusive, require strict placement of multiple electrodes or cuff-sizes, have low accuracy in critically ill patients, and are rarely tested in children so their practicality remains in doubt when used for monitoring SV in patients with CHD [35].

Seismocardiography is a promising method for NICCOM that uses a low-noise accelerometer placed on the chest to capture the SCG, which provides cardiomechanical information unobtainable by other NICCOM methods. When combined with the electrocardiogram (ECG), the SCG allows for the calculation of systolic time intervals—such as the pre-ejection period (PEP) and ventricular ejection time (VET). In recent years, groups have demonstrated that ECG and SCG signals acquired from wearable devices can accurately estimate SV [39], heart failure clinical status [40], and underlying events in the cardiac cycle using echocardiography and CMR [41] in persons with structurally normal hearts. However, SCG signals have not been evaluated in patients with CHD, resulting in lack of understanding in how major anatomical and physiological differences, such as those

present in single-ventricle patients, affect the waveform morphology. Furthermore, the ability of baseline SCG features to accurately assess diagnostic differences in absolute SV across different persons has not been examined. Finally, SCG-based SV estimation has only been studied in comparison to the transesophageal Doppler echocardiogram and therefore never with respect to an unequivocal gold standard measurement such as CMR.

Overall, a convenient wearable biosensor that accurately estimates SV enables remote monitoring of cardiac function and may potentially help identify decompensation in patients with CHD.

In conclusion, these noninvasive sensing methodologies may prove to accurately assess hemodynamic parameters—such as BP and SV—previously buried below the surface of the skin. Finally, the integration of these sensors into wearable multimodal sensing systems offers an interdisciplinary approach to address these multifaceted problems and provide a holistic assessment of cardiovascular health.

1.2   Major Contributions of This Work

The main contributions of this work are given below:

- Designed, optimized, and validated a custom wearable system and associated calibration techniques for feasible and robust cuff-less BP estimation over the course of a day in an unsupervised, at-home setting.
- Evaluated the accuracy and feasibility of the cuff-less BP monitoring system in a medically underserved and predominantly Black population, including participants with a high body mass index and hypertension.

- Demonstrated that seismocardiogram measurements using a wearable device can noninvasively quantify stroke volume in patients with congenital heart disease in a hospital setting.

1.3   Document Organization

The following work is separated into individual chapters, each which expand upon the major contributions listed above. First, background on the most pertinent overlapping cardiovascular physiology and multimodal wearable sensing concepts is provided in CHAPTER 2. Then, in CHAPTER 3 the development and at-home validation of SeismoWatch—a noninvasive, wrist-worn device for estimating BP without a cuff—are covered. Next, CHAPTER 4 concerns the comprehensive in-lab evaluation of SeismoWatch in a racially diverse and high body mass index population—for whom noninvasive sensing using optical and mechanical sensors is of large concern and potentially could provide the greatest value. CHAPTER 5 details the design of a chest-worn wearable biosensor and its ability to noninvasively estimate stroke volume in patients with congenital heart disease. Finally, in CHAPTER 6 we provide the overall conclusion of using multimodal wearable sensing systems to monitor these hemodynamic parameters including both the overarching impacts of this work and suggestions for future efforts which can stem from the advancements made herein.

1.4   Chapter Summaries

CHAPTER 3. This chapter covers the development of our wearable watch-based device ("SeismoWatch") designed to provide convenient, noninvasive, cuff-less blood pressure estimation in an at-home setting. The watch measures single-lead electrocardiogram, tri-

axial seismocardiogram, and multi-wavelength photoplethysmogram signals to compute the pulse transit time, allowing for blood pressure estimation. We sent our custom watch device and an oscillometric blood pressure cuff home with 21 healthy subjects, and captured the natural variability in blood pressure over the course of a 24-hour period. After subject-specific calibration, our noninvasive pulse transit time measurements correlate with around-the-clock blood pressure (Pearson correlation coefficient of 0.69 and root-mean-square error of 2.72 mmHg). Using a novel two-point calibration method, we achieved a root-mean-square error of 3.86 mmHg. We further demonstrated the potential of a semi-globalized adaptive model to reduce calibration requirements.

CHAPTER 4. Using our cuff-less, wrist-worn, pulse transit time–based device ("SeismoWatch") developed in CHAPTER 3, here we present findings on its feasibility when monitoring blood pressure in a diverse population. We recruited a diverse population through a collaborative effort with a nonprofit organization working with medically underserved areas in Georgia. We compared the wearable pulse transit time measurements with those from a finger-cuff continuous blood pressure device over the course of several perturbations used to modulate blood pressure. Our pulse transit time-based wrist-worn device accurately monitored diastolic blood pressure and mean arterial pressure in a diverse population (N=44 participants) with a mean absolute difference of 2.90 mm Hg and 3.39 mm Hg for diastolic blood pressure and mean arterial pressure, respectively, after calibration. We further demonstrate the ability of our device to capture the commonly observed demographic differences in underlying arterial stiffness.

CHAPTER 5. In this chapter, we present the feasibility of multimodal wearable estimation of stroke volume in a diverse congenital heart disease population (N=45 patients). We used

our chest-worn wearable biosensor to measure baseline electrocardiogram and seismocardiogram signals from patients with congenital heart disease, before and after their routine cardiovascular magnetic resonance imaging exam, and derived features from the measured signals, predominantly systolic time intervals, to estimate stroke volume using ridge regression. Wearable signal features achieved accurate stroke volume estimation (28% error with respect to cardiac magnetic resonance imaging) in a held-out test set of patients with congenital heart disease, per CO measurement guidelines, with a root-mean-square error of 11.48 mL and R^2=0.76. Additionally, we observed that using a combination of electrical and cardiomechanical features surpassed the performance of either modality alone. Overall, we observed that using a combination of electrical and cardiomechanical features surpassed the performance of either modality alone.

CHAPTER 2.   GENERAL CONCEPTS

2.1   Cardiovascular Physiology and Hemodynamic Parameters

2.1.1   Blood Pressure

BP represents the pressure exerted by circulating blood on the vessel walls and therefore is an important hemodynamic parameter of both the amount of blood the heart can pump out and the resistance to blood flow in the arteries. Hence, BP is understood to be the product of the volumetric flow rate of blood through the arterial system (i.e., CO) and the resistance to flow exerted on circulating blood by the vasculature (i.e., systemic vascular resistance (SVR)). It can be further dissected into three major components which are the diastolic BP (DBP), systolic BP (SBP), and mean arterial pressure (MAP), shown in Figure 2. Respectively, these components represent the BP during diastole (i.e., when the left ventricle is filling with blood), systole (i.e., when the left ventricle ejects blood into the aorta), and the average BP over a cardiac cycle.
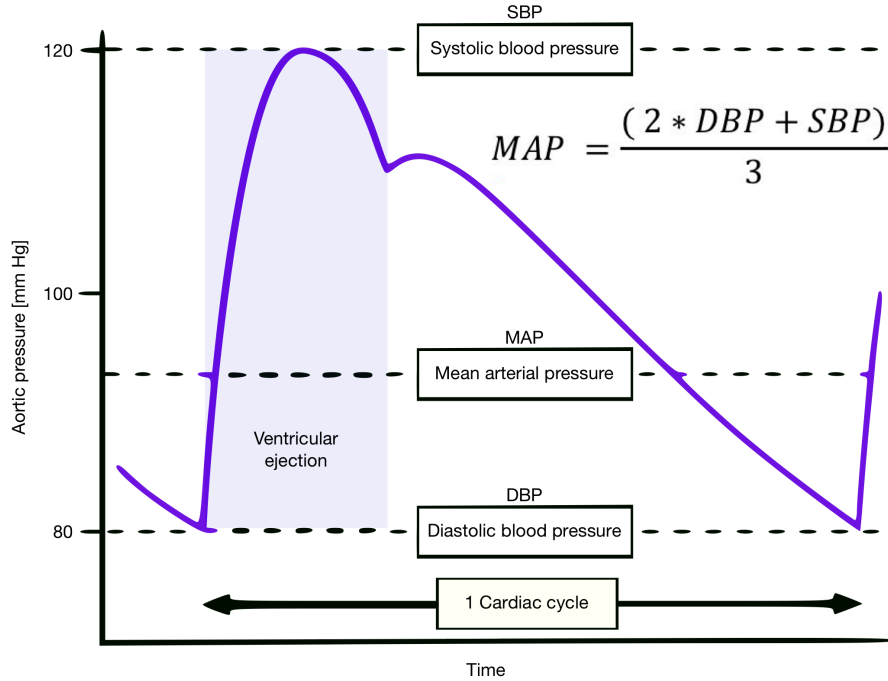
Figure 2. Arterial blood pressure (ABP) diagram. ABP waveform over the duration of one cardiac cycle shown. The three major components of blood pressure (BP) indicated—namely systolic blood pressure (SBP), diastolic blood pressure (DBP), and mean arterial pressure (MAP)—represent the BP when the left ventricle ejects blood into the aorta, is filling following ejection, and the average pressure over the cardiac cycle, respectively. Adapted from [42]**.**

2.1.1.1   Pulse Transit Time and BP Relationship

The PTT is the time it takes for a pressure wave ejected from the left ventricle to propagate along the arterial tree and reflects arterial stiffness. It has been shown to be inversely related to BP through arterial wave propagation models. Mathematically, this relationship is derived from the Moens-Korteweg equation which relates the pulse wave velocity—equivalent to the distance travelled along the arterial tree divided by the PTT—to the arterial wall elasticity. This relationship is shown in Equation 1 below, where the parameters are the Young's modulus (E), vessel wall thickness (h), vessel radius (r), blood density (p), arterial inertance per unit length (L), and compliance (C).

12

$$PWV = \sqrt{\frac{Eh}{rp}} = \frac{1}{\sqrt{L*C}} \qquad (1)$$

The compliance is also inversely related to the pressure (P), as shown in Equation 2 below, where A_m, P_0, and P_1 are subject specific parameters used in physical models to correlate BP to PWV.

$$C(P) = \frac{A_m}{\pi * P_1 \left[1 + \left(\frac{P - P_0}{P_1}^2\right)\right]} \qquad (2)$$

Assuming a constant distance, and substituting Equation 2 into Equation 1, PTT can be modelled to be inversely related to BP, commonly expressed as the formula in Equation 3, where K_1 and K_2 are subject specific parameters related to arterial stiffness and baseline BP, respectively.

$$BP = \frac{K_1}{PTT} + K_2 \qquad (3)$$

As a result, as shown in Figure 3, the PTT can be captured by measuring the pulse wave at two locations along the arterial tree and provides information about arterial stiffness and, by using these equations, also BP. However, though PTT can be used as a surrogate for BP—because several factors can modulate arterial stiffness independently from BP—it is first and foremost a measure of arterial stiffness.
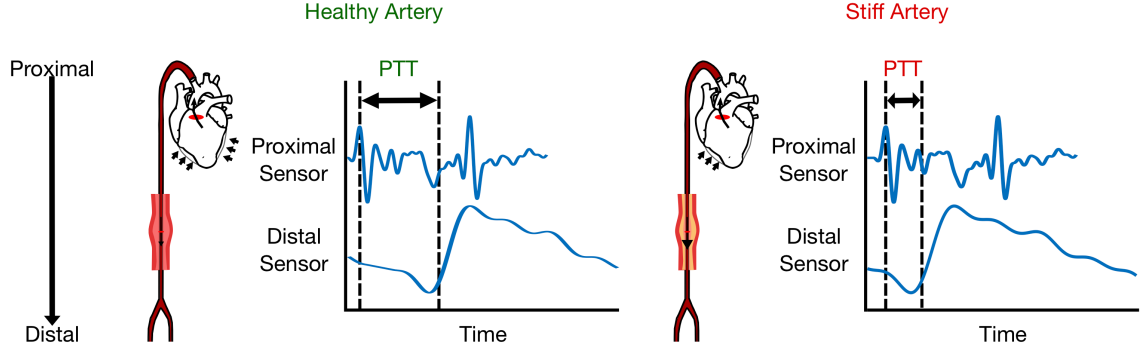
Figure 3. Relationship between pulse transit time (PTT) and arterial stiffness. PTT differences between a healthy and stiff artery captured through two noninvasive sensors placed proximal to and distal from the heart.

2.1.2 Stroke Volume

SV represents the volume ejected by the heart with each heartbeat. Because the heart does not eject its entire volume of blood with each heartbeat the SV can be computed as the difference between the end diastolic volume (EDV) and end systolic volume (ESV), provided in Equation 4.

$$SV = EDV - ESV \tag{4}$$

The percentage of the blood volume ejected to the volume that filled the heart is further quantitatively expressed as the EF, shown in Equation 5.

$$EF = \frac{SV}{EDV} * 100 \tag{5}$$

Furthermore, as given in Equation 6, the product of heart rate (HR) and SV is the CO, related to BP through SVR.

$$CO = SV * HR \tag{6}$$

2.2   Cardiomechanical Biosignals

2.2.1   Seismocardiogram

Seismocardiography, originally used as a means of monitoring the cardiac function of astronauts during the 1960s space programs, involves the simple use of a low-noise accelerometer placed on the chest to capture local cardiac mechanical activity—or a biosignal known as the SCG [19], shown in Figure 4. The SCG is an infrasonic, cardiogenic sternal vibration signal that, in combination with the ECG, contains rich information on systolic time intervals such as the PEP and left ventricular ejection time (LVET). In lieu of the ECG, which alone measures the electrical activity of the heart, the SCG waveform offers a means to assess the vital—and otherwise difficult to obtain—mechanical activity that is traditionally overlooked. In recent years, groups have shown the ability of the SCG signal to assess SV [39], oxygen uptake [43], and heart failure clinical status [40].
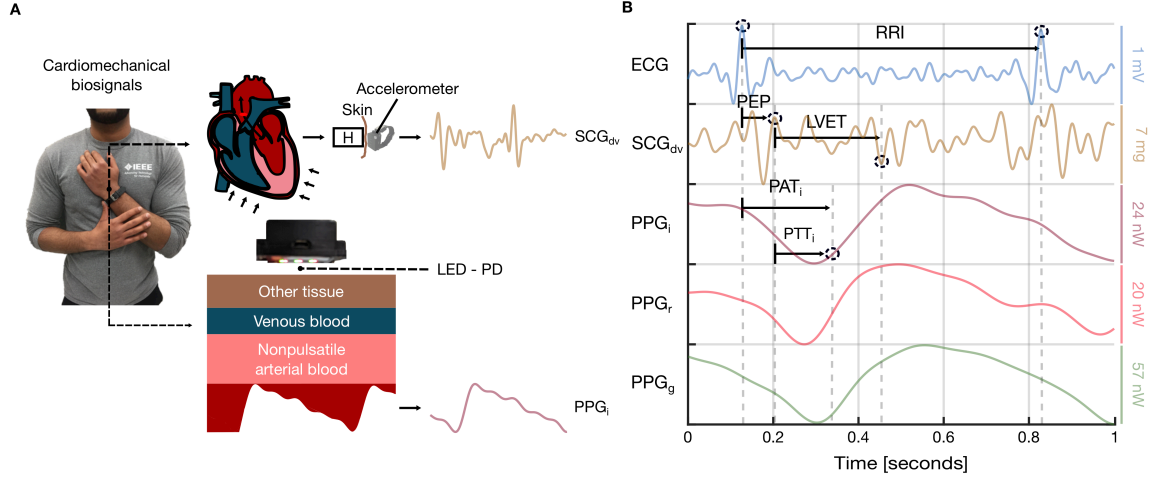
Figure 4. Cardiomechanical biosignals mechanistic overview and key signal features. A, Concept illustration of seismocardiogram (SCG) and photoplethysmogram (PPG) origin, noninvasive acquisition, and resulting signal. B, Wearable biosignals and their pertinent derived systolic time intervals. In order from top to bottom: electrocardiogram (ECG), SCG, infrared PPG, red PPG, green PPG signals measured from our custom wrist-worn wearable system ("SeismoWatch"). Methods for ECG interbeat R-R wave interval (RRI), SCG pre-ejection period (PEP) and left ventricular ejection time (LVET), and PPG pulse arrival time (PAT) and pulse transit time (PTT) feature computations shown.

2.2.2 *Photoplethysmogram*

The PPG is a blood volume per pulse biosignal that is obtained through the use of an LED and an optical sensor, PD. The combination of the LED and PD are used to transmit and receive light—the intensity of which varies corresponding to the periodic changes in blood volume as per the Beer-Lambert law, which relates light attenuation to the material properties of the medium it is propagating through [44]. Hence, the greater the arterial blood volume, the more light absorbed by the blood vessels and the less light intensity measured by the PD. Therefore, the PPG signal is indicative of the small-signal pulsatile changes in arterial blood which are masked by the significantly greater light intensity reflected from components of the tissue, venous blood, and non-pulsatile arterial blood. It

16

can be configured to either be in transmissive or reflective mode depending on whether the LED and PD combination is on the opposite or same side of the vessel being monitored, respectively. Transmissive mode PPGs, despite having greater accuracy and the ability to apply a backing force, are limited to the extremities (i.e., primarily fingers, toes, and earlobes) because of body part thickness and optical wavelength penetration depth. However, reflective PPG can be used to monitor the vasculature at several sites on the body in a more convenient manner. The PPG signal has been used primarily in pulse oximeters for its relationship to peripheral blood oxygen saturation, due to haemoglobin and deoxy-haemoglobin having different absorption and emission spectra at red and infrared (IR) wavelengths, but has now found its use in HR monitoring and BP estimation without the use of a cuff [44].

Collectively, the SCG and PPG represent cardiomechanical signals—due to their ability to capture mechanical activity, whether it be force of cardiac contraction or blood volume—that can provide a holistic assessment of cardiac health by distinctively examining both the function of the "pump" and the "pipes", respectively.

CHAPTER 3.   WEARABLE CUFF-LESS BLOOD PRESSURE

ESTIMATION AT HOME VIA PULSE TRANSIT TIME

3.1   Introduction

Several technologies exist that provide a more complete assessment of BP status, but they each have drawbacks. The most common measurement technique is the oscillometric cuff. Typically, a cuff is placed around the upper arm and its bladder is inflated until it exceeds the SBP. Then the bladder is gradually deflated while the device measures the BP oscillations and computes the SBP, DBP, and MAP. While widely accepted as the gold-standard of at-home BP monitoring, oscillometric cuff measurements are inconvenient, have limited portability, and require the user to follow strict guidelines to obtain an accurate reading. In an effort to decrease obtrusiveness and increase portability wrist-worn devices have been developed (e.g., Omron HeartGuide, Bpro) that currently still use oscillometry or tonometry—both which require imparting forces on the vessel to measure pressure differences—to acquire BP, thereby falling into the same pitfall as their uncomfortable upper-arm counterparts [17]. Therefore, there is a need for a low-user-input, noninvasive device that can perform cuff-less BP monitoring.

Our previous work [45] focused on developing a wearable watch to estimate BP by extracting the PTT: the time it takes for a pulse wave to travel between two distinct locations along the arterial tree, using noninvasive sensors (i.e., an accelerometer and PPG) [18]. Other noninvasive cuff-less wearable watch- based devices currently exist such as Heartisans; however, their ECG-based methods, albeit convenient, technically extract the

pulse arrival time (PAT), which performs poorly as a surrogate for BP when compared to PTT [18]. In addition, our group showed that PTT-based BP estimation significantly outperformed PAT- based BP estimation using an older version of this watch in our previous work [45].

Our group has already shown that PTT can be acquired noninvasively and correlates well to BP in our previous work [45]. However, a significant drawback to the design was the lack of portability. The various sensors in the watch needed to connect to an external analog-front-end (AFE) and a subsequent data acquisition system (DAQ). Consequently, the watch was limited to lab studies, and home monitoring was not practical. To address this limitation, we improved on the design to create a novel and unique combination of off-the-shelf sensors in a robust multimodal, noninvasive, and fully wearable device for obtaining high-fidelity PTT measurements, allowing for low-user-input in an at-home setting. Additionally, our device utilizes data from multiple sensors to trigger different operational modes that preserve battery life and reduce memory requirements from the addition of low-power states. We used the device to obtain multiple PTT measurements for comparison to BP readings from a oscillometric cuff over the course of a 24-hour period at-home. Finally, we present novel and realistic calibration methods for the practical use of this technology in a real-world setting. To the best of our knowledge this represents the first comprehensive assessment of BP estimation noninvasively utilizing PTT in an at-home setting.

3.2   Methods

3.2.1   Hardware Design for Home Monitoring

We adapted the design from our previous work to allow for wearable, at-home monitoring. Though other wearable devices on the market (e.g., Apple Watch and Fitbit) have accelerometers, PPG, ECG sensors, and offer cardiovascular health metrics (i.e., heart rate, oxygen saturation, arrhythmia detection, etc.), they still have yet to demonstrate cuff-less BP monitoring. These devices, compared to the one described in this chapter, lack high-sensitivity multi-wavelength PPG arrays and a low-noise-floor accelerometer that have been essential for our group's ability to obtain high quality signals in our previous works [46], [47].

The design was refined to integrate all sensors with an on-board microcontroller inside a small main watch body (27.5 × 27.5 × 16.1 mm), removing any need for external components and making the watch truly portable. Additionally, to allow for further assessment of cardiac health, we included an ECG, sternum PPG sensors, a gyroscope, and environmental sensors. The ECG sensor allows for easy partitioning of the heartbeats and can be used to assess the heart rate variability (HRV) to provide insight into autonomic state [48]. To capture sternum PPG, we placed three additional PPG sensors on the top side of the watch to measure the sternum's pulse wave while the user performs the same maneuver needed to capture the SCG, as detailed in our previous work [45]. The sternum PPGs will provide an additional timing reference for PTT calculations. We included a gyroscope to sense the gyrocardiogram (GCG) signal. Previous work noted a reduced error when using the GCG in combination with SCG to predict the PEP [49]. The environmental sensor measures the temperature, relative humidity (RH), and barometric pressure, adding an aspect of activity context for improved physiological interpretations.

The complete design features three stacked printed circuit boards (PCBs) and a 150 mAh lithium-ion battery (Adafruit Industries, New York City, NY, USA) inside of a custom 3D printed case. From the backside of the watch—closer to the wrist when worn—to the topside, the boards and battery are stacked in the following order (Figure 5B): wrist PPG/ECG board, main board, battery, and finally, sternum PPG board. The case includes three slots on both the top and bottom portion to expose the PPG sensors.
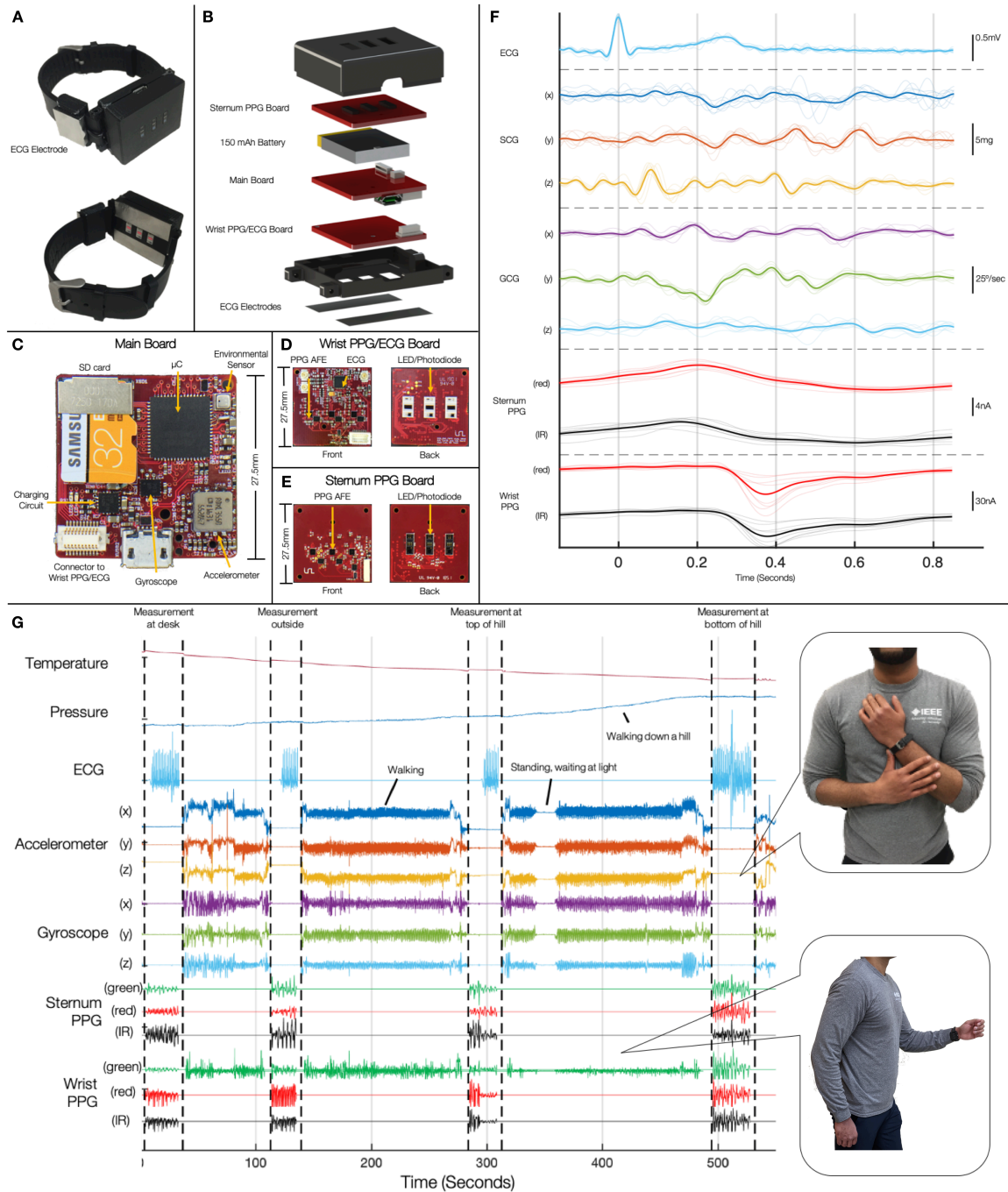
Figure 5. A, SeismoWatch 2.0. B, The inside of the watch contains three printed circuit boards (PCBs) and a 150 mAh lithium-ion battery. A stack connector connects the main board to the wrist PPG/ECG board. The sternum PPG board and the wrist PPG/ECG board snap into the 3D printed case. Stainless steel electrodes placed on the back of the watch and the wristband allow for ECG measurements. C, Main board that includes the ATSAM4LS8B microcontroller, ADXL355 accelerometer, BMG250 gyroscope, BME280 environmental sensor, SD card,

charging circuit, and connectors to the daughter boards. An on-board micro-USB port allows for data transfer and battery charging. D, The wrist PPG/ECG board with three pairs of SFH7072 photodiodes (PDs)/light-emitting diodes (LEDs) and MAX86141 analog-front-ends (AFEs), and the ADS1291 ECG AFE. E, Sternum PPG board with three pairs of SFH7060 PDs/LEDs and MAX86140 AFEs. F, Ensemble averaged waveforms from a single 30-second recording. G, Recordings during a 10-minute walk outside where 30-second measurements were taken four times. To take a complete measurement, subjects place a finger or thumb on the wrist electrode. When there is no contact with the electrode and watch is on the wrist, the watch reduces power by lowering the sample rate and only turning on certain sensors.

For the microcontroller, we selected the ATSAM4LS8B (Microchip Technology, Chandler, AZ, USA) for its large amount of storage (512kBytes Flash, 64kBytes RAM), high number of peripheral options (48 GPIOs, 4 USART), and ultra-low power consumption (1.5 µA sleep mode). We removed the custom AFEs used in the previous iteration and selected sensors with internal AFEs to reduce the number of components and power consumption. Additionally, we decided to not use on-board analog-to-digital converters (ADCs) due to the relatively high noise and low bit conversion compared to external ADCs. Instead, we selected sensors that included an integrated ADC. This allowed for a completely digital interface and allowed the sensors to independently make conversions, freeing up processor time on the microcontroller.

The various components on each of the boards can be seen in Figure 5(C/D/E). Table 1 details the system specifications including the sample rate for each sensor. The main board contains most of the watch hardware: the microcontroller, charging circuit, accelerometer, gyroscope, environmental sensor, secure digital (SD) card, and various connectors to the other components. For the accelerometer, we selected the ADXL355 (Analog Devices Inc., Norwood, MA, USA) that has a noise floor at 25 µg/Hz and resolution of 0.003 mV/bit. This high-resolution, low-noise accelerometer is needed to

accurately measure the SCG, which can have a peak-to-peak amplitude of as low as approximately 8 mg. To measure the GCG, we chose the BMG250 (Bosch, Gerlingen, Germany) due to the low output noise (0.007 °/s/√Hz). The main board also includes the BME280 (Bosch, Gerlingen, Germany) that features a small package size (2.5 × 2.5 mm), low current consumption (3.6 µA), and a low noise floor pressure sensor (0.2 Pa RMS). The microcontroller stores data on an on-board SD card at a write speed of 12 Mb/s.

The wrist PPG/ECG board, as the name implies, contains both the wrist PPG and ECG circuit. On the back side of the board are three SFH7072s (Osram, Munich, Germany) with each containing a green, red, and infrared (IR) LED and two photodiodes (PDs). One of the PDs blocks red and IR wavelengths, improving the detection of a green wavelength, while the second more broadband PD has a peak sensitivity around the red and IR wavelength. Measurements of PTT would utilize the red and IR detectors to monitor the deeper arteries. The high signal-to-noise ratio (SNR) green detector could constantly measure heart rate when the user is not taking a PTT measurement and indicate physiological states between PTT measurements. Each SFH7072 interfaces with a MAX86141 (Maxim Integrated, San Jose, CA) to drive the LEDs and to read the current output of the PDs. This board also includes the ECG circuitry where we selected the ADS1291 (Texas Instruments, Dallas, TX) due to the low-noise (8 µVpp) and high-resolution ADC (24 bit). The ADS1291 connects to three dry stainless-steel electrodes. For the negative reference and the right leg drive, two electrodes are placed on the back- side of the watch to make contact with the wrist. We placed a third electrode for the positive reference on the outside of the wristband. Using the ADS1291's lead-off detection feature,

which constantly monitors the connection to the body, the user can initiate a measurement by simply touching the wristband electrode with the opposite hand.

Table 1. Device specifications

Parameter	Value		
	PTT measurement mode	Continuous mode	Standby mode
Data storage capacity		(Depends on μSD card size)	
Power consumption	19 mA	5 mA	4 mA
Battery life (based on 150mAh battery)	8 hrs	30 hrs	38 hrs
Physiological measurements			
ECG (single-lead)			
Bandwidth	125 Hz	-[a]	-
Noise	8 μVpp	-	-
Sample rate	1 kHz	-	-
Accelerometer (3-axis)			
Bandwidth	125 Hz	31.25 Hz	-
Noise	25 μg/$\sqrt{Hz}$	25 μg/$\sqrt{Hz}$	-
Sample rate	500 Hz	125 Hz	-
Gyroscope (3-axis)			
Bandwidth	125 Hz	25 Hz	-
Noise	0.007 º/s/$\sqrt{Hz}$	0.007 º/s/$\sqrt{Hz}$	-
Sample rate	500 Hz	125 Hz	-
Sternum PPG (Green, Red, IR)			
Wavelength (λ_{peak})	530, 660, 950 nm	-, -, -	-, -, -
Spectral sensitivity	0.27, 0.47, 0.77 A/W	-, -, -	-, -, -
Radiant sensitive area	1.3 x 1.3 mm	-, -, -	-, -, -
Sample rate	333, 333, 333 Hz	-, -, -	-, -, -
Wrist PPG (Green, Red, IR)			
Wavelength (λ_{peak})	526, 660, 950 nm	526, -, - nm	526, -, - nm
Spectral sensitivity	0.31, 0.56, 0.84 A/W	0.31, -, - A/W	0.31, -, - A/W
Radiant sensitive area	0.89 x 0.89 mm	1.29 x 2.69 mm	1.29 x 2.69 mm
Sample rate	333, 333, 333 Hz	125, -, - Hz	8, -, - Hz
Environmental measurements			
Temperature sensor			
Noise	0.004 ºC RMS	0.004 ºC RMS	-
Sample rate	33 Hz	4 Hz	-
Pressure sensor			
Noise	1.3 Pa RMS	1.3 Pa RMS	-
Sample rate	33 Hz	4 Hz	-
Humidity sensor			
Noise	0.07 % RH RMS	0.07 %RH RMS	-
Sample rate	33 Hz	4 Hz	-

[a] Note that a "-" indicates that particular sensor was not enabled during that measurement mode.

The remaining board, the sternum PPG board, contains three pairs of SFH7060s (Osram) and MAX86140 s (Maxim Integrated, San Jose, CA). We selected the SFH7060 over the SFH7072 due to the increased area of the PDs, increasing the total sensitivity and compensating for the decreased perfusion at the sternum when compared to the wrist. Since the SFH7060 only includes a single PD, we selected the single-channel MAX86140 AFE. Similar to the SFH7072, the SFH7060s still contain green, red, and IR LEDs.

The data is temporarily saved to the SD card. The watch interfaces with the computer through a micro-USB port on the main board and is accessible through a cut-out in the case. A custom C# based app communicates using the universal serial bus (USB) protocol with the microcontroller to pull and subsequently delete data on the SD card, freeing up space for future measurements. Additionally, the inserted micro-USB interfaces with a battery charger (bq24232, Texas Instruments) to charge the battery.

3.2.2   Device Operations

We designed the watch to operate in three modes: standby, continuous, and PTT measurement mode. During standby mode, all sensors on the device are shutdown except for a single green PPG on the wrist which is sampled at 8 Hz and configured to act as a proximity sensor. When an object approaches the sensor, as when the user places the watch on the wrist, an interrupt flag is set, and the watch transitions to continuous mode. During this mode, the three green wrist PPGs, accelerometer, and gyroscope are active and sample at 125 Hz. The environmental sensor is also turned on and samples at 4 Hz. The lower sample rate saves power while providing enough context for activity classification. The watch transitions to PTT measurement mode when the ECG senses a lead-on event. To

trigger this mode when wearing the watch on the wrist, the user will need to touch the wrist-band electrode with the hand contralateral to the watch, as seen in Figure 6. During PTT measurement mode, the sternum PPGs are turned on and the device was placed directly in contact with the subject's skin at the mid sternum. All wavelengths (i.e., green, red, and IR) of both the wrist and sternum PPGs were activated. The sternum was chosen primarily for optimal SCG quality based on some of our previous work characterizing signal quality at different sensor placement locations [50]. In this mode, all sensors are sampled at the full rate as shown in Table 1. Although the measurement bandwidth of the PPG and environmental signals is very low ($\leq$10 Hz), part of the reason we were able to acquire high-quality data, was related to our ability to oversample all of these signals such that less complex filters are needed during post-processing. In addition, because of our power-saving operational modes, we were not concerned with increased power consumption or memory storage requirements when sampling higher. Figure 5F shows the ensemble average of the ECG, SCG, GCG, and PPG during a 30-second recording while the watch was operating in the PTT measurement mode.
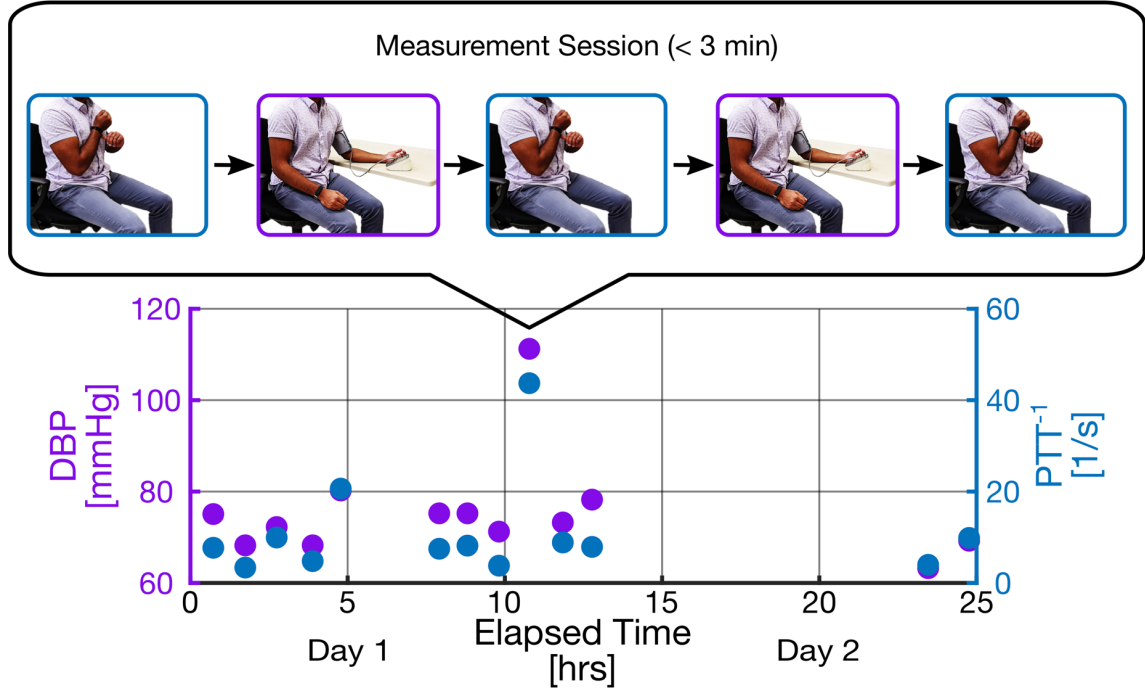
Figure 6. Measurement protocol diagram. Subjects were instructed to acquire pulse transit time (PTT) and blood pressure (BP) cuff measurements hourly, over the course of a 24-hour period, wearing the watch throughout the period except during sleep. As shown, the watch was worn on the arm contralateral to the oscillometric cuff. Each hourly measurement session required a sequence of PTT measurements, acquired by placing the watch on the chest, in contact with skin, and touching the wrist electrode, and BP cuff measurements, taken using the oscillometric cuff. Diastolic BP (DBP) and inverse pulse transit time (PTT^{-1}) data for Subject 21 are shown.

Figure 5G shows the recordings of all sensors during a 10-minute walk outdoors. When the user touched the wrist electrode, the watch transitioned to PTT measurement mode, increasing the sample rate and sampling from all sensors. When the finger was removed, the watch returned to continuous mode, decreasing the sample rate and only sensing from sensors that give activity context for determining physiological states. Configuring the watch to transition between these modes reduces power consumption and memory requirements, as well as indicating PTT measurement timings. Specifically, the additional capability of transitioning between device modes (PTT measurement, continuous, standby

mode) allowed us to save battery life (8, 30, and 38 hrs) enough to readily acquire PTT data for a complete assessment of around-the-clock BP changes. In context, if used as an ambulatory BP cuff, which takes measurements every 30 minutes, the watch would only be in measurement mode 0.8% of the time with the 15 second measurements used herein.

To compensate for variable PPG signal quality due to different skin tones amongst subjects, we decided to automatically adjust the LED drive current for the individual PPGs and wavelengths to prevent railing and improve signal quality. This required having a two-state current threshold and adaptively decreasing the LED current and switching to the lower threshold value if the most significant byte (MSB) of the input light measured from the PD exceeded the higher threshold. Otherwise, the current cutoff was increased to its higher value to allow the signal to grow in amplitude.

3.2.3 Study Protocol

This study was conducted under a protocol approved by the Georgia Institute of Technology Institutional Review Board. For this study, 21 (16 males, 5 females) young and healthy volunteers (Age: 25.9±3.4 years, Weight: 74.4±16.9 kg, Height: 176.3±10.9 cm, and body mass index (BMI): 23.7±3.6) with no prior history of heart problems were recruited, and written informed consent was obtained. The subjects were instructed to take the watch and an Association for the Advancement of Medical Instrumentation (AAMI) approved BP785 N BP cuff (Omron, Kyoto, Japan) home and acquire measurements hourly over the course of 24 hours, taking at least 12 total measurements. In addition, they were told to specifically take a measurement directly before and after bedtime and to not wear the watch during sleep. Therefore, the watch was worn until bedtime to obtain data from

the continuous mode—for activity context—was charging during sleep, and re-worn the next morning. The subjects were briefed on how to use the watch and BP cuff to perform measurements. The watch was worn on the right wrist, and the BP cuff was worn on the left arm. They were not worn on the same arm to mitigate any potential confounding effects of vessel occlusion associated with the oscillometric cuff measurement. Additionally, the maneuver where the user places the watch on their sternum benefits from being at a heart level which helps increase BP reading accuracy from wrist-worn devices [51]. Due to this user-input requirement, our device currently can only be used to reliably acquire measurements when stationary, as in this study. This fit well with the procedure for the oscillometric cuff, which itself can be even more restricting and tedious to obtain an accurate measurement. Since all the data was saved automatically from both devices the protocol required low-user-input, essential for an at-home measurement system. Every measurement session consisted of five sections broken down into three 30 second watch measurements with BP cuff measurements in between as shown in Figure 6, resulting in approximately three-minute-long measurement sessions. We ensured that at least 15 seconds were added between the middle watch measurement and the BP cuff measurements before and after to comply with the American Heart Association's (AHA's) recommendation of one-minute intervals between BP cuff measurements. To keep this consistent, both before the first BP cuff measurement and after the final BP cuff measurement, we made sure that 15 seconds were added before proceeding to that next measurement.

3.2.4   Signal Processing

The signal processing was carried out in MATLAB R2018a (MathWorks, Natick, MA). Only the data from the PTT measurement mode were analyzed in this study. The entire recording was partitioned using the serviceable ECG lead-on detection feature to extract signals from each of the individual measurement sessions. We reduced the length of signals to 15 seconds per session for PTT analysis to remove sections corrupted with motion artifacts caused by the subject still adjusting and placing the watch on the sternum. Additionally, the sternum and all green and red wavelength PPGs were not utilized as the IR wavelength wrist PPGs had the highest mean SNR, potentially due to IR wavelength's ability to penetrate deeper in the tissue and capture larger, more pulsatile arteries. Furthermore, we attempted to use only data from the last cuff reading and measurement session as the subject had a greater likelihood of reaching a resting steady-state before readings. Since the subjects did not take both measurements at the same time, using the later measurements when the subject was more likely to have a steady BP allowed us to more accurately compare cuff BP to watch PTT. However, a few subjects had corrupted watch measurements due to erratic toggling probably due to misapplication of the ECG. In those cases, we used the latest clean watch section. For subjects whom we had to use the first watch section, we also used the first BP cuff measurement. Additionally, for one subject that we did not use the first watch section for, we used the first cuff measurement because the second had the lowest recorded standard deviation (SD) of DBP at 2.2 mmHg.

The PTT was calculated as the difference between the proximal timing reference, aortic valve opening (AO) point of the dorso-ventral SCG (i.e., z-axis acceleration), and the distal timing reference, foot of highest SNR PPG. First, we filtered the ECG, SCG, and PPG signals using a digital FIR bandpass filter with a bandwidths of 2.2–30 Hz, 0.8–25 Hz, 1–

8 Hz, respectively. Then, we split the SCG and PPG waveforms into separate beats by using a simple peak detection algorithm for determining R-to-R intervals of the ECG. Next, we ensemble averaged both the SCG and PPG beats and the resulting wave- forms were used to extract both of the aforementioned timing references. The SNR was calculated using a noise-to-signal ratio (NSR) detection algorithm detailed in [52]. Both the methods to determine the two timing references, the foot of the PPG and the AO point of the SCG, were the same as those used in our previous work [45]. Specifically, the foot of the PPG was computed from the intersecting tangent method described in [45] and the AO point was assumed to be the first peak in each ensemble averaged window. SNR thresholds were set to retain only high-fidelity signals; if the SNR of the SCG or PPG beats was not greater than the prescribed cutoff, then the respective ensemble averaged waveforms were deemed too noisy for use. If the SCG or all of the PPG waveforms were discarded, then that measurement session was not used for PTT calculation. If the subject had fewer than 9 measurements with valid SNR levels, we gradually decreased SNR thresholds in an effort to yield more data points. The logic behind our approach was sound as it led to subject-specific SNR thresholds but only to yield at least 75% of total measurement sessions per subject for regression. In general, not surprisingly, inconsistencies due to an unsupervised study led to low SNR signals overall.

3.2.5 Statistical Analysis

The multiple linear regression shown in Figure 7 was performed independently on subject-specific MAP, DBP, and SBP inverse PTT value pairs to calculate the coefficient estimates for each of the three BP components per subject. The calibration coefficients used in the regression model therefore are merely the slope and y-intercept of the line of

best fit. Outliers were removed if the corresponding residual was greater than expected in 95% of new observations. The mean-absolute-difference (MAD) was computed from the mean of the absolute value of the difference between the estimated and reference BP. The error bounds for analysis were chosen based on the Institute of Electrical and Electronics Engineers (IEEE) Standard for Wearable Cuff-less BP Measuring Devices [53] and the MAD was compared to the requirements therein. Finally, the root-mean-square error (RMSE), which was calculated from the root-mean-square (RMS) of the difference between the estimated BP and measured BP, was also presented because it is more sensitive to outliers.

3.2.6   *Calibration Analysis*

The aforementioned slope and y-intercept outputs from linear regression are the calibration coefficients K_1 and K_2 in the popular PTT model [18] shown in Equation 3 above.

In this section, we will present two new potential calibration methods that leverage the natural variability in BP and show promise in reducing calibration requirements for a PTT-based BP estimation device: (1) a 'semi-globalized' model and (2) a two-point calibration model. For these additional calibration analyses, only DBP estimation was examined due to the im- proved correlations. In general, PTT correlates better with DBP, as the distal timing reference used, the foot of the PPG waveform, occurs during diastole [18]. First, we investigated the performance of our subject-specific curve in estimating intrasubject DBP when trained using an increasing number of calibration points. Then, we sought to compare this intrasubject model, in which both the K_1 and K_2 calibration coefficients are subject-

specific, to those of semi-globalized models. This 'semi-globalized' model determines one calibration coefficient using intrasubject data and the other one from all the remaining subject's data—which we refer to as the 'global' set herein. While this model still requires intrasubject data and thus requires subject-specific calibration, the burden on calibration is reduced since only one variable is needed for calibration as the 'global' set is used to calibrate the second variable. Specifically, in our work, the global K_1 model trains K_1 on the global set and K_2 on intrasubject data. Similarly, the global K_2 model trains K_2 on the global set and K_1 on intrasubject data. Finally, we investigate the performance of two, intrasubject two-point calibration methods that either use the subject-specific maximum and minimum DBP values for calibration or the subject-specific maximum and minimum PTT values.

Data points of PTT and corresponding DBP values for each subject were randomly selected for training an intrasubject linear regression curve used to determine calibration coefficients. These coefficients were then used to estimate DBP based on the PTT values from the remaining data points (i.e., testing set) for that subject. As aforementioned, the RMSE was computed between the estimated and measured DBP. This process was repeated until the averaged RMSE reached an expected value. We verified that overfitting was avoided, by ensuring that none of the testing subject's data was trained on for our intrasubject multi-point calibration testing loss results shown in Figure 8A. An increasing number of training points were used, which were again independently and randomly selected from each subject. As shown in Figure 8 intrasubject training stopped once a total of six calibration points was reached, as there were subjects with only seven total calibration points available. Since regression was not possible based on a single training

point, for single-point calibration we assumed that the first randomly selected data point's DBP value would be the same estimated DBP value for all of the subject's points, hence the labeling 'Constant DBP' in Figure 8.

To test the performance of a semi-globalized model to estimate DBP from PTT, we investigated placing global constraints on either the K_1 or K_2 calibration coefficient while adaptively changing the other. The individual global methods either fix the testing subject's K_1 or K_2 to the K_1 or K_2 output of the linear regression curve calculated from all the PTT and DBP data points for all the remaining subjects, respectively. That is, none of the held-out test subject's data were used when training the global coefficient. The remaining calibration coefficient was estimated for each subject independently using this global constraint for an increasing number of calibration points.

Two, two-point calibration methods were tested and compared to the regular multi-point calibration already presented in this study. For these methods either both the PTT values associated with the maximum and minimum BP or the maximum and minimum PTT values over the subject's 24-hour period were chosen for use in training a linear regression curve for BP estimation. Subjects were removed if BP and PTT values used for calibration directly correlated. This resulted in only one subject being removed, and only for the BP dynamic range method. The other subject that was removed from both methods was identified as an outlier probably due to having the lowest Pearson correlation coefficient ($r = 0.44$) of the entire population.

Two-sample t-tests were performed for these various calibration analyses to assess the significance (P<0.05) level of these differences in RMSE from independent, randomly sampled points with normal distributions.

3.3   Results

Figure 7 illustrates the correlation and Bland-Altman plots for PTT-based BP calibration of MAP, DBP, and SBP across all subjects. A more thorough view of our results per subject are provided in Table 2. The mean MAD was 2.24 mmHg, 2.50 mmHg, and 4.03 mmHg for DBP, MAP, and SBP, respectively. The mean±SD RMSE was 2.72±0.75 mmHg, 2.99±1.12 mmHg, and 4.75±2.29 mmHg for DBP, MAP, and SBP, respectively. DBP and MAP estimation had better confidence intervals (95%) than SBP at 5.64 mmHg, 6.48 mmHg, and 10.67 mmHg, respectively. Our Pearson correlation coefficients were 0.69, 0.61, and 0.33 for PTT-based DBP, MAP, and SBP estimation respectively. Across all subjects we used data from 216 out of 245 total measurement sessions (88%), with at least 75% of measurements used per subject. All unused measurement sessions were deemed too noisy for a trustworthy PTT calculation.
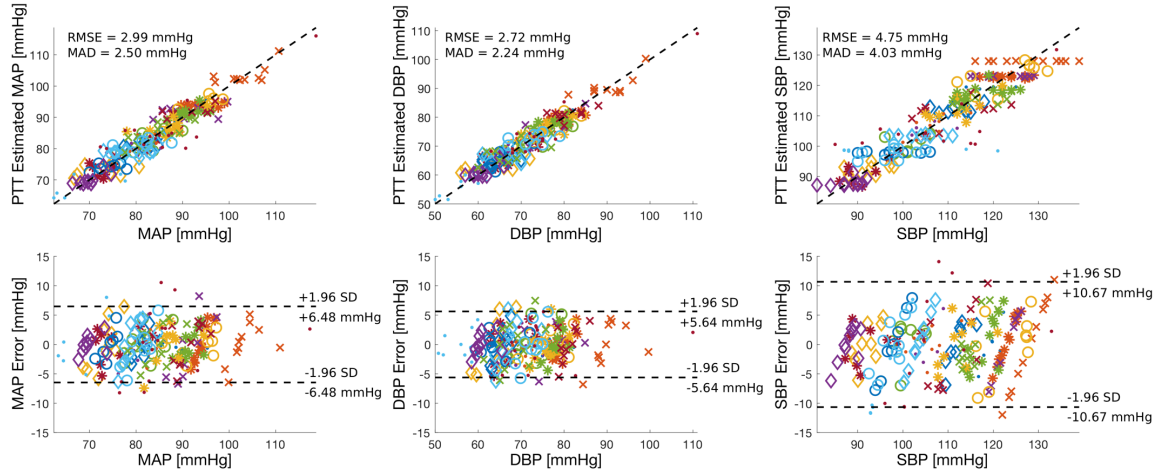
Figure 7. Correlation and Bland-Altman plots between pulse transit time (PTT) estimated blood pressure (BP) and gold-standard oscillometric cuff BP for mean arterial pressure (MAP), diastolic BP (DBP), and systolic BP (SBP) estimation. The root-mean-square error (RMSE) and mean-absolute-difference (MAD) for each correlation are shown.

Table 2. Individual subject diastolic blood pressure estimation results

Subject	μDBP [mmHg]	RMSE [mmHg]	R	e < 5 mmHg
1	77 ± 3	1.09	0.92	1.00
2	79 ± 3	2.31	0.54	1.00
3	64 ± 5	4.07	0.48	0.70
4	76 ± 6	3.01	0.84	0.89
5	73 ± 5	2.81	0.76	0.80
6	56 ± 4	2.27	0.80	1.00
7	66 ± 5	3.13	0.72	0.89
8	66 ± 3	2.87	0.45	1.00
9	91 ± 5	3.49	0.71	0.90
10	77 ± 5	1.99	0.89	1.00
11	69 ± 4	2.61	0.67	1.00
12	78 ± 3	2.36	0.48	1.00
13	67 ± 4	3.54	0.54	0.82
14	81 ± 4	2.90	0.50	0.90
15	64 ± 4	1.64	0.90	1.00
16	72 ± 3	2.18	0.72	1.00
17	75 ± 4	2.70	0.64	0.89
18	61 ± 3	1.73	0.75	1.00
19	68 ± 5	3.64	0.69	0.83
20	73 ± 4	3.28	0.44	0.78
21	75 ± 12	3.50	0.95	0.69
μ	**72**	**2.72**	**0.69**	**0.91**
σ	**9**	**0.75**	**0.16**	**0.10**

Figure 8 depicts changes in RMSE across a different number of training points and

comparisons between semi-globalized calibration models. Notably, in Figure 8A RMSE

significantly (P<0.05) decreased from a single-point calibration (6.05±1.75 mm Hg) to four-point (4.73±2.41 mm Hg, P=.0495), five-point (4.24±1.97 mm Hg, P=.0043), and six-point (3.83±1.40 mm Hg, P=.0004) calibration. Four points were the minimum required for calibration to result in a mean (4.73±2.41 mm Hg) that was lower than that of the single-point calibration (6.05±1.75 mm Hg). Despite not showing statistical significance, the globalized K_1 calibration model in Figure 8B outperformed the regular intrasubject calibration with one point (5.34±1.59 mm Hg vs. 6.05±1.75 mm Hg). However, at four and six points the regular intrasubject calibration model began to outperform the global K_2 model (4.73±2.41 mm Hg vs. 4.81±1.22 mm Hg) and global K_1 model (3.83±1.40 mm Hg vs. 4.03±1.28 mm Hg) respectively.
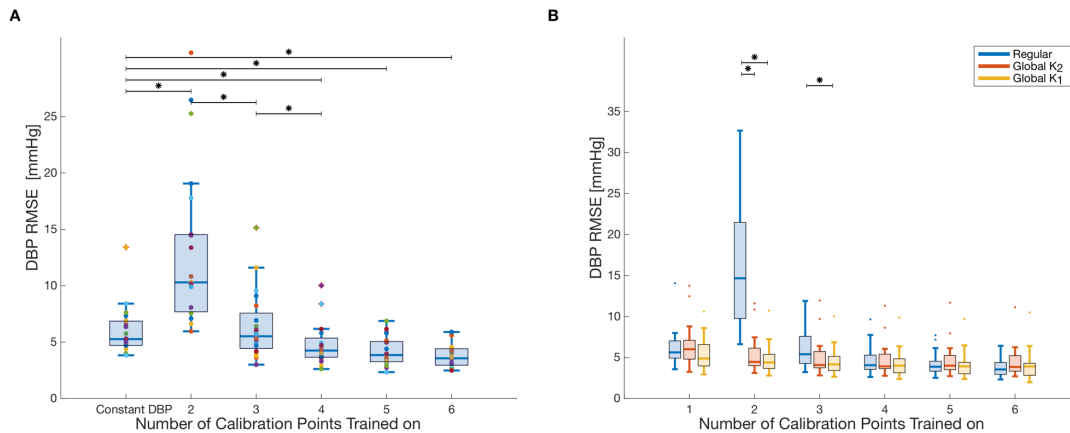
Figure 8. A, Boxplots showing the statistically significant (*P<.05) decreasing root-mean-square error (RMSE) for diastolic BP (DBP) in intrasubject testing loss with an increasing number of calibration points. B, Boxplots showing the notable differences in RMSE for DBP in intrasubject testing loss between the regular intrasubject calibration method, the global K_2 model, and the global K_1 model with an increasing number of calibration points.

Figure 9 shows the boxplots of two different two-point calibration methods compared to the regular multi-point calibration method. The mean±SD RMSE values for the regular

multi- point, BP dynamic range, and PTT dynamic range methods are 2.71±0.75 mmHg, 5.99±3.03 mm Hg, and 3.86±1.53 mm Hg respectively. Both dynamic range two-point calibration methods significantly outperformed the regular, randomly selected, two-point intrasubject testing loss (11.62±16.82 mm Hg) seen in Figure 8A. The mean MAD was 4.66 mm Hg and 3.16 mm Hg for the two-point BP dynamic range and PTT dynamic range calibration methods, respectively.
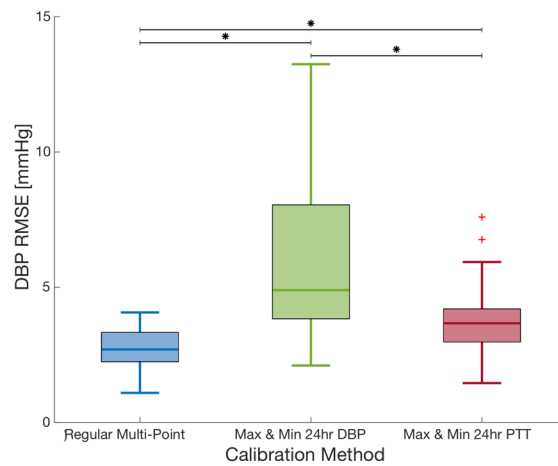
Figure 9. Boxplots showing statistical significance (*P<.05) in root-mean-square error (RMSE) for diastolic BP (DBP) intrasubject testing loss between two different two-point calibration methods using either the maximum and minimum DBP values or pulse transit time (PTT) values and the standard multi-point calibration method.

3.4   Discussion

This study represents, to the best of our knowledge, the first time that BP has been estimated using noninvasive PTT measurements in an at-home setting. We demonstrated the feasibility of a more convenient method for obtaining ambulatory BP than the standard oscillometric cuff and presented new methods for accurately estimating BP even when calibrated less frequently. The work represents an important step towards enabling

wearable PTT-based BP estimation and monitoring for persons outside of clinical settings, including through the development and validation of a novel watch-based form factor with embedded systems innovations enabling robust sensing and storage of PTT.

3.4.1 Tracking Around-The-Clock BP

We developed a PTT-based BP monitoring device and demonstrated accurate monitoring of BP throughout the day in an at-home setting. Our results for MAP, DBP, and SBP were well within the acceptable criteria for BP estimation error set by the IEEE standard (MAD≤5 mm Hg) [53]. Ultimately, we were still able to achieve a reliable correlation between PTT and BP even with several factors—intrinsically coupled to an in-the-wild study— confounding PTT measurements and independently affecting BP.

The average correlation in this study was lower than that in our group's previous work which was conducted in a lab setting—0.84 and 0.69, respectively—but this reduction was attributed to the uncontrolled setting as well as narrower BP ranges and unaccountable transient fluctuations in vascular smooth muscle tone [45]. Despite the weaker correlation, our RMSE values were still within 5 mmHg for MAP, DBP, and SBP, understandably implying that BP did not change considerably. Specifically, not only were there narrower daily BP ranges, due to the lack of perturbations previously employed, but also several confounding factors that affected BP in this uncontrolled, in-the-wild experiment. To elaborate, in the previous work, as with many PTT studies, known perturbations that affected both smooth muscle contraction (SMC) and BP proportionally were employed to modulate BP and determine the effectiveness of a PTT-based approach in a controlled lab setting. Since both SMC and BP concomitantly and considerably affect PTT when

measured from peripheral arteries [6], calibration accounted for changes in both BP and vasomotor tone. In an uncontrolled setting, external stimuli can modulate vasomotor tone independently from BP, resulting in unbalanced peripheral arterial elasticity which relates to PTT. For instance, a study demonstrated that the relationship between pulse wave velocity and muscle sympathetic nerve activity is independent of BP in normal individuals [54]. This suggests that over the course of a day, several encounters and stressors can instantaneously modulate sympathetic arousal to different degrees acutely affecting vascular smooth muscle tone prior to and independently from BP, transiently confounding PTT but not BP cuff measurements [55]. Although, we have not previously accounted for transient fluctuations in vascular smooth muscle tone, we try to minimize them by leveraging longer wavelength LEDs to measure the small pulsatile changes in blood volume from deeper arteries in the tissue that would not be affected as much as thinner, more cutaneous capillaries [18]. Despite these obstacles, our device demonstrated accurate BP estimation in an at-home setting.

Predictably, DBP estimation proved to be the most accurate, similar to our previous work [45], as the foot of the PPG wave- form signifies the arrival of the distal pulse wave and signifies end-diastole [18]. Meanwhile, our SBP estimation performed the worst, as the peak rather than the foot of the pulse wave occurs during systole [18]. Regardless, recent studies have shown and mentioned that PTT computed from the foot outperforms that from the systolic maximum for both DBP and SBP and thus the peak was not examined herein [56], [57]. It is noteworthy that the subject whose data is plotted in Figure 6, with the highest Pearson correlation coefficient (subject = 21, r = 0.95) also had the greatest standard deviation of DBP (± 12 mm Hg) and had taken the greatest number of

measurements. This subject had apparently performed running exercise before a measurement, which explains the wide DBP range. Additionally, their point of maximum DBP was not determined as an outlier because their PTT had also considerably changed. We found this to be a promising possible indication that it would be best to acquire fewer, more significant, calibration points after some initial exercise or when BP has changed past a significant threshold from baseline to capture the full dynamic range of normal daily BP.

3.4.2 Reducing Calibration Requirements

For the first time, we demonstrated the ability of novel calibration methods to reduce the burden of calibration required for accurate BP estimation through PTT. Notably, we achieved accurate BP estimation within the IEEE's standards using both a semi-globalized calibration model and a two-point calibration method that each use fewer coefficients and fewer points, respectively, for calibration [53].

Our device accurately predicts DBP over the course of a day using only four calibration points—on average less than half of the used data points for the regular multi-point calibration. Due to outliers stemming from the inclusion of noise and lack of wide DBP ranges, our regression-based approach for two and three- point calibration performed worse than single-point calibration. While a good result was obtained with single point calibration, presumably due to low variations in DBP, we found a statistically significant improvement in RMSE when using multi-point calibration versus single point calibration. Furthermore, we assess the ability of the calibration curve to track changes in DBP by providing the Pearson correlation coefficient, resulting in R-values comparable, albeit lower, to those seen in previous works [18]. Global model parameters were then

incorporated into subject-specific models to improve the estimation accuracy at fewer numbers of points.

Our semi-globalized integrated models were better estimators of DBP than the regular intrasubject multi-point method with a fewer number of calibration points. Understandably, the multi-point subject-specific calibration method eventually surpassed the global models. Additionally, the global K_1 model outperformed the global K_2 model considerably and consistently, as well as the regular intrasubject testing loss until six points, though not significantly other than at three calibration points. Though we do not present a globalized intersubject model for estimating BP from PTT, an ideal solution, we believe that the results presented here within show promise for a more realistic solution. Compared to a globalized model, a subject-specific model will realistically always have improved performance, with the downside of increased complexity. However, in the meantime this result demonstrates the feasibility of reducing this complexity and burden by requiring only a single variable for calibration. Specifically, we propose a heuristic that represents an intermediate-globalized model which can be adaptively and marginally tailored to a specific subject to provide a more accurate estimation when using fewer calibration points for estimation.

Using two points for calibration, our device accurately tracks around-the-clock DBP within the IEEE's standards by selecting more physiologically salient calibration points [53]. In addition, they significantly improve upon the intrasubject two-point calibration testing loss seen in Figure 8A. This can be attributed to a training set with wider DBP range, thereby avoiding randomly selected points that neighbor one another and thus do not offer a good assessment of normal daily DBP range. Ideally the best possible two

calibration points would be the ones with the widest range—the minimum and maximum points in which the PTT and DBP change proportionally and markedly together [18]. The PTT dynamic range method yielded a statistically significant improvement when compared to the DBP dynamic range method, potentially due to accounting for differences in vasomotor tone confounding PTT-based DBP estimation. Specifically, we believe that this suggests that there were factors present which changed DBP independently from the PTT, rendering those points poor for calibration. In general, PTT-based studies with wider BP ranges tend to have higher correlations, while ones with narrower ranges tend to yield lower RMSE values [18]. To further decrease computational complexity, this data suggests that a recursive least-squares approach could be applied to a subject's past data to optimally estimate a calibration curve given a new point. These results become especially exciting when considering the ability of our hardware to use a multimodal sensor fusion approach to gate different operational modes based on hemodynamic-contextualized data and prompt users for these more physiologically salient calibration measurements.

3.4.3   Limitations and Future Design

3.4.3.1   Study Population Demographic

Our PTT-based device should be tested in elderly, overweight, and hypertensive populations. Aside from the growing importance of monitoring younger populations [58], similar to that studied herein, accurate remote monitoring has the ability to immediately improve the hypertension screening and management standard of care. However, first PTT-based BP estimation should be investigated in diverse populations with differences in arterial stiffness, compliance, and SMC [18].

3.4.3.2 PTT Models and Calibration Longevity

Linear regression, albeit rudimentary, was used in this study: while non- linear models can have better accuracy, they tend to contain more than two unknown variables which dictates the need for more PTT and BP calibration points [18]. Furthermore, in cases where perturbations do not noticeably change BP, or in our case where there were no perturbations, only linear models might be feasible and employable [18]. Also, the confounding factors that were inherently prevalent in this unsupervised, at-home study such as SMC can have a linearizing effect [59]. Eventually, however, once enough datasets amongst at-home, longitudinal, and at-risk monitoring subjects have been collected, these similar methods could be reanalyzed and combined with more recent work that has shown promise in estimating BP either through analytical models [60] or machine learning (ML) approaches for a potential globalized model. As a whole, further work needs to be completed to assess how reliably subject-specific calibration curves can function across several days, thereby eliminating the need for consistent re-calibration.

3.4.3.3 Novel Signal Processing Algorithms and Sensor-Fusion for Improved PTT Calculation and BP Calibration

One of the challenges of using the SCG as the proximal timing reference is determining the true AO peak. The signal varies greatly between subjects, and the peaks can either be mistaken for the wrong physiological markers or the location of the peaks can be corrupted by either motion artifacts or improper placement of the watch. While for most subjects our method to determine the AO point was sound and led to a high correlation between PTT and BP, for a few sessions it annotated the incorrect AO point and had to be manually

remedied. In our previous study we relied on the user to undergo a protocol such as exercise to increase the heart's contractility to decrease the PEP [45]. However, at-home monitoring of natural variability in BP is a more challenging problem and dictates a need to capitalize on promising signal processing advances. Specifically, by using new ML approaches to assess signal quality [61] or a gyroscope as an additional proximal timing reference [49].

Novel methods to both identify higher quality PPG signals and select those from arteries deeper in the tissue should be investigated to improve the distal timing reference and avoid inconsistencies that arise when measuring from cutaneous capillaries [18]. In particular, we attached an array of three LED-PD pairs to the top side of the watch. These now allow for a pulse wave measurement at the sternum as the user performs the same maneuver needed to capture the SCG. The sternum PPGs, taken from a more central location, tend to have pulse waves with a different morphology—typically with smoother systolic peaks—and therefore should be investigated further to see if timing references extracted from them will lead to a more reliable BP estimation [62]. Additionally, examining PPG signal features will not only allow us to better select amongst the various PPGs but also elucidate properties of the underlying waveform morphology that are of greater importance in different populations. For example, features such as the augmentation index and rise-time have been shown to capture physiologically salient pulse waves that generate a more accurate, and meaningful estimated BP [45].

3.4.3.4 Hardware Advances for Usability

For remote monitoring, wireless technologies (e.g., cellular, LoRa, Bluetooth, and Wi-Fi) must be incorporated such that data can be automatically uploaded to the cloud for

clinicians to view. Additionally, PTT-based BP estimation should be handled on-chip or on the cloud prior to viewing by leveraging advances in lightweight firmware or cloud-based algorithms for computation.

3.5   Conclusion

Ultimately, we show a more convenient method for obtaining accurate ambulatory BP than using the standard oscillometric cuff and present new calibration methods for BP estimation using fewer calibration points that are more practical for a real-world scenario. Remote monitoring of hypertension is critical to the success of the AHA and World Health Organization's new missions and can assist prevention, offer early detection, and incentivize lifestyle changes to ultimately increase both the quality-adjusted life years (QALY) of at-risk patients and lifetime savings versus clinic BP measurements [3], [63]. For already hypertensive patients serial and longitudinal monitoring of BP at-home, and in outpatient settings, can be used to remotely titrate care of antihypertensive drugs [64]. We have demonstrated that a watch- based wearable device, capable of noninvasive PTT based BP estimation, can reliably and conveniently track natural around- the-clock variability in BP in an at-home setting. Following future studies with more diverse populations, and longer-term studies aimed at evaluating the time-course for which the calibration curve may hold as accurate, this device may enable more convenient and widespread monitoring of BP outside of clinical settings.

CHAPTER 4. ENABLING WEARABLE PULSE TRANSIT TIME-BASED BLOOD PRESSURE ESTIMATION FOR MEDICALLY UNDERSERVED AREAS AND HEALTH EQUITY

4.1 Introduction

Noninvasive and cuff-less approaches to monitor BP, in light of their convenience and accuracy, have paved the way toward remote screening and management of hypertension. However, existing noninvasive methodologies, which operate on mechanical, electrical, and optical sensing modalities, have not been thoroughly evaluated in demographically and racially diverse populations. Thus, the potential accuracy of these technologies in populations where they could have the greatest impact has not been sufficiently addressed. This presents challenges in clinical translation due to concerns about perpetuating existing health disparities.

In our previous work, we designed a wearable, multimodal, wrist-worn PTT monitoring device ("SeismoWatch") and validated it in both controlled lab [45] and unsupervised home [65] settings, primarily on young, healthy persons with lighter skin. Here, we expand upon our previous work with a community-engaged research strategy that leverages expertise from a nonprofit organization serving MUAs in Georgia and evaluated our device in a more diverse population. We present our device's ability to accurately estimate BP in this diverse population and capture significant demographic-level differences in underlying arterial stiffness that coincide with observations from existing literature, through the calibration coefficients used in our BP estimation model. This study represents the first

time that a noninvasive, cuff-less, PTT-based wearable device has been extensively evaluated in a community-based diverse population as a potentially reliable and convenient monitoring option toward, ultimately, the remote screening and management of hypertension for health equity.

4.2 Methods

4.2.1 Study Protocol

A comprehensive breakdown of the demographics of the study population is presented in Table 3. This study was conducted under a protocol approved by the Georgia Institute of Technology institutional review board (protocol number H19251). The study was separated into two different populations (N=44 participants): (1) a young and healthy homogeneous population (first cohort=26 participants) and (2) an older, entirely Black, higher BMI, metropolitan population (second cohort=18 participants) recruited later through the help of our community outreach partners—a nonprofit organization serving medically underserved persons in the state of Georgia. For the first cohort, 26 (19 males and 7 females) young and healthy volunteers (mean age 26.7 years, SD 3.7; mean weight 73.8 kg, SD 14.1; height 173.9 cm, SD 9.6; and mean BMI 24.2 kg/m2, SD 3.2) with no previous history of cardiovascular disease were recruited, and written informed consent was obtained. For the second cohort, 18 (6 males and 12 females) Black participants (mean age 44.1 years, SD 11.7; mean weight 94.4 kg, SD 18.0; mean height 169.6 cm, SD 11.5; and mean BMI 33.2 kg/m2, SD 7.6) with no previous history of cardiovascular disease other than hypertension were recruited from the Atlanta metropolitan area, written informed consent was obtained, and further demographic information was collected post

hoc with verbal consent. Both hypertensive status and the use of regular prescription medications were self-reported.

Table 3. Participant demographics and cardiovascular parameters for study participants (grouped by cohort; N=44).

Demographics and cardiovascular parameters	Homogenous data set (first cohort; n=26; participant 1-26)	Community outreach (metropolitan Atlanta) data set (second cohort; n=18; participant 27-44)	*P* value
Age (years), mean (SD)	26.7 (3.7)	44.1 (11.7)	<.001
Sex, n (%)			N/A[b]
Male	19 (73)	6 (33)	
Female	7 (26)	12 (67)	
Height (cm), mean (SD)	173.9 (9.6)	169.6 (11.5)	.19
Weight (kg), mean (SD)	73.8 (14.1)	94.4 (18.0)	<.001
BMI[c] (kg/m^2), mean (SD)	24.2 (3.2)	33.2 (7.6)	<.001
Obesity class, n (%)			N/A
I	1 (4; participant=23)	2 (11; participant=30, 43)	
II	N/A	3 (17; participant=38, 40, 42)	
III	N/A	4 (22; participant=34, 36, 37, 41)	
Race, n (%)			N/A
Black	1 (4; participant=5)	18 (100)	
Other race	25 (96)	N/A	
Hypertensive status, n (%)			N/A
Normotensive	26 (100)	15 (83)	
Hypertensive	N/A	2 (11; participant=29,37)	
Hypotensive	N/A	1 (6; participant=33)	
Current medications, n (%)			N/A
Hydrochlorothiazide	N/A	2 (11; participant=29,37)	
Lisinopril	N/A	1 (6; participant=29)	
Iron supplement	N/A	1 (6; participant=33)	

[a] Statistical significance between groups in values, where applicable, was computed using an unpaired two-tailed t-test.
[b] N/A: not applicable.
[c] Obesity classified using the BMI per the guidelines from the National Heart, Lung, and Blood Institute of the National Institutes of Health [67] (I: BMI=30-34.9; II: BMI=35-39.9; III: BMI ≥40).

The concept of the study design is shown in Figure 10. Although not explicitly shown, two versions of the SeismoWatch were used in this study: a previous version of the hardware with comparable sensors was used in the young, homogeneous population (i.e., the first cohort), before being adapted for a more robust, portable, and multimodal wearable device used in the metropolitan Atlanta population (i.e., the second cohort). Specifically, the data from these cohorts were collected during two intervals, between which the hardware was revised to incorporate multiwavelength PPGs before investigating the performance of the sensing modality in the underrepresented population. This was essential to assess the efficacy of shorter-wavelength LEDs (i.e., those with shallower skin penetration depths) in a Black population. However, in both the correlations in Figure 11 and calibration coefficient comparisons in Figure 12, only the results derived from the infrared (IR) PPGs, available to both devices, were computed and shown. The other key sensing components and reference system components were essentially identical: (1) the first version of the device used an analog version of the accelerometer (ADXL354, Analog Devices Inc.) to acquire the SCG, whereas the second version simply used the digital version of the same sensor (ADXL355, Analog Devices Inc.) to reduce size and (2) the finger-cuff continuous BP reference system (ccNexfin, Edwards Lifesciences) along with the data acquisition module (MPU150, Biopac Systems) were identical in both studies.

A

SeismoWatch
wearable PTT

ECG
SCG
Wrist PPG array
Sternum PPG array

Reference system
⦿ ECG
◼ Continuous
BP cuff

1. Cardiac ejection onset

Cardiomechanical activity

F_{Heart} → H → Skin — Accelerometer → SCG

2. Arterial pulse wave propagation

LED - PD
Skin
Venous blood

PPG

3. Distal pulse arrival

Aortic valve opening — Pulse transit time — Diastolic foot arrival

B

1. Sitting (120 seconds)
μ_{MAP} (σ)=91 (12) mm Hg

2. Standing (120 seconds)
μ_{MAP} (σ)=96 (10) mm Hg

3. Mental arithmetic (60 seconds)
μ_{MAP} (σ)=100 (14) mm Hg

4. Rest (120 seconds)
μ_{MAP} (σ)=95 (12) mm Hg

5. Cold pressor (60 seconds)
μ_{MAP} (σ)=102 (15) mm Hg

6. Rest (180 seconds)
μ_{MAP} (σ)=96 (14) mm Hg

7. Exercise (60 seconds)
μ_{MAP} (σ)=96 (13) mm Hg

8. Rest (480 seconds)
μ_{MAP} (σ)=95 (12) mm Hg

C

Participant 37: Black female
Age=42 | BMI=45 | Hypertensive

ECG — 1 mV
SCG — 15 mg
PPG$_{IR}$ — 48 nW
PPG$_{Red}$ — 54 nW
PPG$_{Green}$ — 116 nW
ECG — 1 mV
ABP — 60 mm Hg

Time [seconds]

D

Blood pressure [mm Hg]

Exercise

SBP

DBP

Time in protocol [min]

Figure 10. Concept overview and study design. Sensor information and placement locations for wearable system (blue) and reference system (purple). Noninvasive pulse transit time (PTT) measurement concept overview using seismocardiogram (SCG) and photoplethysmogram (PPG) sensors. Study protocol tasks in chronological order with duration and mean (SD) of mean arterial pressure (MAP) values for each task. Sample filtered signals from the participant with the lowest signal-to-noise ratio (SNR) signals (n=37): a hypertensive, high BMI, older Black female. In order from top to bottom: electrocardiogram (ECG), SCG, infrared PPG, red PPG, green PPG signals measured from the wearable system (blue) and the synchronized ECG, and arterial blood pressure (ABP) signals measured by the reference system (purple). Systolic blood pressure (SBP; top) and diastolic blood pressure (DBP; bottom) plotted across the full protocol for participant 37, with rest periods (green) and perturbations used to modulate blood pressure (BP) (red) highlighted in chronological order, and the location where the reference finger-cuff continuous BP system was paused during the exercise indicated.

Figure 11. Wearable pulse transit time (PTT)–based blood pressure (BP) estimation results. Correlation and Bland-Altman plots between PTT-estimated BP and the finger-cuff continuous BP for mean arterial pressure (MAP), diastolic BP (DBP), and systolic BP (SBP) estimation. The root-mean-square error (RMSE) and the mean absolute difference (MAD) for each correlation are shown.
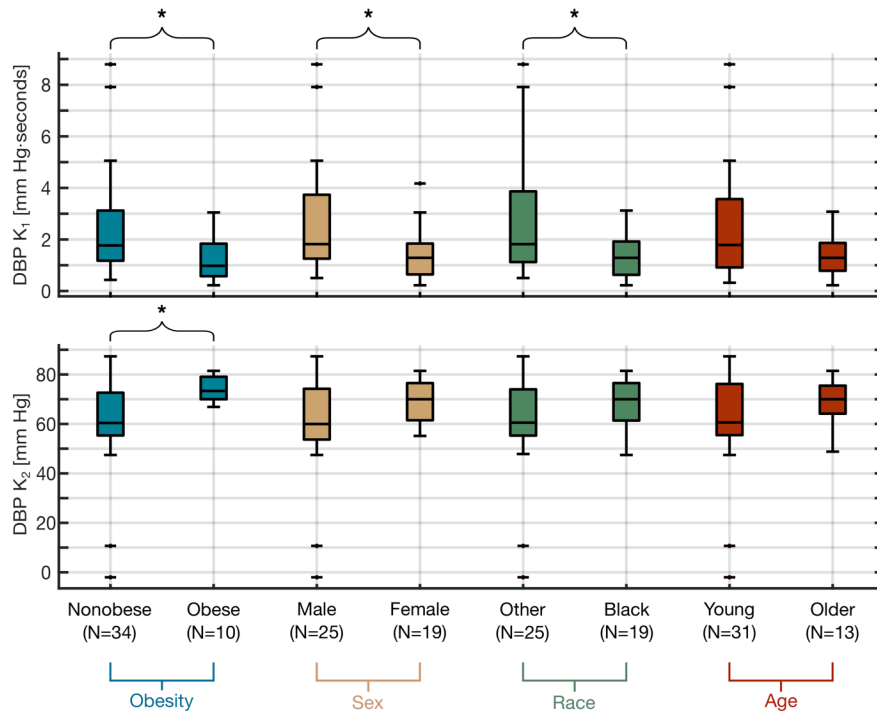
Figure 12. Participant-specific diastolic blood pressure (DBP) calibration coefficients are significantly different in demographics with typical disparities in arterial stiffness. Boxplots showing the statistically significant (*P<.05; Mann-Whitney U)

difference in the DBP K_1 and K_2 calibration coefficients between participants who are nonobese and obese. Boxplots showing the statistically significant (*P<.05; Mann-Whitney U) difference in the DBP K_1 calibration coefficients between male and female participants. Boxplots showing the statistically significant (*P<.05; Mann-Whitney U) difference in the DBP K_1 calibration coefficients between participants of other race and Black participants. Boxplots showing the difference in the DBP K_1 and K_2 calibration coefficients between young and older participants.

To acquire a timing reference for the start of a cardiac cycle, while serving as a reference for alignment to the wearable system signals, a wireless ECG module (BN-EL50, Biopac Systems) was attached to the participant in a three-lead configuration with Ag/AgCl gel electrodes as shown in Figure 10. As depicted in Figure 10, a finger-cuff BP sensor based on the volume-clamp methodology (ccNexfin, Edwards Lifesciences) [66], [67] was placed on the same hand as the watch, acquiring a reference measurement of continuous beat-by-beat BP. Although volume-clamping continuous BP devices are not the clinical gold standard for ABP measurements, an arterial line was not feasible due to invasiveness, and a sphygmomanometer was not used because of the need for a trained professional and lack of beat-by-beat BP data. Similarly, semiautomated BP cuffs were not used as they hinge on following strict guidelines to obtain an accurate reading, such as being seated and resting the arm at heart level, which were impossible to satisfy simultaneously while acquiring watch measurements, given the need for the contralateral hand to touch the ECG electrode to activate the PTT mode [65]. In addition, it was recently demonstrated that a volume-clamping–based system had comparable accuracy with noninvasive oscillometric BP cuffs [68]. All reference system sensors were sampled at 1 kHz and interfaced to a computer using a data acquisition system (MPU150, Biopac Systems) and its corresponding software (Acqknowledge, Biopac Systems). The reference system files were saved to a desktop computer for postprocessing.

Participants were asked to change into either a V-cut T-shirt or tank top, if not wearing one already, to acquire the sternal PPGs included in the wearable designs, though not examined in this study. The watch was fitted such that the PPGs faced the radial artery on the ventral side of the wrist. To capture the PTT, the participant performed a simple maneuver to place the watch on the sternum to acquire the SCG for the proximal timing reference, as shown in Figure 10, whereas the PPGs were sampled at both the sternum and wrist. Although this offers a noncontinuous assessment, routine remote BP monitoring using oscillometric devices has already demonstrated clinical value despite similarly not offering continuous BP measurement [69]. Specifically, ambulatory BP monitors, due to their superior portability and measurement frequency—comparable with what this wearable device can easily provide [65]—have become invaluable for the screening and management of hypertension [69] such that the added benefit of continuous BP measurement may only be marginal.

In order, the participants went through a 2-minute baseline period while sitting before obtaining another 2-minute baseline measurement while standing. Then, a series of perturbations with varying rest periods in between were used to modulate BP. First, a mental arithmetic exercise was used to increase BP [18], in which participants were given a three-digit integer and were told to add the sum of the digits to the number repeatedly for 1 minute. Then, a cold pressor test was conducted in which participants submerged their hand contralateral to the watch in a bucket of ice water for as long as tolerable or until the full minute. Finally, during the exercise session, the finger cuff was removed to avoid damage, and the participant performed either a stair stepping or bicycling exercise, based on personal preference, for 1 minute. As mentioned in our previous work [65], the new

version of the watch enters the PTT measurement mode when the user places a finger from their hand contralateral to the watch on the positive wrist ECG electrode; therefore, we were unable to acquire PTT data during exercise for both cohorts and cold pressor for the participants in the second cohort (i.e., second cohort). Although with the newer hardware, we were unable to collect PTT data during the cold pressor perturbation for the second cohort, the effect of the cold pressor—assessed directly after the hand was removed from the ice water (i.e., a maximum of 1 minute after immersion)—was still well within its physiological window during the following rest period [70]. Overall, as our device is not designed to offer continuous measurements of BP, examining the effect of these perturbations in the rest period directly following them, similar to our previous work [45], still allowed for a comprehensive evaluation of the methodology in a diverse population. However, PTT data from the first cohort during the cold pressor were still used. As the BP data from the cold pressor test were still acquired for the second cohort, as the continuous BP cuff was still on, the mean arterial pressure (MAP) values were factored into the ones displayed in Figure 10. To do so, a 50 ms moving average filter was applied to the measured continuous BP signal, ensemble averages of 10 heartbeats with 50% overlap were taken, and the BP beat with the highest SNR was selected.

4.2.2 Signal Processing

The signal processing pipeline is shown in Figure 13. All signal processing and statistical analyses were performed in MATLAB R2018a (MathWorks). Before preprocessing the SCG and PPG signals acquired from the wearable system, it was imperative to time-align them to the continuous BP signal from the reference system using the respective ECGs to ensure proper temporal comparison. Specifically, the ECGs from

each system were first filtered using a digital finite impulse response bandpass filter (BPF; fpass=10-40 Hz) to remove baseline wander due to postural sway and extract the R-wave, which was then identified using a simple peak detection algorithm. Then, cross-correlation was used to align the R-peaks of the two ECG readings by detecting the amount of lead and truncating either the wearable or reference signals depending on the condition. After alignment, the dorsoventral axis of the SCG (i.e., z-axis acceleration) and green, red, and IR wrist PPGs were filtered using a digital finite impulse response BPF with bandwidths of 1-40 Hz and 1-8 Hz, respectively, to remove their out-of-band noise and baseline wander due to respiration. In addition, the continuous ABP waveform was smoothed using a 50 ms moving average filter.
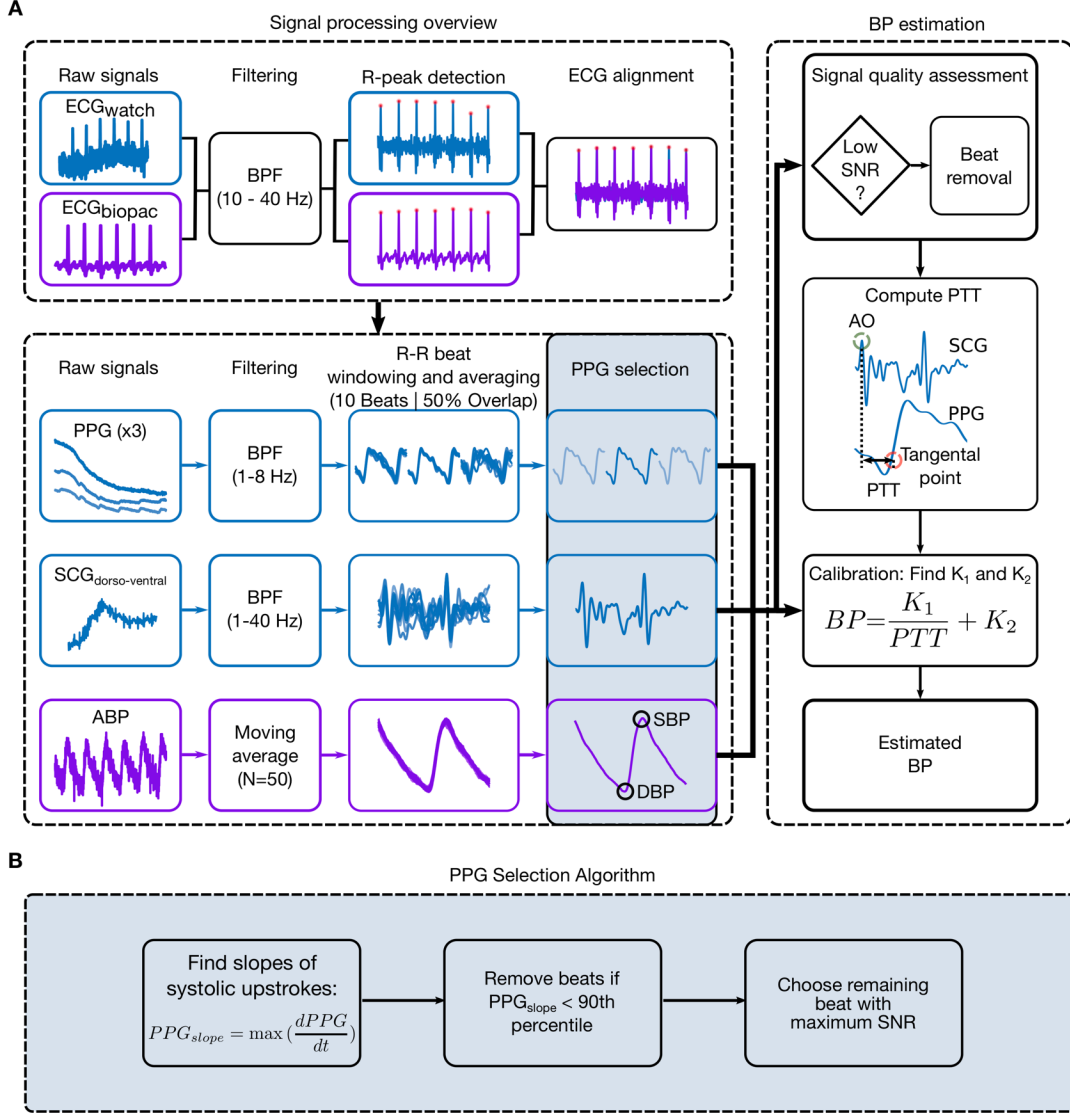
Figure 13. Signal processing pipeline. Block diagram of signal processing overview showing signal alignment using electrocardiogram (ECG) signals acquired from the wearable system (blue) and reference system (purple) before bandpass filtering (BPF), heartbeat windowing, and photoplethysmogram (PPG) selection. After beat selection and signal quality assessment, the pulse transit time (PTT) is computed as the aortic valve opening point (AO) of the seismocardiogram (SCG) to the diastolic foot of the PPG. Calibration is used to estimate blood pressure (BP) using the arterial BP (ABP) waveform acquired from the continuous BP finger-cuff. Block diagram of the custom PPG selection algorithm, locating beats with greater systolic upstrokes and signal-to-noise ratio (SNR).

58

Next, the filtered and aligned SCG, PPG, and ABP waveforms were split into separate heartbeats using the detected R-R intervals of the synchronized ECG. Then, these heartbeat-indexed signals were ensemble-averaged using 10-beat windows with 50% overlap before assessing the signal quality to select the highest quality beat per task for each participant, similar to the methods used in our previous works [45], [65]. Given the number of high BMI participants in this population, the SCG not only had a lower mean SNR when compared with our previous studies but was also observed to have less variability than the PPG SNR; hence, an emphasis was placed on determining the optimal PPGs first. In addition, upon an initial assessment of signal quality, it was observed that when the PPG signal had the highest SNR, typically, the SCG signal did as well—perhaps because acquiring a clean PPG signal inherently hinges on applying consistent pressure. The optimum PPG was selected using a physiologically inspired algorithm to first identify the beats with the top 10% of systolic upstrokes (i.e., maximum of the derivative of the PPG waveform) and then select the remaining beat with the maximum SNR. The SNR was calculated using a noise-to-signal ratio detection algorithm detailed in Inan et al [52]. The methods used to determine the timing references for PTT calculation, the foot of the PPG, and the AO point of the SCG were the same as those used in our previous studies [45], [65]. Specifically, the foot of the PPG was computed using the intersecting tangent method described in the study by Mukkamala et al [18], and the AO point was assumed to be the first peak in each ensemble-averaged window before the foot of the PPG. Occasionally, the SCG signal was manually annotated to impose realistic constraints for the AO point or to ensure that the same morphological peak was consistently chosen for all tasks per participant. Participant-specific SNR thresholds were set to retain only high-fidelity

signals; if the SNR of the SCG, PPG, or ABP beats was not greater than the prescribed cutoff, or if the foot of the PPG was not within a realistic range, then the respective ensemble-averaged waveforms were deemed too noisy for use and that task was not used for PTT calculation. Notably, the continuous reference BP allowed for the ability to evaluate the SNR of the ABP signal and incorporate this quality assessment into our signal processing pipeline to remove beats with low SNR reference measurements. After the entire signal quality assessment process, at least four of the tasks were used for BP estimation per participant. Finally, the PTT was calculated as the difference of the proximal timing reference, AO point of the paired SCG, and distal timing reference, the foot of the selected PPG. In addition to wavelength comparisons, the green and red wavelength PPGs were not used as the IR wavelength wrist PPGs had the highest mean SNR, because of the greater indifference of the IR wavelength to melanin absorption and the ability to capture more pulsatile arteries deeper in the tissue than cutaneous capillaries [18], [71].

In addition, the postexercise recovery period was separated into an early and late rest period based on when the BP reached a consistent value. This allowed us to capture both the immediately heightened CO–induced BP increase postexercise and the recovery back to baseline, while opportunely adding another PTT and BP data point for linear regression.

4.2.3   Statistical Analysis

Simple linear regression was performed independently between wearable participant-specific inverse PTT (PTT^{-1}) and reference diastolic BP (DBP), MAP, or systolic BP (SBP) value pairs, to calculate the calibration coefficients necessary to estimate each of the three BP components per participant; nonlinear models, whereas potentially more accurate,

dictate the need for more calibration points [18], [59]. Therefore, the resulting calibration coefficients—used to estimate BP from the conventional PTT-based BP estimation model shown in Equation 3—are merely the slope (i.e., slope calibration coefficient [K_1]) and y-intercept (i.e., Y-intercept calibration coefficient [K_2]) of the line of best fit [18]. This was identical to the calibration methods used in our previous work [45], [65].

The mean absolute difference (MAD) was computed from the mean of the absolute value of the difference between the estimated and reference BP. The benchmarks for MAD were chosen based on the Institute for Electronics and Electrical Engineers (IEEE) standard for wearable cuff-less BP measuring devices [53]. In addition, the RMSE, calculated as the RMS of the difference between the estimated BP and measured BP, was computed because of its enhanced sensitivity to outliers.

We stratified the entire study population for the demographic comparisons of the calibration coefficients shown in Figure 12, based on four factors (i.e., obesity, sex, race, and age) known to affect arterial stiffness [72]–[77] and therefore the PTT. The participants were split into nonobese and obese groups based on the guidelines from the National Heart, Lung, and Blood Institute of the National Institutes of Health defining a BMI ≥30 kg/m2 as obese [78]. Thus, the nonobese group had a BMI ≤30. To assess differences due to age, we separated the participants into younger (aged ≤40 years) and older groups (aged ≥40 years). Statistical significance (P<.05) between demographic data for each cohort was assessed using an unpaired two-sample, two-tailed t test, as shown in Table 3.

For the demographic DBP calibration coefficient comparisons, a one-sample Kolmogorov-Smirnov test was used on each data point to test for normality, which

determined that none of the data for the comparisons were normally distributed. Then, a Mann-Whitney U test (i.e., Wilcoxon Rank Sum test) was used to assess statistical significance (P<.05) among the unpaired data.

For the PPG wavelength DBP estimation comparisons—only applicable to the second cohort population due to the differences in hardware used—first, a one-sample Kolmogorov-Smirnov test was used on each data point to test for normality, which determined that none of the data for the comparisons were normally distributed. Then, a Wilcoxon Signed Rank test was used to assess statistical significance (P<.05) among the paired data.

4.3   Results

4.3.1   Multimodal Engineering Mechanics of the SeismoWatch

The previous version of the watch, not shown in this thesis, consisted of a 3D printed case embedded with an accelerometer, PDs, and IR LEDs. All sensors were connected to a small external circuit box with straps for the participant to wear around the waist. The output of the analog accelerometer (ADXL354, Analog Devices Inc.) was connected to an AFE in the circuit box. To amplify the SCG signal and prevent saturation of the alternating current components owing to the varying direct current levels, the AFE separated the direct current and alternating current components using a low pass (fc=1 Hz; G=−10 dB) and BPF (fpass=0.2 Hz-40 Hz) in parallel. An analog adder recombined both components. For PPG measurements, the cathode of the PDs (S2386-18k, Hamamatsu Photonics) was connected to transimpedance amplifiers configured as a low-pass filter (fc=12 Hz; G=110 dB) followed by gain and filter stages (fpass=0.5-12 Hz; G=59 dB). Finally, the ECG was

acquired by placing three copper dry electrodes on the wrist band of the watch with two on the inside in contact with the wrist and one on the outside to place the index and middle finger. The two on the inside act as the right leg drive electrode and the positive lead, whereas the outside electrode is the negative lead. All electrodes were connected to an AFE (AD8232, Analog Devices Inc.) for ECG measurements. A microcontroller (Teensy 3.6, PJRC LLC) sampled the output of the accelerometer, PPG, and ECG AFE at 1 kHz. An onboard SD card was used to store the raw data for postprocessing, and a 1.2 Ah lithium-ion rechargeable battery was used to power the system. All instrumentation details were adopted from our previous work, with minor revisions [45].

The updated hardware, pictured in Figure 14, added modalities of sensing (i.e., a gyroscope), included multiple wavelengths of LEDs for comparison with IR, improved the form factor for comfort and ease of use, and featured embedded systems innovations leveraged in this study. A more thorough description of the revised hardware is available in our most recent work [65]. An example of the serviceable automatic LED current scaling algorithm, detailed in our previous work [65], is highlighted in Figure 14. This proved to be an integral part of enabling accurate BP estimation in this study; by adaptively adjusting the LED drive current, we were able to prevent saturation and variable PPG signal quality caused by varying contact pressure and, more importantly, prominent differences in skin tone among participants.
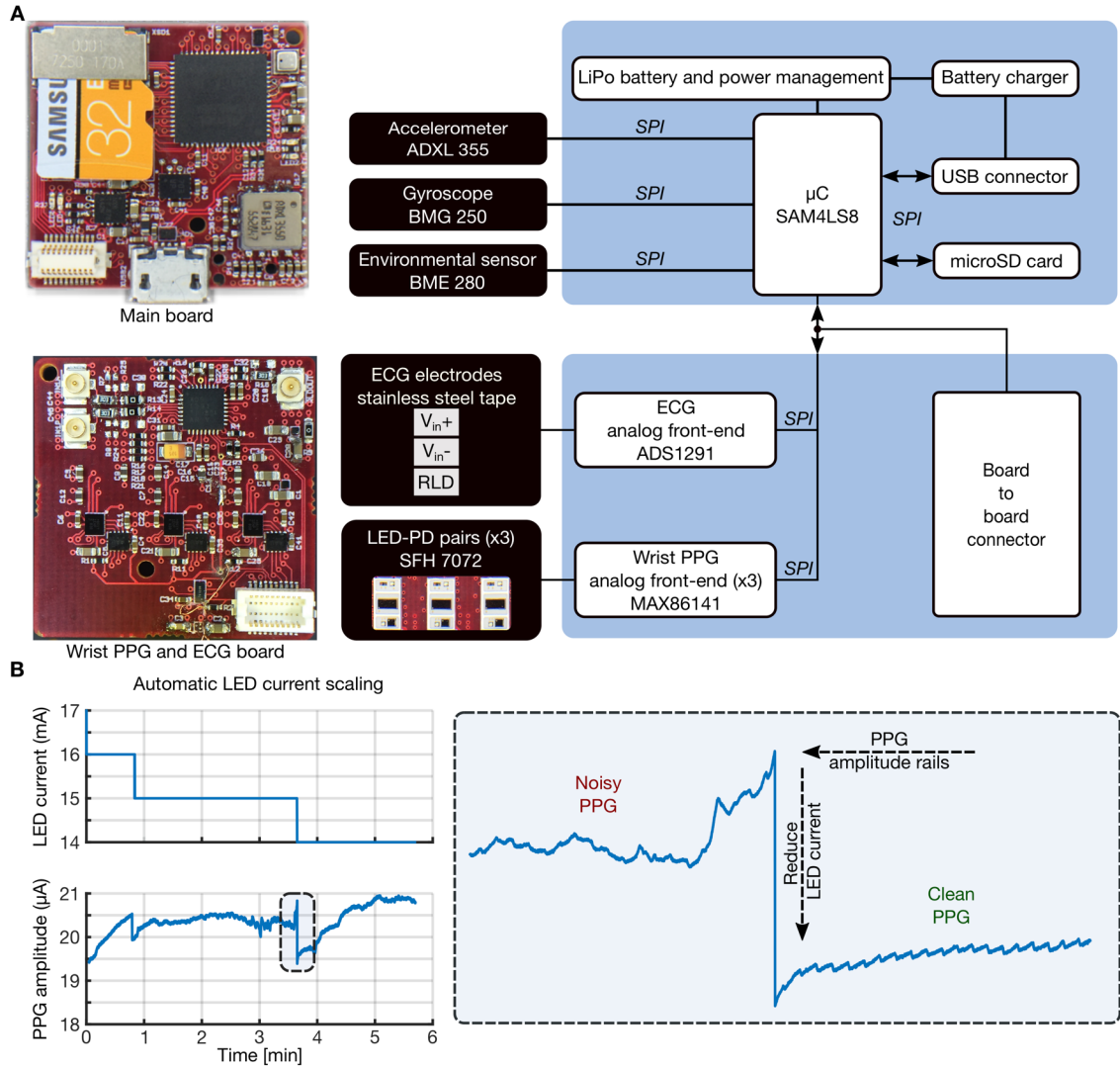
Figure 14. Pertinent multimodal hardware block diagram and adaptive light-emitting diode (LED) scaling. Main board with ATSAM4LS8 microcontroller (μC), ADXL355 triaxial accelerometer, BMG250 triaxial gyroscope, and BME280 environmental sensor using the serial peripheral interface (SPI) for fast communication supporting higher sample rates. Sensor board used to acquire wrist photoplethysmogram (PPG) and electrocardiogram (ECG) signals. Automatic LED current scaling in operation during data collection: showing an increase in contact pressure and subsequent saturation of the photodiode, mitigated by an automatic decrease in LED current and overall consequential improvement in PPG signal quality.

4.3.2   Human Subject Studies in a Diverse Population

64

All applicable results are presented as mean (SD). Figure 11 illustrates the correlation and Bland-Altman plots for our wearable PTT-based BP estimation of MAP, DBP, and SBP across all participants (N=44). The MAD was 2.90 mm Hg, 3.39 mm Hg, and 5.36 mm Hg for DBP, MAP, and SBP, respectively. The mean RMSE was 3.41 (SD 2.01) mm Hg, 3.95 (SD 2.42) mm Hg, and 6.28 (SD 3.44) mm Hg for DBP, MAP, and SBP, respectively. DBP and MAP estimation had better 95% CIs than SBP at 7.99 mm Hg, 9.42 mm Hg, and 14.59 mm Hg, respectively. The mean Pearson correlation coefficient (PCC) was 0.67 (SD 0.16), 0.63 (SD 0.31), and 0.50 (SD 0.41) for PTT-based DBP, MAP, and SBP estimation, respectively.

The MAD for the individual study populations (first cohort=26 participants and second cohort=18 participants) was 2.69 mm Hg and 3.20 mm Hg, 3.21 mm Hg and 3.64 mm Hg, and 5.17 mm Hg and 5.63 mm Hg, for DBP, MAP, and SBP estimation, respectively. The mean RMSE for the individual study populations (first cohort=26 participants and second cohort=18 participants) was 3.19 (SD 1.64) mm Hg and 3.73 (SD 2.48) mm Hg, 3.78 (SD 2.06) mm Hg and 4.18 (SD 2.90) mmHg, and 6.26 (SD 3.25) mm Hg and 6.32 (SD 3.80) mm Hg for DBP, MAP, and SBP estimation, respectively. The mean PCC for the individual study populations (first cohort=26 participants and second cohort=18 participants) was 0.69 (SD 0.15) and 0.65 (SD 0.17), 0.68 (SD 0.23) and 0.55 (SD 0.38), and 0.58 (SD 0.33) and 0.39 (SD 0.49) for DBP, MAP, and SBP estimation, respectively.

The MAD for the 19 Black participants was 3.18 mm Hg, 3.72 mm Hg, and 5.84 mm Hg for DBP, MAP, and SBP estimation, respectively. The mean RMSE for all 19 Black participants was 3.72 (SD 2.41) mm Hg, 4.29 (SD 2.86) mm Hg, and 6.69 (SD 4.03) mm Hg for DBP, MAP, and SBP estimation, respectively. The mean PCC for all 19 Black

participants was 0.64 (SD 0.17), 0.53 (SD 0.38), and 0.37 (SD 0.48) for DBP, MAP, and SBP estimation, respectively.

The MAD for the 10 participants who were obese was 2.69 mmHg, 3.17 mm Hg, and 5.02 mm Hg for DBP, MAP, and SBP estimation, respectively. The mean RMSE for all 10 participants who were obese was 3.28 (SD 2.59) mm Hg, 3.69 (SD 3.00) mm Hg, and 5.71 (SD 4.18) mm Hg for DBP, MAP, and SBP estimation, respectively. The mean PCC for all 10 participants who were obese was 0.65 (SD 0.18), 0.52 (SD 0.48), and 0.39 (SD 0.58) for DBP, MAP, and SBP estimation, respectively.

Figure 12 depicts the boxplots of the DBP calibration coefficients from our estimation model, K_1 and K_2, for four different demographic factors known to affect arterial stiffness: obesity, sex, race, and age. The DBP K_1 and K_2 values for nonobese (N=34) versus obese (N=10) participants are 2.38 (SD 1.99) mm Hg/s versus 1.20 (SD 0.88) mm Hg/s and 61.02 (SD 18.03) mm Hg versus 74.31 (SD 5.14) mm Hg, respectively. The DBP K_1 and K_2 values for male (N=25) versus female (N=19) participants are 2.65 (SD 2.18) mm Hg/s versus 1.40 (SD 0.98) mm Hg/s and 60.16 (SD 20.64) mm Hg versus 69.14 (SD 8.29) mm Hg, respectively. The DBP K_1 and K_2 values for non-Black (N=25) versus Black (N=19) participants are 2.63 (SD 2.21) mm Hg/s versus 1.44 (SD 0.94) mm Hg/s and 60.66 (SD 20.29) mm Hg versus 68.49 (SD 9.98) mm Hg, respectively. The DBP K_1 and K_2 values for young (N=31) versus older (N=13) participants are 2.38 (SD 2.09) mm Hg/s versus 1.47 (SD 0.87) mm Hg/s and 61.96 (SD 19.03) mm Hg versus 69.00 (SD 9.22) mm Hg, respectively.

Both K_1 and K_2 were significantly different between the nonobese and obese populations (P=.045 and P=.008, respectively). The female K_1 values were significantly (P=.04) lower than those of their male counterparts. The K_1 values for Black participants were significantly (P=.047) lower than those of the other races.

For the participants in the second cohort—all Black—with whom we used the newer version of the hardware [65] that included green and red LEDs in addition to the IR, the PCC for DBP estimation was 0.38 (SD 0.34), 0.59 (SD 0.44), and 0.65 (SD 0.17) when using the green (λ=526 nm), red (λ=660 nm), and IR (λ=950 nm) wavelength PPGs for the distal timing reference, respectively. The PCC for the IR and red wavelength PPGs was significantly (P=.01 and P=.048) higher than that of the green wavelength PPGs. However, the corresponding mean DBP RMSE was 3.95 (SD 2.53) mm Hg, 3.11 (SD 2.33) mm Hg, and 3.73 (SD 2.48) mm Hg for green, red, and IR, respectively.

4.4 Discussion

4.4.1 Principal Findings

To the best of our knowledge, this is the first study to accurately estimate DBP and MAP using noninvasive PTT measurements acquired from a holistic population, with considerable differences in body fat percentage, melanin levels, and vascular stiffness associated with age and hypertension. Furthermore, our SBP estimation is sufficient to be clinically recommended for monitoring [53], [79]. We demonstrated the reliability of a convenient method for estimating BP and observed that our calibration coefficients were significantly different in characteristic demographic groups known to have increased arterial stiffness. This study represents a necessary advancement toward remote monitoring

for persons in MUAs by enabling wearable PTT-based BP estimation, including through the comprehensive evaluation of a watch-based form factor conducive to obtaining ambulatory BP measurements in low-resource settings.

4.4.2 Accurately Estimating BP in a Diverse Population Using a Multimodal Wearable Device

We demonstrated the performance of our wrist-worn PTT-based device when used to estimate BP within a diverse population over the course of multiple unique perturbations. Our results for MAP and DBP passed the acceptable benchmarks for the BP estimation error set by the IEEE standard on wearable cuff-less BP estimation devices (MAD≤5 mm Hg) [53]. We were still able to achieve a reliable correlation between PTT and BP even with several demographic factors such as age, melanin levels, and BMI inherently influencing the measured optical-PPG and mechanical-SCG signals.

The DBP estimation remained the most accurate, similar to our previous studies [45], [65]; the foot of the PPG waveform, used as the distal timing reference, indicates the arrival of the pulse wave during end diastole. Similarly, the SBP estimation continued to perform the worst, as the peak of the pulse wave is the fiducial marker of the PPG that occurs during systole; however, the peak is not frequently extracted, as its true timing can be confounded by wave reflection interference, leading to unreliable PTT estimates [18]. Recent studies have demonstrated that the PTT computed using the diastolic foot of the PPG outperforms that using the systolic maximum for both DBP and SBP [56].

The DBP RMSE was relatively similar at both low and high values of DBP, which indicates that the diastolic foot was a dependable timing reference for calculating the PTT,

irrespective of inherent participant-specific differences in BP. Although our SBP estimation was just outside the acceptable limits set forth by the IEEE standard (i.e., MAD=5.36 mm Hg vs 5.0 mm Hg) [53], this error translates to a grade B classification [53] and therefore would still be clinically recommended for monitoring SBP [79]. Furthermore, the SBP range studied was greater than 100 mm Hg, substantially higher than that reported in previous studies in the literature for wearable cuff-less BP estimation, and a combination of different perturbations was used to modulate BP. Using a single perturbation would have led to an improved correlation [18], [20], as in our previous work where we had only used exercise [45]. However, a comprehensive evaluation of this methodology would be incomplete without a procedure consisting of a wide variety of perturbations with different known physiological responses and pathways to modulate BP [20]. In addition, as noted in Figure 10, the exercise perturbation did not apparently produce a marked difference in BP due to several factors: (1) technical limitations in rapid calibration for the reference measurement (i.e., finger-cuff continuous BP) and increased motion artifacts following exercise led to a greater percentage of beat removal in the early exercise section than any other task and (2) exercise does not necessarily consistently modulate BP in a predictable manner due to differences in participant-specific vasoactivity and contractility [18], [80].

Only the DBP was examined for further analyses conducted below because, as previously mentioned, the distal timing reference used (i.e., the foot of the PPG waveform) occurs during diastole and therefore provides the most reliable estimation of DBP out of the three BP components [18]. The dependability of the diastolic foot and our robust DBP estimation were necessary before performing in-depth analyses with confidence. Although

elevated SBP is considered to be the greatest predictor of future cardiovascular risk [81], [82], elevated DBP has nonetheless been shown to independently increase the risk of subsequent cardiac events [81], [83]. In addition, DBP is a greater contributor to MAP, which in older patients with isolated systolic hypertension, when compared with an equivalent increase in pulse pressure, has been shown to be a comparable independent predictor of both stroke and all-cause mortality [84]. Finally, DBP has been shown to be a more significant predictor than SBP of new-onset hypertension in adults younger than 50 years of age [82], [85]–[87]. This suggests that accurate DBP estimation using a wearable device can efficiently be used to incentivize people to make healthy lifestyle modifications earlier in life, central to the World Health Organization's effort to reduce the global prevalence of hypertension [88].

4.4.3 Essential Device Novelties Enabling Reliable PTT Computation

For the first time, we demonstrated that noninvasive PTT measurements are reliable estimators of BP across a wide range of skin tones and BMI. Both DBP and MAP estimation for the 10 participants who are obese and 19 Black participants in this study were well under the IEEE requirement [53]. This was enabled by the highly sensitive hardware, multi-sensor approach, and automated LED current scaling that our custom wearable device offers [65]. The PPG array and adaptive LED current scaling allowed us to automatically mitigate poor signal quality issues due to misplacement, inherent differences in skin tone, and applied pressure that typically corrupts PPG signals. However, the most integral components of our PPG hardware were the IR wavelength LEDs.

We leveraged longer wavelengths of light for deeper penetration into the tissue to robustly acquire the PPG signal from arteries located deeper than the cutaneous vascular bed [18]. Cutaneous arteries are greatly affected by the changes in vascular tone expected from the perturbations we used to modulate BP herein (i.e., cold pressor and exercise). Furthermore, as IR PPGs are more susceptible to motion artifacts than lower wavelength ones [18], [89], our PPG-first signal quality assessment not only avoided these motion artifact corrupted waveforms because of their low SNR but also avoided moments where the SCG quality would naturally suffer as well. However, even the red PPGs had a considerably larger SD in their PCC than the IR PPGs, possibly because the IR wavelength, when compared with red, is less sensitive to the oxygen content of hemoglobin and has approximately half the skin absorption coefficient in Black individuals [18], [71]. Despite statistically significant differences in the PCC using IR and red PPGs rather than green PPGs, the actual DBP RMSEs were comparable. This implies that when using the green PPGs for participants with a low PCC, our signal quality assessment algorithm removed beats with greater BP variability, resulting in a lower SD of DBP and consequent RMSE. Although even green wavelength PPGs have demonstrated the ability to reliably extract heart rate across a wide variety of skin tones [90], our data suggest that these shorter wavelengths cannot be used to dependably compute the PTT in a diverse population. In addition, although unconventional, our watch was placed on the ventral side of the wrist, which allows for both higher quality, convenient SCG acquisition and enhanced PPG SNR due to viable access to the radial artery and less melanin content than the dorsal side [91]. Therefore, existing smartwatches, beginning to slowly incorporate cuff-less, noninvasive

BP methodologies, may face even greater difficulties in achieving accurate PPG measurements across a broad range of skin tones.

Finally, our physiologically inspired PPG selection algorithm—to first select the PPG signals with the greatest systolic upstrokes—had an important role in reducing the BP estimation error. PPG waveforms with greater systolic upstrokes (i.e., maximum derivative of the PPG waveform) offer improved PTT estimates and are key indicators of BP stemming from larger, more pulsatile, elastic arteries with greater distensibility [18], [92]. In addition, several recent ML approaches to use the PPG signal for BP estimation have shown that the systolic upstroke is one of the most important features of the waveform [93], [94]. Hence, the selection algorithm, by extracting information from these more reliable and clinically important arteries, was a central part of our ability to notice the demographic differences in arterial stiffness rooted in our calibration coefficients.

4.4.4   Calibration Coefficients Capture Demographic Differences in Arterial Stiffness

We observed that the participant-specific calibration coefficients used in the standard linear PTT-BP estimation model for DBP, shown in Equation 3 (i.e., K_1 and K_2), are significantly different between subpopulations with large variations in demographic factors known to affect arterial stiffness. We selected the four demographic categories (i.e., obesity, sex, race, and age) based on the literature, emphasizing these as major determinants of differences in arterial stiffness and therefore risk factors for hypertension [22], [72]–[75], [77], [95], [96].

The K_1 value (i.e., the slope of the line of best fit) is indicative of the underlying baseline vascular stiffness, whereas K_2 (i.e., the intercept) represents the inherently

correlated bias in baseline BP [18], [97], [98]. At the same BP, persons with greater arterial stiffness have inherently faster pulse wave velocities (PWVs) and therefore shorter PTTs than persons with normal arterial stiffness [18]. The K_1 value mitigates these differences in PTT-based estimation by capturing the intrinsic participant-specific arterial stiffness to output similar BP values. Therefore, with increasing arterial stiffness, we expected to find a lower K_1 value and a higher K_2 value, as observed in the PWV literature [97], [98].

Obesity was the only comparison for which the differences in the K_1 and K_2 calibration coefficients were statistically significant. This coincides with the literature stating that obesity is one of the greatest age-normalized risk factors and contributors to arterial stiffness [99]. Otherwise, only the K_1 values in the sex and race comparisons were statistically significant between the groups. Although it has been shown that both females and Black individuals have greater arterial stiffness than similar-age males and White individuals [73], [76], [77], these two comparisons should be re-evaluated after increasing our recruitment. Approximately 47% (9/19 participants) of both the female and Black population were also obese. The age comparison was not statistically significant, although the older population followed a similar trend of a lower K_1 and higher K_2. This finding is not surprising, as significant differences in arterial stiffness and substantial augmentations in arterial remodeling are typically examined in participants older than 50 years of age [74], [100].

4.4.5 Limitations and Future Work

4.4.5.1 Refining Population Demographics and Investigating PTT, K_1, and K_2 as Potential Digital Biomarker of Arterial Stiffness

Overall, although this data set captured a more representative population in the range of end users for which consistent BP monitoring is recommended [58], our PTT-based device should be further tested in an exclusively older (i.e., age>50 years), morbidly obese (i.e., BMI>40 kg/m2), and hypertensive population—with even distributions across sex, race, and skin tones along the Fitzpatrick scale—to truly understand the limits of this technology and supplement the findings herein.

Early vascular remodeling due to the demographic factors investigated, not to mention socioeconomic factors affecting MUAs [21], [22], predispose individuals who are obese and Black individuals to greater lifetime cardiovascular risk [72], [77], [99], [101], [102]. Therefore, future PTT-based BP estimation studies should closely monitor the calibration coefficients, K_1 and K_2, as potential intermediate digital biomarkers for longitudinal monitoring and the comparison of arterial stiffness among different persons [12]. Eventually, even PTT measurements, as PWV is already an independent predictor of arterial stiffness [103], may indicate subclinical differences in vascular resistance due to early stage arterial remodeling, the main precursor to hypertension [74].

4.4.5.2   Reducing the Burden of Calibration

Consistent recalibration poses a practical concern for PTT-based BP estimation. Hence, future studies should focus on evaluating the timeframe for which participant-specific calibration curves can reliably estimate BP and whether interparticipant and population-level curves can be sufficient. However, given the value of interpreting the calibration coefficients presented, caution should be exercised due to the trade-off of sacrificing this potential usefulness when using generalized interparticipant models. Furthermore, the

individual effects of the perturbations used to modulate BP in this experiment should be scrutinized, along with other exercises shown to substantially change BP [104]–[106]. The goal is to use perturbations that can consistently be leveraged to increase the dynamic range of BP measurements for calibration—critical to achieving optimal estimations at home in our previous work [65] and are achievable in low-resource settings.

4.4.5.3 Leveraging ML and Hardware Advancements for Robust SCG AO Detection

Similarly, to the instrumental role of the physiologically inspired PPG selection algorithm, further exploration into automated SCG fiducial point detection algorithms may help extract the most informative SCG signals. Specifically, the SCG can be greatly affected by inaccurate placement of the watch; however, recent advancements using ML techniques have shown that the SCG waveform is modulated in a predictable manner during these placement inaccuracies [107]. Therefore, by interpreting these findings, one might be able to convert the measured SCG to the archetypal SCG or use a template-matching localization approach [108] for each participant before extracting salient features from the optimal waveform.

In addition, annotating the exact AO point can be challenging because the signal not only has appreciable interparticipant variability, especially in a population with considerable differences in BMI, but can also be corrupted by motion artifacts. Although our technique for extracting the AO point has led to a high correlation between PTT and BP, in both our recent work [65] and this one, for a few sessions, we manually annotated the SCG to impose realistic constraints for the range of the PEP and selected a consistent morphological peak across all tasks per participant. Eventually, robust identification of this

timing reference is necessary for reliable automatic PTT computation, as the main advantage of using the PTT over the pulse arrival time (i.e., the time from the R-wave of the ECG to the diastolic foot of the PPG) for BP estimation is its ability to account for changes in the nonnegligible cardio-electromechanical delay, that is, the PEP [18], [109]. Furthermore, examining the other sensor data available at our disposal, such as filtering the SCG in a higher bandwidth (i.e., fpass=30-125 Hz) to retain the phonocardiogram (PCG) signal indicative of valve closures, using the three-axis gyrocardiogram or simply the other axes of the SCG, could prove to help with improving PEP estimation as shown in previous work [45], [49].

4.5 Conclusions

We have demonstrated that a wrist-worn device, using noninvasive PTT estimates, can reliably and conveniently track BP in a diverse population. Leveraging the ubiquity of wearable devices can empower users to make healthy lifestyle modifications such as exercise, which can contribute to a significant reduction in arterial stiffness [72], [110] by providing consistent feedback on progress [111]–[113]. In addition, digital health technologies that accurately estimate BP could potentially be used to titrate BP medications for patients with hypertension from the comfort of their homes [12], [64]. In addition to these broader impacts, the knowledge gained from this study—especially when combined with the advent of low-profile, flexible electronics capable of robustly detecting physiological biosignals [114]–[117]—represents a significant step toward the unobtrusive monitoring of BP in ambulatory settings and health equity for persons in MUAs.

CHAPTER 5.   TOWARD SMART WEARABLE SEISMOCARDIOGRAPHY-BASED ASSESSMENT OF STROKE VOLUME IN CONGENITAL HEART DISEASE

5.1   Introduction

Patients with CHD are at risk for the development of low CO and other physiologic derangements, which could be detected early through continuous SV measurement. Unfortunately, existing SV measurement methods are limited in clinic because of their invasiveness (e.g., thermodilution), location (e.g., cardiac magnetic resonance imaging), or unreliability (e.g., bioimpedance). Multimodal wearable sensing, leveraging the SCG—a sternal vibration signal associated with cardiomechanical activity—offers a means to monitor SV conveniently, affordably, and continuously. However, it has not been evaluated in a population with significant anatomical and physiological differences (i.e., children with CHD) or compared against a true gold standard (i.e., CMR).

We sought to evaluate the use of SCG to measure SV in a unique population of patients with CHD using our convenient wearable biosensor. In this work, simple, intuitive, physiologically inspired ECG and SCG features derived from this wearable biosensor were used, along with ML, to estimate the baseline SV of patients with CHD undergoing a clinically indicated CMR. In addition, this work provides greater insight into how cardiomechanical signals such as the SCG are modulated in CHD patients with severe anatomical and physiological differences. Ultimately, it will yield a framework, along with the pertinent features necessary, for estimating SV using wearable ECG and SCG signals

toward noninvasive, continuous, and ubiquitous monitoring of this vital hemodynamic parameter.

5.2 Methods

5.2.1 Multimodal Hardware Design
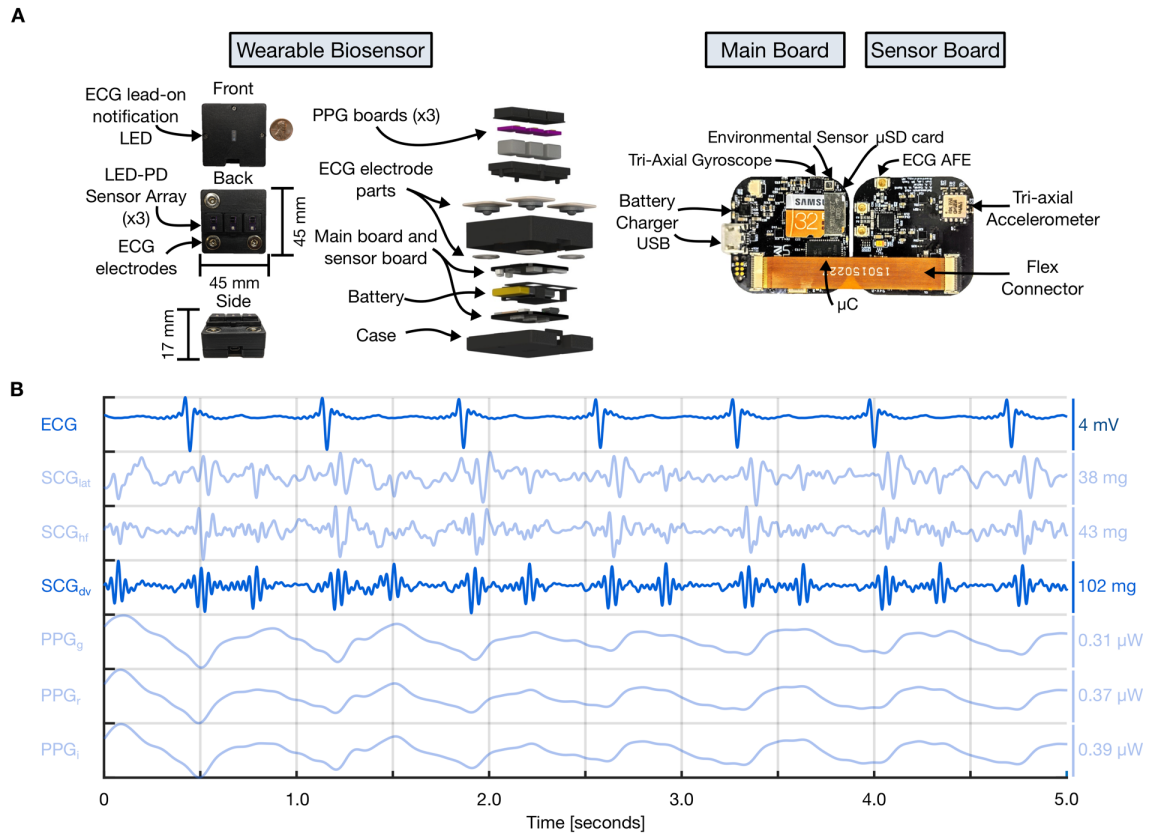
Figure 15. Wearable multimodal hardware engineering mechanics. A, Pertinent multimodal hardware diagram. Final wearable biosensor iteration with exploded view detailing photoplethysmogram (PPG) components, gel-electrode electrocardiogram (ECG) connectors, lithium-polymer battery, and printed circuit boards (PCBs). Main PCB with ATSAM4LS8 microcontroller (µC), BMG250 triaxial gyroscope, and BME280 environmental sensor, micro secure digital card (µSD), and bq24232 battery charger. Sensor PCB—connected to main PCB via flexible connector—with ADXL355 accelerometer, ADS1291 analog-front-end, and magnetic wire connections to separate PCB containing SFH7016 multi-chip light-emitting diode (LED) and SFH 2703 photodiode (PD) used to acquire triaxial seismocardiogram (SCG), single-lead ECG, and multi-wavelength sternum PPG

signals, respectively. B, Sample five seconds of filtered wearable signal data from a single-ventricle patient with corresponding amplitudes shown. In order from top to bottom: ECG, lateral SCG (SCG$_{lat}$), head-to-foot SCG (SCG$_{hf}$), dorso-ventral SCG (SCG$_{dv}$), green PPG, red PPG, infrared PPG signals. The darker blue ECG and SCG$_{dv}$ signals are those utilized in this study.

The electronic hardware used in this study is an updated and miniaturized version to that described in detail in [65]. Updates focused on decreasing the overall device size to accommodate a pediatric population. From a sensing standpoint, identical sensors and AFEs, were utilized in this study to acquire the ECG (ADS1291, Texas Instruments Inc., Dallas, Texas, USA) and SCG (ADXL355, Analog Devices Inc., Norwood, Massachusetts, USA) signals across all versions of the hardware, and the same three-dimensional printing filament—polylactic acid—was used to manufacture the device housing. Data was saved locally on an internal SD card and downloaded over USB using the custom software application mentioned in [65].

Overall, the key upgrades from the hardware used in [65] include the addition of a flexible connector, two main sensing PCBs as opposed to three, eventually the use of gel-electrode ECG, a separate PPG sensor board with newer discretized PDs and LEDs, and a foam-based spring backing mechanism for improved PPG sensing. However, the PPG signals were not explored in this work and therefore—to prevent detracting from the focus of this work—the specific details of that hardware will not be expanded on further. In the newer version, shown in Figure 15, the sample rate of the SCG was increased to 2 kHz to provide a bandwidth of 500 Hz; the SCG sampling frequency was adjusted to capture higher frequency vibrations that may eventually be utilized to monitor patients with heart murmurs—a subsection of the CHD population at a greater risk of decline. Unfortunately, as with a proof-of-concept study, the hardware required few—mostly device housing—

modifications at different stages of the study before reaching the current prototype pictured in Figure 15. Most importantly, the earlier version of the hardware utilized in this study featured the use of a dry electrode ECG, using stainless steel tape, for which the device was pressed against the chest of the patient to acquire the biosignals, while the later version used standard infant AgCl gel electrodes (Kendall HP69, Medtronic PLC, Dublin, Ireland) to adhere to the chest, eliminating the need for an extra contact force. To help mitigate any issues from differences in contact pressure with the dry electrode version, in addition to having the same group of few clinicians collect all data, only segments of the signals where the dry electrode acquired ECG—which is susceptible to variations in contact pressure due to changes in skin-electrode-impedance [118]—had a consistent amplitude were analyzed. Devices with both versions of the ECG featured a firmware modification which leveraged the lead-on detect feature of the ECG chip and would toggle a LED facing the clinician between red and green for when ECG lead was detected as off or on, respectively. This also removed the possibility of accidentally applying an excessive amount of pressure without knowing whether a signal was being acquired.

5.2.2   Study Protocol

A detailed overview of the study design is provided in Figure 16. This study was conducted under Institutional Review Board protocol STU2019-1280 at the University of Texas Southwestern Medical Center. We approached consecutive CHD patients undergoing a clinically indicated CMR and obtained written consent and assent as appropriate. For this study, data were analyzed from volunteers who had both a supine wearable and CMR measurement. We placed the wearable chest-worn biosensor on the patient while they were supine, if possible, for a maximum of three minutes both before

and after their CMR scan. If the patient was undergoing the scan under anesthesia, the device was placed 10 minutes after induction of anesthesia to allow for them to reach physiological equilibrium [119]. During the clinical CMR scan, left ventricular and right ventricular SV—and, if recommended, aortic valve forward flow—were collected per clinical protocols [120]. Only either pre-CMR or post-CMR supine data were examined in this work, with most data taken from the pre-CMR measurement to ensure consistency, unless unavailable. The aortic forward flow measurement was prioritized over the volumetric one, if acquired. The systemic ventricle—connected to the aorta and responsible for CO—was labeled by the cardiologist and SV data from this ventricle along with the instantaneous HR taken from the corresponding CMR measurement, for either the volumetric or aortic forward flow measurement, were used as the reference SV and HR measurement, respectively.
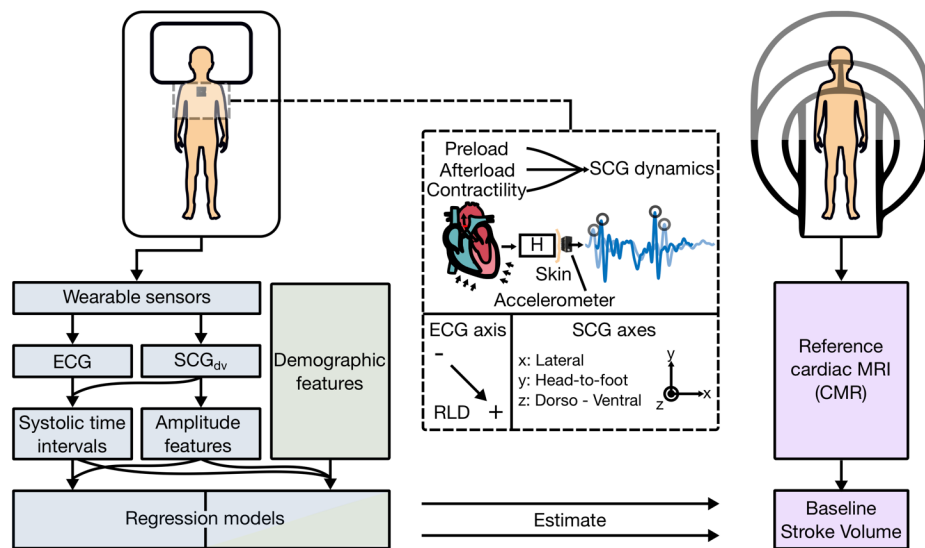
Figure 16. Concept overview. Study design showing wearable biosensor placement when supine and asynchronous reference cardiac magnetic resonance (CMR) measurement. Seismocardiogram (SCG) mechanistic overview detailing modulation due to cardiac physiology, acquisition with an accelerometer, and sensing axes for

electrocardiogram (ECG)—negative, positive, and right-leg-drive (RLD) electrodes—and tri-axial SCG signals. Analysis pipeline—from sensor input to model estimation of stroke volume (SV)—for wearable (blue), demographic (green), and CMR (purple) data.

5.2.3 *Signal Processing*

A signal processing block diagram is depicted in Figure 17. Pre-processing consisted of bandpass filtering the ECG and the dorso-ventral axis of the SCG signal between 5-30 Hz and 0.8-30 Hz to remove their respective out-of-band noise. The SCG was also filtered into a higher frequency bandwidth 30-125 Hz to produce a signal hereafter referred to as high-frequency SCG, which is more closely representative of the PCG. In turn, this wider bandwidth accelerometer signal is capable of picking up on higher frequency vibrations, coupled to the acoustics of the PCG, thus offering a more reliable timeframe to estimate aortic valve opening and closing events [45], a common technical challenge in SCG processing [65]. After filtering, all signals were resampled to 1 kHz. The R-peaks of the ECG were used to segment the SCG and high-frequency SCG signals into different heartbeats. The SCG and high-frequency SCG heartbeats were ensemble averaged using 30 heartbeat windows with 50% overlap—to reduce zero-mean noise, account for respiratory induced variability in SCG signals, and improve the consistency of amplitude features—before selecting the highest signal-to-noise-ratio beat later used to extract the features shown in Table 4.
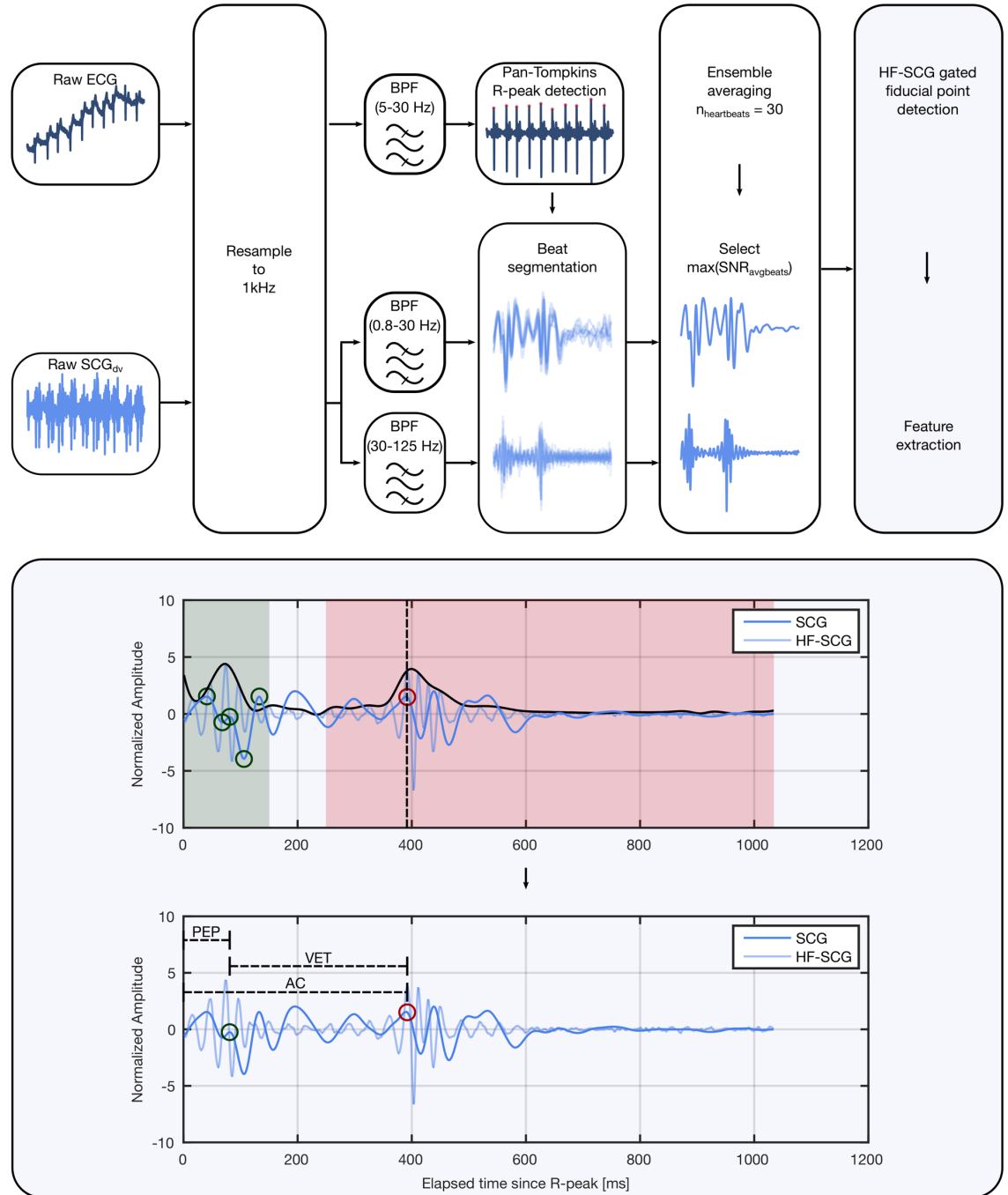
Figure 17. Signal processing pipeline. Block diagram of signal processing overview showing interpolation of electrocardiogram (ECG) and seismocardiogram (SCG) signals acquired from the wearable before bandpass filtering, R-peak detection, heartbeat windowing, and signal quality assessment using the signal-to-noise ratio (SNR). Illustration of the custom high-frequency SCG (HF-SCG)—indicative of valve closures—assisted feature selection algorithm, helping to locate key fiducial points such as the aortic valve opening (AO) and aortic valve closure (AC) on the

SCG—used to compute the pre-ejection period (PEP), ventricular ejection time (VET), and the AC. Additionally, the search radius for the AO (green) and AC (red) algorithm as well as their candidate points are shown.

Table 4. Physiological features and corresponding measurement system

Feature name	Measurement system
Heart rate (HR)	Both Reference CMR and Wearable System
Pre-ejection period (PEP)	Wearable System
Ventricular ejection time (VET)	Wearable System
Timing of aortic valve closure (AC)	Wearable System
Root-mean-square power during PEP (RMS$_{PEP}$)	Wearable System
Root-mean-square power during VET (RMS$_{VET}$)	Wearable System
PEP-to-VET ratio (PEP/VET)	Wearable System
VET-to-PEP ratio (VET/PEP)	Wearable System

All signal processing and feature extraction was carried out in MATLAB 2018a (MathWorks, Natick, Massachusetts, USA) and entirely automated. A high-frequency SCG signal more closely related to the PCG was extracted for this analysis. The PCG, typically acquired from digital stethoscopes, is a wide bandwidth, high-frequency acoustic signal that captures heart sounds (i.e., S_1 and S_2) and obtains information of valve closures when placed at specific auscultation sites. Although, the PCG should be acquired using a wide-bandwidth, piezoelectric accelerometer (i.e., a contact microphone) rather than the capacitive, direct current micro-electro-mechanical systems accelerometer used herein, the sampling rate of the accelerometer was increased to provide this bandwidth. First, the R-peaks of the ECG—marking ventricular depolarization—were found using Pan-Tompkins's algorithm and used to determine the wearable HR. Then the SCG and high-frequency SCG signals were segmented into different heartbeats using and beginning with

the detected R-peaks of the ECG. Due to the large differences in HR in this dataset, all of the heartbeats were zero-padded to a fixed length of 1300 ms, based on the slowest HR in the dataset. Next, the SCG and high-frequency SCG heartbeats were ensemble averaged using 30 heartbeat windows with 50% overlap—to reduce zero-mean noise, remove respiratory induced variability, and improve the consistency of amplitude features—before selecting the highest SNR beat—calculated using the algorithm in [52]. First the envelope of the high-frequency SCG was computed which provided the profiles for the conventional heart sounds S_1 and S_2. The algorithm for detecting the AO point on the max SNR SCG beat was the same as that used in [45], where the AO was detected by finding the nearest zero-crossing after the peak of the high-frequency SCG envelope between 0 and 150 ms; the AC point was determined by finding the most consistent peak of the high-frequency SCG itself between 250 ms to the end of the beat. The AO point resembles the PEP with the difference between that and the AC point being the VET. Two other reciprocal features, PEP/VET and VET/PEP—systolic marker robust to differences in HR–are the quotient of the PEP and VET. Two interpretable systolic amplitude features were calculated as the RMS amplitude of the SCG during the PEP and during the VET. In total 9 systolic features were extracted from the wearable signals. Note that the HR from the CMR was added as a feature, due to both the inability to acquire continuous measurements with the wearable patch during the CMR—because of magnetic interference and injury— and due to expected high accuracy in HR estimation when using wearable ECG during baseline measurements, as a closer measure of the HR during the reference measurement.

Leveraging surrounding physiological information can contextualize and improve the estimation accuracy of wearable measurements. The SV measurement from the CMR, is

computed from a composition of several images which are obtained a relatively slow sampling rate. Therefore, due to respiratory induced variability in SV readings—stemming from changes in venous return, preload, and HR—clinicians typically ask patients to hold their breath. However, as imaginable, for younger children this is obviously not possible. Instead, multiple scans are taken, are the resulting images are averaged before computing SV from the averaged image. Similarly, when using wearable measurements to accurately estimate SV compared to CMR readings should also factor in respiratory variability by averaging over a larger timespan—such as the 30 heartbeats employed in this analysis.

5.2.4   Machine Learning Regression Analysis

Ridge regression was utilized to estimate SV due to its ability to handle multicollinearity—a trait common amongst systolic time intervals—as well as provide feature importances with reduced complexity simply from its weights as a linear model. To avoid data leakage, a 80%-20% fixed training-testing scheme (i.e., 36 patients for training, 9 for testing) was determined using a true random number generator (RANDOM.ORG, Dublin, Ireland). A 10-fold cross-validation on the training set was used to perform the grid search necessary for hyperparameter optimization. Forward feature selection, on the training set, was used to reduce the feature set from 14 down to nine features by examining the coefficient of determination, through simple linear regression between ECG and SCG features and SV. Different ridge regression models, trained on a combination of feature sets, each with their respective optimized lambda hyperparameter from the 10-fold cross validation on the training set, were used to estimate SV. Specifically, we began by examining a model that was merely trained on demographic features alone (i.e., body surface area and age)—due to their well-known correlation to CO [121]—which

assessed the ability to quantify SV without the use of a wearable biosensor at all. Next, we tested using ECG features—namely HR—to assess the estimation accuracy when using solely a conventional metric that is readily, remotely, and continuously available through Holter monitors. Then, we tested our novel approach by adding SCG features to the ECG model to provide for a holistic evaluation of both the electrical and mechanical aspects of cardiac health. Finally, we have provided various combinations of these wearable biosensor and demographic feature sets to determine whether the easily accessible demographic information can augment model estimation.

To assess these model performances, we computed the RMSE and the coefficient of determination (R^2) between the estimated SV and true CMR SV in the held-out test set that was unseen to the ML algorithm until final testing. Percent error was calculated for the highest performing model given the guidelines for CO measurement devices per Equation 7 below with a percent error less than 30% regarded as accurate [122]. Feature importances were derived from the magnitude of the weights from ridge regression, shown in Figure 19, and permutation importances—iterated 1000 times—were also computed and are provided in Figure 20.

$$PE = \left(\frac{1.96 * (SD\ of\ bias\ between\ CMR\ and\ wearable)}{0.5 * (Mean\ SV_{CMR} + Mean\ SV_{wearable})} \right) * 100 \qquad (7)$$

All ML and CV was performed in Python 3.0 using scikit-learn ridge regression and grid search packages, respectively. Despite a considerable sample size with respect to other SCG literature—especially given the diversity of demographics and diagnoses in such a diseased population—due to a small number of overall datapoints for a ML problem, multi-

variate ridge regression was chosen as a more interpretable model to estimate SV. Ridge regression is similar to multiple-linear regression but with a regularization penalty—commonly referred to as lambda—that penalizes the model to prevent overfitting to the training data, thereby hopefully improving model generalizability.

10-fold CV was chosen as a commonly regarded robust method for optimizing hyperparameters and given that each subject had only one datapoint there would be no overlap of subject-specific data in each fold. To approximately balance and have a representative number of the number of single-ventricle patients in the training and testing set based on their size, originally during the data collection we again randomly split them into groups of four and three, respectively. However, after the final data was collected, a last single-ventricle patient was added to the training set to achieve a perfect 80%-20% split, hence a slight imbalance.

When selecting features for biomedical ML problem with a small dataset size there is a greater importance placed on not only selecting a few features that can explain a lot of the variance but also ones that can be clinically understood. Therefore, the original feature set of predictor variables consisted of 14 features that were chosen based on those with strong overlap between commonly used SCG features in existing literature and those that are simple and intuitive to cardiologists.

Both training and testing set features were normalized based on the training set mean and standard deviation. The hyperparameter lambda for the highest performing model, which combined ECG and SCG features, came out to the maximum regularization penalty of 1.0.

5.3 Results

We enrolled 57 and successfully acquired both supine wearable and CMR data from 45 patients. Their detailed subject demographics are presented in Table 5.

Table 5. Overview of patient demographics and clinical parameters of cardiovascular function for study participants.

Demographics and cardiovascular parameters	Training set (n=36)	Held-out test set (n=9)	*P* value
Sex, n (%)			
Male	22 (61)	6 (67)	N/A[b]
Female	14 (39)	3 (33)	N/A
Height (cm), mean (SD)	151.3 (26.6)	163.1 (16.0)	.21
Weight (kg), mean (SD)	56.3 (26.0)	59.2 (19.7)	.76
Body surface area (m²), mean (SD)	1.52 (0.48)	1.63 (0.34)	.52
Age (y), mean (SD)	15.0 (7.9)	14.7 (2.6)	.90
Stroke volume[c] (mL), mean (SD)	68.8 (32.34)	78.19 (24.81)	.42
Cardiac output[c] (L/min), mean (SD)	4.94 (1.88)	5.01 (0.84)	.92
Ejection fraction[c] (%), mean (SD)	0.57 (0.08)	0.59 (0.12)	.51
Reference heart rate (bpm), mean (SD)	76.1 (14.2)	67.7 (14.8)	.12
Single ventricle, n (%)	5 (14)	3 (33)	N/A
Systemic ventricle, n (%)			
Right ventricle	6 (17)	2 (22)	N/A
Left ventricle	30 (83)	7 (78)	N/A

[a] Statistical significance between training and testing sets in values, where applicable, was computed using an unpaired t-test.
[b] N/A: not applicable.
[c] Values for systemic ventricle data shown.

The regression model performance—the coefficient of determination and RMSE—for the training (i.e., 10-fold CV) and testing set for all feature sets are shown in Table 6. The test set performance, when combining features from both the ECG and SCG modalities, improved upon that of the ECG model alone (R^2=0.76 and RMSE=11.48 mL vs. R^2=0.69 and RMSE=13.05 mL) and substantially upon the demographic one (R^2=-0.10 and RMSE=24.56 mL). However, the ECG only model still outperformed the SCG only model (R^2=0.20 and RMSE=20.51 mL). To put the significance of these low RMSEs into context, the dynamic range of measured SV in the training and test set were 146.5 mL and 74.8 mL, respectively. The regression and Bland-Altman plot for the highest performing model, combining ECG and SCG features to estimate SV, are shown in Figure 18. The percent error—the metric that is used by CO measurement guidelines—for this highest performing model was 28%, within the acceptable criteria of 30% [122]. By contrast, the percent error for the ECG only model was outside the threshold for accuracy at 31%.

Table 6. Ridge regression performance using different feature sets

Feature set	10-fold CV training set R^2	Held-out test set R^2	RMSE [mL]
ECG	0.47	0.69	13.05
SCG	0.22	0.23	20.51
Age + BSA	0.72	-0.10	24.56
ECG + SCG	0.49	0.76	11.48
ECG + SCG + Age + BSA	0.88	0.27	19.94
ECG + SCG + BSA	0.74	0.46	17.20

The demographic feature model has a stark difference between training (R^2=0.72) and testing (R^2=-0.10) performance—a clear sign of overfitting. Therefore, combining the

demographic information with ECG and SCG features improved their training set performance(R^2=0.88), but not the test set performance (R^2=0.27). However, as presented in Table 5, there was no significant difference, between the demographics of the training and testing set.
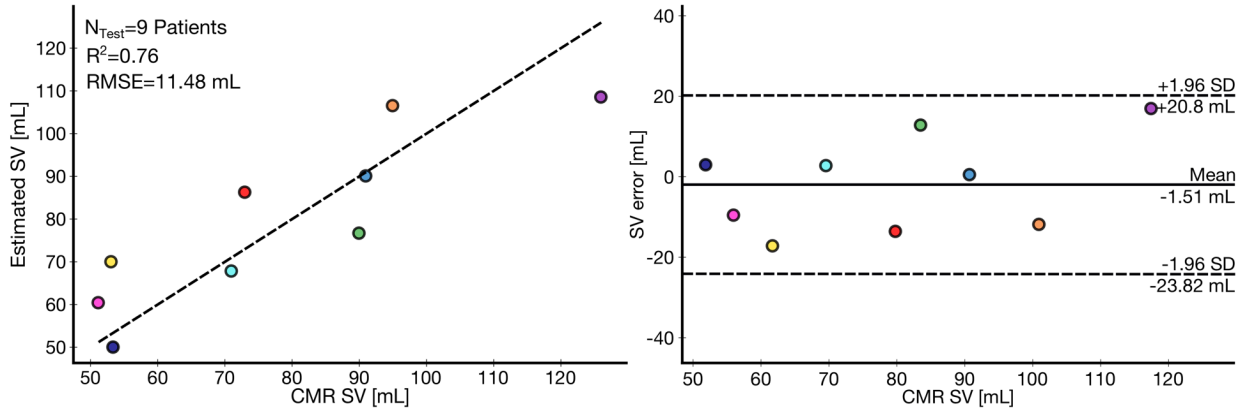
Figure 18. Wearable stroke volume (SV) estimation results. Correlation and Bland-Altman plots between wearable signal estimated SV and the cardiac magnetic resonance (CMR) imaging SV for held-out test set of nine patients. The coefficient of determination (R^2=0.76) and root-mean-square error (RMSE=11.48 mL) are shown.

The feature importance based on the magnitude of the weights from the ridge regression model are shown in Figure 19. Other than HR the most important features are either the PEP, VET, or a ratio derived from the combination of them. The permutation importances, given in Figure 20, were comparable to the magnitude of the weights from ridge regression, however, with VET and PEP having opposite ordering in importance.
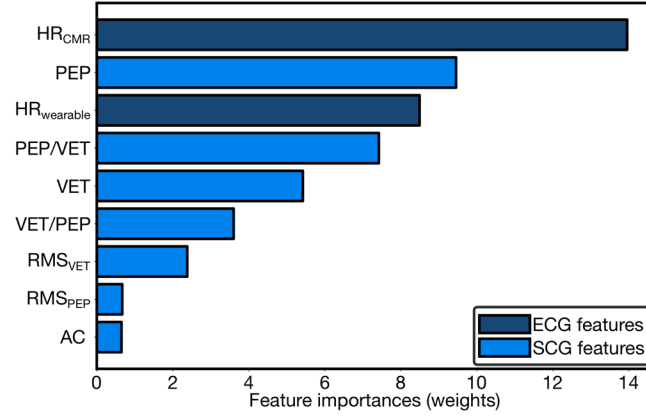
Figure 19. Feature importances for stroke volume (SV) estimation model. Feature importances for wearable system from magnitude of ridge regression weights ranked in order from top to bottom and color-coded by wearable sensing modality—electrocardiogram (ECG) and seismocardiogram (SCG) signals.
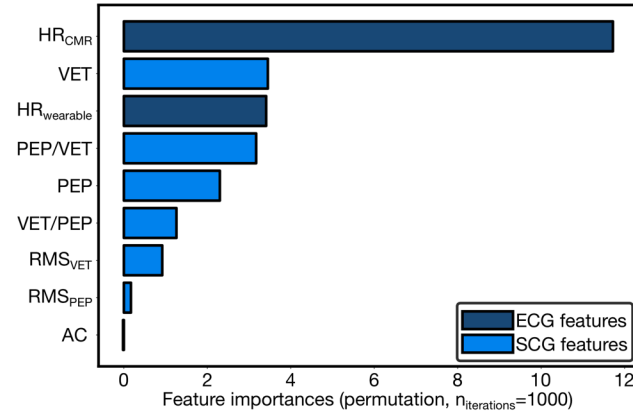
Figure 20. Permutation feature importances for stroke volume (SV) estimation model. Permutation feature importances for wearable system with features randomly shuffled 1000 times, ranked in order from top to bottom, and color-coded by wearable sensing modality—electrocardiogram (ECG) and seismocardiogram (SCG) signals.

5.4   Discussion

In this study, we show that a combination of SCG and ECG parameters, obtained noninvasively, can estimate SV in patients with CHD undergoing CMR with sufficient accuracy per CO measurement guidelines [122]. This work represents a necessary

advancement toward both more holistic wearable SV estimation for diagnostics and remote monitoring for CHD patients. Furthermore, our study is novel in using SCG in children and those with CHD; other studies have focused on structurally normal hearts. Specifically, although it has been shown previously that noninvasive ECG and SCG measurements can be used to accurately estimate SV [39], this relationship had not been examined in a diverse population of patients with structural heart defects and compared against a true gold standard measurement. Here, we evaluated the future utility of a convenient method for estimating SV and observed that there was a strong correlation between simple, highly interpretable SCG features and SV, across a wide range of CHD diagnoses, ages, and anatomical differences. We further achieved accurate estimation of SV in a completely held-out test set by using a regression model that combined both electrical and cardiomechanical wearable features—producing performance superior to that of either feature subset alone.

5.4.1   Wearable Multimodal Signal Features Can Accurately Estimate Baseline SV in a Completely Held-out Test Set

Wearable features were strongly correlated to baseline gold standard CMR SV in a heterogenous population of CHD patients. Furthermore, with an overall 28% error, we were able to achieve an accurate estimation of SV—based on the criteria set forth by CO measurement guidelines—in a completely randomized held-out test set [122]. This SV estimation model trained on multimodal wearable signal features and tested on unseen data is of greater utility than a purely correlation-based result. Additionally, for the Bland-Altman analysis, all estimations were within the limits of agreement indicative of high model precision. Meanwhile, existing inconvenient methods—although more

comprehensively evaluated—such as transesophageal Doppler and NICCOM methods have estimation errors of greater than 40% [123]. In the field of physiological research and biomedical signal processing, to be able to accurately compare baseline measurements to absolute values in clinical parameters across a subject population is extremely difficult and rarely performed. Typically, a perturbation or intervention are leveraged to modulate physiological properties, in this case hemodynamics, which allows for a greater dynamic range and ability to track subject-specific changes in waveform morphology, usually resulting in higher accuracy. In this study, the comprehensive age range and diagnoses— representative of higher-risk children and adults with CHD, who would be undergoing CMR—not only adds difficulty in hardware design, but also contributes to a high intersubject variability. Eventually, if the device were to be utilized to obtain continuous, noninvasive measurements, perhaps in the case of monitoring patients with CHD post-surgery for low CO syndrome, then tracking subject-specific changes in SCG signals would suffice to monitor status, predict exacerbation, and offer personalized healthcare without a specific gold-standard baseline assessment. Generally, subject-specific models will outperform globalized models, although the reduced complexity of the latter may prove to be beneficial in certain scenarios.

Our low RMSE for the test set of 11.48 mL—underscored by the wide dynamic range in SV of 74.8 mL within—demonstrates that our estimation is relatively robust to outliers. Hence, the inability to explain these outliers with a demographics-only model, which performed worse than our overall model, suggests that the accurate estimation was not driven primarily by patient size (e.g., body surface area). Similarly, wide dynamic range of the training set—nearly double that of the test set—of 146.5 mL may explain the lower

performance therein and the discrepancy observed in this random seed. From the residual errors in the regression plot shown in Figure 18, our model also had comparable estimation of high and low SVs: a well-known limitation of ML approaches that cleverly estimate the mean to reduce error. However, there was a slightly better performance at lower SV, most likely due to a greater number of datapoints with similar target values. Additionally, in our training set there were again fewer datapoints near the highest SVs which lead to the greatest error when estimating them and potentially explains the difference between the good training but strong testing performance. Therefore, increasing the number of datapoints with an emphasis on those exhibiting the boundaries of SV should improve estimation performance and overall model robustness.

Nevertheless, using wearable signal features to accurately estimate SV across a heterogeneous population of patients with CHD, suggests that eventually SCG signals can assist in overall diagnostics—previously not demonstrated in SCG literature.

5.4.2 Cardiomechanical SCG Features Improve Model Estimation

As shown in Table 6, adding the cardiomechanical SCG features to the purely electrical ECG model resulted in a modest improvement in performance that reduced the percent error from 31% to 28%, which was sufficient to achieve accurate SV estimation per CO measurement guidelines. Although the heart is electrically activated, it remains a mechanical pump and therefore assessing these other aspects of cardiac health—though traditionally ignored by NICCOM methods—are essential to quantifying its mechanical function. Specifically, while HR is well known to exhibit a strong correlation to SV, the other most important features essential to achieving a good estimation were the PEP, VET,

and PEP/VET [124], [125]. The PEP—a combination of the intrinsic electromechanical delay and isovolumic contraction time—was our second most important feature. This is in accordance with established knowledge that the PEP can vary based on age, between infancy and puberty, and differences in contractility and preload—both captured in our dataset [126]. Similarly, the VET—the time it takes to eject the SV of blood out the aorta—is related to SV [124], [126]. In addition, several NICCOM technologies utilize the impedance cardiogram to estimate SV through mathematical formulas—grounded in well understood relationships between bioimpedance and CO [37]—and leverage the VET as a strong correlate to SV. However, bioimpedance inconveniently requires multiple electrodes to be placed on the body, while SCG can capture the same VET in a significantly more convenient manner simply through an accelerometer placed on the chest. Additionally, their ratio (i.e., PEP/VET) has been demonstrated to be inversely related to contractility and helpful in determining heart failure [127]. This relationship is understood to be due to the greater amount of time required for the failing heart to build up the pressure necessary for ejection—related to PEP—and the smaller stroke volume ejected during a shorter VET [127].

Though the ECG features had a more significant independent contribution in estimating baseline SV, the SCG signal has been shown to better capture longitudinal changes in ventricular function by assessing the mechanical aspects of cardiac health [39], [40]. Nonetheless, given the complex determinants of SV, it is not surprising that combining features from multiple sensing modalities was necessary to create the holistic model that had the greatest performance.

5.4.3   *Demographic Based Correlations to SV Do Not Necessarily Generalize*

Demographic feature models (i.e., those using age and body surface area) did not generalize well to our held-out test set. Typically, body surface area is known to be well correlated to CO—especially in this population with significant age and developmental size differences [121]. However, although these demographic feature models substantially improved training set performance, these improvements did not translate to the test set. This inability to generalize well in cases when the conventional trend between SV and demographics may not be observed [128], suggests that the proper physiological data in waveform format is necessary for the robust estimation of SV. Overall, demographics may be misleading—especially in populations presenting with the unique anatomies and extreme physiologies typical to those with underlying CHD. Regardless, with an increasing number of datapoints the contribution of these demographic features should be utilized for a similar diagnostic application. Specifically, given our accurate SV estimation and the available wearable HR, these demographic characteristics can clearly be incorporated, if the body surface area is correlated to SV, to compute cardiac index, which is commonly used in pediatric cardiology to assess adequacy of oxygen delivery.

5.4.4   *SV Estimation is Robust Against Anatomical Differences*

Largely, our data suggest that accurate SV estimation can be achieved regardless of the unique anatomies and physiologies in patients with CHD. Although there are considerable anatomical modifications between single-ventricle and two-ventricle patients, it has previously been shown that there are no distinguishable differences in their SV estimation before and after the hemi-Fontan operation when using magnetic resonance imaging [129]. In addition, due to their wide-ranging diagnoses and demographics, the intersubject variability in the single-ventricle patients may have overshadowed their population

variability with respect to the two-ventricle patients. In future studies, to accurately determine whether any anatomical-induced modulation in SCG morphology exists, data should be taken from a larger and more homogenous single-ventricle population; for instance, reducing the age gap to only neonates with single- and two-ventricles.

Eventually, remote monitoring of the growing population of older children and adults with heart defects appears to be more feasible due to their uncoupled characteristics with respect to this novel sensing modality and key hemodynamic parameters of ventricular function such as SV.

5.4.5 Study Limitations

This study has limitations related to both the technologies utilized and the patient population studied. The wearable biosensor is not MRI safe and thus simultaneous measurement of CMR flows and volumetrics with ECG and SCG was not possible. Thus, to mitigate this limitation we obtained the wearable measurements as soon as possible before and after the CMR scan and after the patient was under anesthesia for those getting the CMR with anesthesia. However, it is possible that the patient was in different physiologic states during the CMR as compared to when the wearable measurements were taken.

To acquire reliable sternum PPG signals is exceptionally challenging due to issues facing significantly lower perfusion and greater skin melanin content when compared to conventionally used peripheral sites, differences in chest contours, the influence of body hair, and lower accuracy when using reflective PPG. Over the course of this study, our mechanical design was modified to include a spring-loaded mechanism. This provided the

necessary backing force for the sensors required to obtain the PPG and allowed for a constant pressure, with a modular range, to be applied—resulting in a significant improvement in PPG signal quality. Unfortunately, PPG features could not be reliably extracted from enough patients, which created an imbalance in model feature sets, and so these signals were not utilized. Nonetheless, we believe that features from the PPG signal such as pulse transit time—a measure of arterial stiffness and surrogate of BP—would reasonably add another key modality of sensing to assess SV and CO, as demonstrated in prior work [130].

Finally, though high-fidelity wearable measurements were acquired and only few minutes of data collection were necessary for this work, the wearable biosensor still needs further miniaturization to be used in future longitudinal studies in a pediatric population. However, given the considerably smaller footprint of the internal essential sensing elements, the hardware could readily be miniaturized and exploit the advent of flexible electronics which can offer a low-profile, less obtrusive solution for even greater convenience when performing longitudinal monitoring [117].

5.5   Conclusion

We demonstrated that a multimodal wearable biosensor that measures both SCG and ECG signals can accurately estimate SV in patients with CHD. In the future, this work could be expanded to monitor patients conveniently and longitudinally either post-surgery or from the comfort of their homes. Noninvasive, continuous monitoring of SV using a wearable biosensor equips clinicians with the tools necessary to track their patients longitudinally—not currently captured by any clinical program and seldom studied—

which is essential to comprehend the lifetime complications facing this growing population. Eventually, advanced ML algorithms may even be capable of predicting the periodic decompensations of patients with CHD. In addition, it is well known that there are racial, socioeconomic, and geographic factors that contribute to disturbing health disparities in CHD mortality [131]. Ultimately, following further studies in a larger population, an inexpensive ECG and SCG wearable biosensor may provide accurate, low-user-input SV monitoring in a noninvasive, continuous, and affordable manner for patients in out-of-office settings in low resource settings.

CHAPTER 6.   CONCLUSION AND FUTURE WORK

6.1   Conclusion

Collectively, this dissertation lays the groundwork for quantifying vital hemodynamic parameters, such as BP and SV, using noninvasive cardiomechanical signals—the SCG and PPG. First, we developed and validated a watch that can estimate BP without the use of a cuff in an uncontrolled, at-home setting. Then, we demonstrated the efficacy of this method for noninvasive, cuff-less BP estimation in a medically underserved population. Finally, we elucidated the ability of features derived from these wearable signals to estimate SV in patients with CHD. More importantly, the work herein determined that these multimodal sensing methods uphold their accuracy when used in populations of persons unsupervised at home, those with darker skin tones and high BMI, and pediatric patients with structural heart defects—all for whom these approaches may be the most difficult to utilize but also the most valuable. To have evaluated the feasibility of these novel techniques in these diverse populations represents a significant step toward the translation of wearable multimodal sensing for convenient longitudinal monitoring. Specifically, these advancements have both broader impacts—toward health equity and affordable monitoring for persons in MUAs using wearable devices—and intellectual merit—from understanding the limitations of these systems and development of novel methods used to mitigate them.

6.2   Future Work

For BP estimation, future work should assess the longevity of PTT-BP calibration measurements to determine the gravity of the cost associated with recalibration.

Furthermore, automated algorithms to classify activities of daily living and autonomic state—using the on-board accelerometer, gyroscope, pressure sensor, and heart rate sensing—should be incorporated to determine optimal periods for calibration measurements with a wide dynamic range in physiological values. In addition, the use of PTT alone to estimate BP may not suffice in all contexts and persons, and therefore, other signal features such as the dicrotic notch and features from the derivatives should be extracted to help design robust BP estimation models. Meanwhile, the ability of wearable PTT to act as a conveniently acquired, longitudinal biomarker of arterial stiffness should be examined in persons who are at risk of developing peripheral arterial disease, atherosclerosis, etc. Hardware should be refined by leveraging the advent of flexible electronics to create more conformal devices for comfortable longitudinal monitoring. Furthermore, hardware can be optimized for greater Sternum PPG signal quality which can then be evaluated for its ability to estimate BP and SV from a more advantageous central location. Monitoring from a more central body site may suffer less from confounding vasomotor tone effects than the periphery and can double as an efficient means to collect continuous ECG and SCG data for studying the holistic dynamics of hemodynamic parameters. In addition, hardware that enables continuous PTT measurements may act as a convenient and attainable surrogate can be used for monitoring during sleep when obtaining BP is more challenging.

For SV estimation, longitudinal SCG signals should be captured along with concurrent clinical markers of low CO to assess whether continuous monitoring of the changes, in the features extracted or signals themselves, are correlated to variations in clinical target variables. If such longitudinal estimation is accurate, then SCG signals may be used as a

convenient approach for monitoring SV bedside or at home without the need for a gold-standard. Then, time-series modeling using ML techniques such as recurrent neural networks can be used to build predictive models to forecast exacerbations in clinical status and guide intervention. SCG signals themselves should be captured in a more homogenous population of neonates with single ventricles to assess if there are truly any distinctive differences in their signal morphology. If differences are captured, such a dataset could be combined with finite element modeling and system identification approaches to help elucidate the origin and propagation mechanics behind the SCG signal, improving our understanding and ability to effectively use this novel cardiomechanical signal.

6.3   Potential Impact of This Work

To effectively handle increasing global life-expectancy, the efficiency of healthcare must improve, which will hinge upon leveraging technological advancements for remote health monitoring in outpatient settings. The development and validation of the wearable cardiomechanical sensing systems in this dissertation are a logical next step in this direction toward convenient and efficient remote monitoring. Furthermore, there are several exciting avenues of research which can now stem from the work herein. Most importantly, these wearable, multimodal methodologies can now confidently continue to be studied due to the promise demonstrated in accurately estimating hemodynamic parameters in uncontrolled settings and diverse and diseased populations. Specifically, research can progress toward cuff-less, ambulatory BP estimation in medically underserved populations where calibration requirements are reduced by using both demographics to determine subject-specific constants related to arterial stiffness (i.e., K_1) and physiological measures acquired during low-power operational modes to select salient calibration points. In addition, with

the understanding that the SCG can be conveniently employed to estimate SV in patients with structural heart defects, continuous SV and CO estimation—whether it be bedside or in outpatient settings—holds promise in monitoring neonates with single ventricles post-surgery to predict LCOS. Together, our efforts in demonstrating the feasibility of noninvasive and convenient methods for monitoring BP and SV, may deliver a means to longitudinally track the health of underserved populations for whom these approaches may be the most impactful.

REFERENCES

[1]   "WHO | Global Health Estimates," *WHO*, 2018.

[2]   S. S. Virani *et al.*, "Heart disease and stroke statistics—2020 update: A report from the American Heart Association," *Circulation*. Lippincott Williams and Wilkins, pp. E139–E596, 2020.

[3]   A. Arrieta, J. R. Woods, N. Qiao, and S. J. Jay, "Cost-benefit analysis of home blood pressure monitoring in hypertension diagnosis and treatment: An insurer perspective," *Hypertension*, vol. 64, no. 4, pp. 891–896, Oct. 2014.

[4]   W. B. White, N. Ghuman, and P. Campbell, "Role of ambulatory and home blood pressure recording in clinical practice," *Current Cardiology Reports*, vol. 11, no. 6. NIH Public Access, pp. 414–421, Nov-2009.

[5]   S. A. Yarows and J. A. Staessen, "How to use home blood pressure monitors in clinical practice.," *Am. J. Hypertens.*, vol. 15, no. 1 Pt 1, pp. 93–6, Jan. 2002.

[6]   J. I. E. Hoffman, "The global burden of congenital heart disease," *Cardiovascular Journal of Africa*, vol. 24, no. 4. Clinics Cardive Publishing (Pty) Ltd., pp. 141–145, May-2013.

[7]   C. D. Ndumele, H. J. Baer, S. Shaykevich, S. R. Lipsitz, and L. S. Hicks, "Cardiovascular disease and risk in primary care settings in the United States," *Am. J. Cardiol.*, vol. 109, no. 4, pp. 521–526, Feb. 2012.

[8]   P. Muntner *et al.*, "Trends in blood pressure control among US adults with hypertension, 1999-2000 to 2017-2018," *JAMA - J. Am. Med. Assoc.*, vol. 324, no. 12, pp. 1190–1200, Sep. 2020.

[9]   D. Zhou, B. Xi, M. Zhao, L. Wang, and S. P. Veeranki, "Uncontrolled hypertension increases risk of all-cause and cardiovascular disease mortality in US adults: The NHANES III Linked Mortality Study," *Sci. Rep.*, vol. 8, no. 1, p. 9418, Dec. 2018.

[10]   S. K. Doyle, A. M. Chang, P. Levy, and K. L. Rising, "Achieving Health Equity in Hypertension Management Through Addressing the Social Determinants of Health," *Current Hypertension Reports*, vol. 21, no. 8. Current Medicine Group

LLC 1, pp. 1–6, 01-Aug-2019.

[11]   J. K. Triedman and J. W. Newburger, "Trends in congenital heart disease," *Circulation*, vol. 133, no. 25, pp. 2716–2733, Jun. 2016.

[12]   O. T. Inan *et al.*, "Digitizing clinical trials," *npj Digit. Med.*, vol. 3, no. 1, p. 20, Dec. 2020.

[13]   A. L. Siu, "Screening for High Blood Pressure in Adults: U.S. Preventive Services Task Force Recommendation Statement," *Ann. Intern. Med.*, vol. 163, no. 10, p. 778, Nov. 2015.

[14]   M. Sharma *et al.*, "Cuff-Less and Continuous Blood Pressure Monitoring: A Methodological Review," *Technologies*, vol. 5, no. 2, p. 21, May 2017.

[15]   T. Arakawa, "Recent research and developing trends of wearable sensors for detecting blood pressure," *Sensors (Switzerland)*, vol. 18, no. 9. MDPI AG, 01-Sep-2018.

[16]   K. Kario, D. Shimbo, N. Tomitani, H. Kanegae, J. E. Schwartz, and B. Williams, "The first study comparing a wearable watch-type blood pressure monitor with a conventional ambulatory blood pressure monitor on in-office and out-of-office settings," *J. Clin. Hypertens.*, vol. 22, no. 2, pp. 135–141, Feb. 2020.

[17]   D. M. Bard, J. I. Joseph, and N. van Helmond, "Cuff-Less Methods for Blood Pressure Telemonitoring," *Front. Cardiovasc. Med.*, vol. 6, Apr. 2019.

[18]   R. Mukkamala *et al.*, "Toward Ubiquitous Blood Pressure Monitoring via Pulse Transit Time: Theory and Practice," *IEEE Trans. Biomed. Eng.*, vol. 62, no. 8, pp. 1879–1901, 2015.

[19]   M. Etemadi and O. T. Inan, "Wearable ballistocardiogram and seismocardiogram systems for health and performance," *Journal of Applied Physiology*, vol. 124, no. 2. American Physiological Society, pp. 452–461, 01-Feb-2018.

[20]   T. H. Huynh, R. Jafari, and W. Y. Chung, "Noninvasive cuffless blood pressure estimation using pulse transit time and impedance plethysmography," *IEEE Trans. Biomed. Eng.*, vol. 66, no. 4, pp. 967–976, Apr. 2019.

[21]   A. A. Bove *et al.*, "Reducing cardiovascular disease risk in medically underserved urban and rural communities," *Am. Heart J.*, vol. 161, no. 2, pp. 351–359, Feb. 2011.

[22]   K. D. Lincoln, C. M. Abdou, and D. Lloyd, "Race and socioeconomic differences in obesity and depression among black and non-hispanic White Americans," *J. Health Care Poor Underserved*, vol. 25, no. 1, pp. 257–275, Feb. 2014.

[23]   "Racial Disparities in Hypertension Prevalence and Management: A Crisis Control? - American College of Cardiology." [Online]. Available: https://www.acc.org/latest-in-cardiology/articles/2020/04/06/08/53/racial-disparities-in-hypertension-prevalence-and-management. [Accessed: 11-Nov-2020].

[24]   D. T. Lackland, "Racial differences in hypertension: Implications for high blood pressure management," in *American Journal of the Medical Sciences*, 2014, vol. 348, no. 2, pp. 135–138.

[25]   H. JI and K. S, "The incidence of congenital heart disease," *J. Am. Coll. Cardiol.*, vol. 39, no. 12, pp. 1890–1900, Jun. 2002.

[26]   M. E. Oster, K. A. Lee, M. A. Honein, T. Riehle-Colarusso, M. Shin, and A. Correa, "Temporal Trends in Survival Among Infants With Critical Congenital Heart Defects," *Pediatrics*, vol. 131, no. 5, pp. e1502–e1508, May 2013.

[27]   M. M, G. K, A. CK, M. JE, and J. KJ, "Causes of death after congenital heart surgery," *Ann. Thorac. Surg.*, vol. 83, no. 4, pp. 1438–1445, Apr. 2007.

[28]   L. J. Burchill *et al.*, "Hospitalization Trends and Health Resource Use for Adult Congenital Heart Disease–Related Heart Failure," *J. Am. Heart Assoc.*, vol. 7, no. 15, Aug. 2018.

[29]   I. Klem *et al.*, "Prognostic Value of Routine Cardiac Magnetic Resonance Assessment of Left Ventricular Ejection Fraction and Myocardial Damage," *Circ. Cardiovasc. Imaging*, vol. 4, no. 6, pp. 610–619, Nov. 2011.

[30]   A. O. Abualsaud *et al.*, "Cardiac output as a predictor in congenital heart disease: Are we stating the obvious?," *Int. J. Cardiol.*, vol. 210, pp. 143–148, May 2016.

[31]   A. M. Valente *et al.*, "Contemporary predictors of death and sustained ventricular

tachycardia in patients with repaired tetralogy of Fallot enrolled in the INDICATOR cohort," *Heart*, vol. 100, no. 3, pp. 247–253, Feb. 2014.

[32] A. F. Connors *et al.*, "The effectiveness of right heart catheterization in the initial care of critically ill patients," *J. Am. Med. Assoc.*, vol. 276, no. 11, pp. 889–897, Sep. 1996.

[33] M. K. Kerstens, M. Wijnberge, B. F. Geerts, A. P. Vlaar, and D. P. Veelo, "Netherlands Journal of Critical Care Non-invasive cardiac output monitoring techniques in the ICU," 2018.

[34] F. Grothues *et al.*, "Comparison of interstudy reproducibility of cardiovascular magnetic resonance with two-dimensional echocardiography in normal subjects and in patients with heart failure or left ventricular hypertrophy," *Am. J. Cardiol.*, vol. 90, no. 1, pp. 29–34, Jul. 2002.

[35] B. Saugel, M. Cecconi, J. Y. Wagner, and D. A. Reuter, "Noninvasive continuous cardiac output monitoring in perioperative and intensive care medicine," *Br. J. Anaesth.*, vol. 114, pp. 562–575, 2015.

[36] W. G. Kubicek, J. N. Karnegis, R. P. Patterson, D. A. Witsoe, and R. H. Mattson, "Development and evaluation of an impedance cardiac output system.," *Aerosp. Med.*, vol. 37, no. 12, pp. 1208–1212, Dec. 1966.

[37] D. P. Bernstein and H. J. M. Lemmens, "Stroke volume equation for impedance cardiography," *Med. Biol. Eng. Comput.*, vol. 43, no. 4, pp. 443–450, Jul. 2005.

[38] K. H. Wesseling, J. R. C. Jansen, J. J. Settels, and J. J. Schreuder, "Computation of aortic flow from pressure in humans using a nonlinear, three-element model," *J. Appl. Physiol.*, vol. 74, no. 5, pp. 2566–2573, 1993.

[39] B. Semiz *et al.*, "Non-Invasive Wearable Patch Utilizing Seismocardiography for Peri-Operative Use in Surgical Patients," *IEEE J. Biomed. Heal. Informatics*, vol. PP, pp. 1–1, Oct. 2020.

[40] O. T. Inan *et al.*, "Novel Wearable Seismocardiography and Machine Learning Algorithms Can Assess Clinical Status of Heart Failure Patients," *Circ. Heart Fail.*, vol. 11, no. 1, p. e004313, Jan. 2018.

[41] A. Akhbardeh *et al.*, "Comparative analysis of three different modalities for characterization of the seismocardiogram," in *Proceedings of the 31st Annual International Conference of the IEEE Engineering in Medicine and Biology Society: Engineering the Future of Biomedicine, EMBC 2009*, 2009, vol. 2009, pp. 2899–2903.

[42] "CV Physiology | Arterial Blood Pressure." [Online]. Available: https://www.cvphysiology.com/Blood Pressure/BP002. [Accessed: 13-Nov-2021].

[43] M. M. H. Shandhi *et al.*, "Wearable Patch-Based Estimation of Oxygen Uptake and Assessment of Clinical Status during Cardiopulmonary Exercise Testing in Patients With Heart Failure: Wearable Monitoring of Cardiovascular Health in Heart Failure Patients," *J. Card. Fail.*, Nov. 2020.

[44] A. Reisner, P. A. Shaltis, D. McCombie, and H. H. Asada, "Utility of the Photoplethysmogram in Circulatory Monitoring," *Anesthesiology*, vol. 108, no. 5, pp. 950–958, May 2008.

[45] A. M. Carek, J. Conant, A. Joshi, H. Kang, and O. T. Inan, "SeismoWatch," *Proc. ACM Interactive, Mobile, Wearable Ubiquitous Technol.*, vol. 1, no. 3, pp. 1–16, Sep. 2017.

[46] A. M. Carek and O. T. Inan, "Robust Sensing of Distal Pulse Waveforms on a Modified Weighing Scale for Ubiquitous Pulse Transit Time Measurement," *IEEE Trans. Biomed. Circuits Syst.*, vol. 11, no. 4, pp. 765–772, Aug. 2017.

[47] M. Etemadi, O. T. Inan, J. A. Heller, S. Hersek, L. Klein, and S. Roy, "A Wearable Patch to Enable Long-Term Monitoring of Environmental, Activity and Hemodynamics Variables," *IEEE Trans. Biomed. Circuits Syst.*, vol. 10, no. 2, pp. 280–288, Apr. 2016.

[48] G. G. Berntson *et al.*, "Heart rate variability: Origins methods, and interpretive caveats," *Psychophysiology*, vol. 34, no. 6. Blackwell Publishing Inc., pp. 623–648, 1997.

[49] M. M. H. Shandhi, B. Semiz, S. Hersek, N. Goller, F. Ayazi, and O. Inan, "Performance Analysis of Gyroscope and Accelerometer Sensors for Seismocardiography-Based Wearable Pre-Ejection Period Estimation.," *IEEE J. Biomed. Heal. informatics*, Jan. 2019.

[50]   H. Ashouri, S. Hersek, and O. T. Inan, "Universal Pre-Ejection Period Estimation Using Seismocardiography: Quantifying the Effects of Sensor Placement and Regression Algorithms," *IEEE Sens. J.*, vol. 18, no. 4, pp. 1665–1674, Feb. 2018.

[51]   E. Casiglia, V. Tikhonoff, F. Albertini, and P. Palatini, "Poor Reliability of Wrist Blood Pressure Self-Measurement at Home: A Population-Based Study," *Hypertension*, vol. 68, no. 4, pp. 896–903, Oct. 2016.

[52]   O. T. Inan, G. T. A. Kovacs, and L. Giovangrandi, "Evaluating the lower-body electromyogram signal acquired from the feet as a noise reference for standing ballistocardiogram measurements," *IEEE Trans. Inf. Technol. Biomed.*, vol. 14, no. 5, pp. 1188–1196, Sep. 2010.

[53]   "1708-2014 - IEEE Standard for Wearable Cuffless Blood Pressure Measuring Devices." [Online]. Available: https://standards.ieee.org/standard/1708-2014.html. [Accessed: 24-Jun-2020].

[54]   E. Świerblewska *et al.*, "An independent relationship between muscle sympathetic nerve activity and pulse wave velocity in normal humans," *J. Hypertens.*, vol. 28, no. 5, pp. 979–984, May 2010.

[55]   L. Faconti, B. Farukh, R. McNally, A. Webb, and P. Chowienczyk, "Arterial Stiffness Can Be Modulated by Pressure-Independent Mechanisms in Hypertension," *J. Am. Heart Assoc.*, vol. 8, no. 15, Aug. 2019.

[56]   C. Yang and N. Tavassolian, "Pulse transit time measurement using seismocardiogram, photoplethysmogram, and acoustic recordings: Evaluation and comparison," *IEEE J. Biomed. Heal. Informatics*, vol. 22, no. 3, pp. 733–740, May 2018.

[57]   M. Gao, N. B. Olivier, and R. Mukkamala, "Comparison of noninvasive pulse transit time estimates as markers of blood pressure using invasive pulse transit time measurements as a reference," *Physiol. Rep.*, vol. 4, no. 10, May 2016.

[58]   M. D. Sinha, J. A. Gilg, L. Kerecuk, and C. J. D. Reid, "Progression to hypertension in non-hypertensive children following renal transplantation," *Nephrol. Dial. Transplant.*, vol. 27, no. 7, pp. 2690–2696, Jul. 2012.

[59]   M. Yavarimanesh, A. Chandrasekhar, J.-O. Hahn, and R. Mukkamala, "Commentary: Relation Between Blood Pressure and Pulse Wave Velocity for

Human Arteries," *Front. Physiol.*, vol. 10, no. SEP, p. 1179, Sep. 2019.

[60]   Y. Ma *et al.*, "Relation between blood pressure and pulse wave velocity for human arteries," *Proc. Natl. Acad. Sci. U. S. A.*, vol. 115, no. 44, pp. 11144–11149, Oct. 2018.

[61]   J. S. Zia, J. Kimball, S. Hersek, M. M. H. Shandhi, B. Semiz, and O. T. Inan, "A Unified Framework for Quality Indexing and Classification of Seismocardiogram Signals," *IEEE J. Biomed. Heal. Informatics*, vol. 24, no. 4.

[62]   V. Hartmann, H. Liu, F. Chen, Q. Qiu, S. Hughes, and D. Zheng, "Quantitative Comparison of Photoplethysmographic Waveform Characteristics: Effect of Measurement Site," *Front. Physiol.*, vol. 10, no. MAR, p. 198, Mar. 2019.

[63]   H. Beyhaghi and A. J. Viera, "Comparative Cost-Effectiveness of Clinic, Home, or Ambulatory Blood Pressure Measurement for Hypertension Diagnosis in US Adults: A Modeling Study," *Hypertension*, vol. 73, no. 1, pp. 121–131, 2019.

[64]   G. S. Stergiou *et al.*, "Reproducibility of home, ambulatory, and clinic blood pressure: implications for the design of trials for the assessment of antihypertensive drug efficacy," *Am. J. Hypertens.*, vol. 15, no. 2, pp. 101–104, Feb. 2002.

[65]   V. G. Ganti, A. Carek, B. N. Nevius, J. Heller, M. Etemadi, and O. Inan, "Wearable Cuff-less Blood Pressure Estimation at Home via Pulse Transit Time," *IEEE J. Biomed. Heal. Informatics*, pp. 1–1, Sep. 2020.

[66]   G. Parati, R. Casadei, A. Groppelli, M. Di Rienzo, and G. Mancia, "Comparison of finger and intra-arterial blood pressure monitoring at rest and during laboratory testing," *Hypertension*, vol. 13, no. 6 I, pp. 647–655, 1989.

[67]   K. H. Wesseling, de B. Wit, van der G.M.A. Hoeven, van J. Goudoever, and J. J. Settels, "Physiocal, calibrating finger vascular physiology for finapres," *Homeost. Heal. Dis.*, vol. 36, no. 2–3, pp. 67–82, 1995.

[68]   K. Chachula, F. Lieb, F. Hess, J. Welter, N. Graf, and A. Dullenkopf, "Non-invasive continuous blood pressure monitoring (ClearSight^{TM} system) during shoulder surgery in the beach chair position: a prospective self-controlled study," *BMC Anesthesiol.*, vol. 20, no. 1, Dec. 2020.

[69]   N. Ghuman, P. Campbell, and W. B. White, "Role of ambulatory and home blood pressure recording in clinical practice," *Current Cardiology Reports*, vol. 11, no. 6. Curr Cardiol Rep, pp. 414–421, Nov-2009.

[70]   Q. Zhao *et al.*, "Reproducibility of blood pressure response to the cold pressor test," *Am. J. Epidemiol.*, vol. 176, no. SUPPL. 7, Oct. 2012.

[71]   S.-H. Tseng, A. Grant, and A. J. Durkin, "In vivo determination of skin near-infrared optical properties using diffuse optical spectroscopy," *J. Biomed. Opt.*, vol. 13, no. 1, p. 014016, 2008.

[72]   R. P. Wildman *et al.*, "Weight change is associated with change in arterial stiffness among healthy young adults," *Hypertension*, vol. 45, no. 2, pp. 187–192, Feb. 2005.

[73]   A. A. Ahimastos, M. Formosa, A. M. Dart, and B. A. Kingwell, "Gender Differences in Large Artery Stiffness Pre-and Post Puberty," *J. Clin. Endocrinol. Metab.*, vol. 88, no. 11, pp. 5375–5380, 2003.

[74]   S. Wu *et al.*, "Aging, Arterial Stiffness, and Blood Pressure Association in Chinese Adults," *Hypertension*, vol. 73, no. 4, pp. 893–899, Apr. 2019.

[75]   C. Alecu *et al.*, "Determinants of arterial stiffness in an apparently healthy population over 60 years," *J. Hum. Hypertens.*, vol. 20, no. 10, pp. 749–756, Oct. 2006.

[76]   T. Coutinho, "Arterial stiffness and its clinical implications in women," *Canadian Journal of Cardiology*, vol. 30, no. 7. Pulsus Group Inc., pp. 756–764, 2014.

[77]   A. E. Schutte, R. Kruger, L. F. Gafane-Matemane, Y. Breet, M. Strauss-Kruger, and J. K. Cruickshank, "Ethnicity and Arterial Stiffness," *Arterioscler. Thromb. Vasc. Biol.*, vol. 40, no. 5, pp. 1044–1054, May 2020.

[78]   "The Practical Guide Identification, Evaluation, and Treatment of Overweight and Obesity in Adults NHLBI Obesity Education Initiative."

[79]   X. Ding and Y. T. Zhang, "Pulse transit time technique for cuffless unobtrusive blood pressure measurement: from theory to algorithm," *Biomedical Engineering Letters*, vol. 9, no. 1. Springer Verlag, pp. 37–52, 08-Feb-2019.

[80] J. R. MacDonald, "Potential causes, mechanisms, and implications of post exercise hypotension," *Journal of Human Hypertension*, vol. 16, no. 4. Nature Publishing Group, pp. 225–236, 2002.

[81] A. C. Flint *et al.*, "Effect of Systolic and Diastolic Blood Pressure on Cardiovascular Outcomes," *N. Engl. J. Med.*, vol. 381, no. 3, pp. 243–251, Jul. 2019.

[82] W. B. Kannel, T. Gordon, and M. J. Schwartz, "Systolic versus diastolic blood pressure and risk of coronary heart disease. The Framingham study," *Am. J. Cardiol.*, vol. 27, no. 4, pp. 335–346, 1971.

[83] H. Kaneko *et al.*, "Association of Isolated Diastolic Hypertension Based on the Cutoff Value in the 2017 American College of Cardiology/American Heart Association Blood Pressure Guidelines With Subsequent Cardiovascular Events in the General Population," *J. Am. Heart Assoc.*, vol. 9, no. 19, p. e017963, Oct. 2020.

[84] M. J. Domanski, B. R. Davis, M. A. Pfeffer, M. Kastantin, and G. F. Mitchell, "Isolated systolic hypertension: Prognostic information provided by pulse pressure," *Hypertension*, vol. 34, no. 3, pp. 375–380, 1999.

[85] H. Kanegae, T. Oikawa, Y. Okawara, S. Hoshide, and K. Kario, "Which blood pressure measurement, systolic or diastolic, better predicts future hypertension in normotensive young adults?," *J. Clin. Hypertens.*, vol. 19, no. 6, pp. 603–610, Jun. 2017.

[86] S. S. Franklin *et al.*, "Does the relation of blood pressure to coronary heart disease risk change with aging?: The Framingham Heart Study," *Circulation*, vol. 103, no. 9, pp. 1245–1249, Mar. 2001.

[87] B. C. Taylor, T. J. Wilt, and H. G. Welch, "Impact of diastolic and systolic blood pressure on mortality: Implications for the definition of 'normal,'" *J. Gen. Intern. Med.*, vol. 26, no. 7, pp. 685–690, Jul. 2011.

[88] "WHO | Global action plan for the prevention and control of NCDs 2013-2020." [Online]. Available: https://www.who.int/nmh/publications/ncd-action-plan/en/. [Accessed: 08-Nov-2019].

[89] V. A. Convertino *et al.*, "Wearable Sensors Incorporating Compensatory Reserve Measurement for Advancing Physiological Monitoring in Critically Injured Trauma Patients," *Sensors*, vol. 20, no. 22, p. 6413, Nov. 2020.

[90] B. Bent, B. A. Goldstein, W. A. Kibbe, and J. P. Dunn, "Investigating sources of inaccuracy in wearable optical heart rate sensors," *npj Digit. Med.*, vol. 3, no. 1, Dec. 2020.

[91] S.-H. Tseng, P. Bargo, A. Durkin, and N. Kollias, "Chromophore concentrations, absorption and scattering properties of human skin in-vivo," *Opt. Express*, vol. 17, no. 17, p. 14599, Aug. 2009.

[92] J. Allen, "Photoplethysmography and its application in clinical physiological measurement," *Physiological Measurement*, vol. 28, no. 3. IOP Publishing, p. R1, 01-Mar-2007.

[93] C. El-Hajj and P. A. Kyriacou, "A review of machine learning techniques in photoplethysmography for the non-invasive cuff-less measurement of blood pressure," *Biomedical Signal Processing and Control*, vol. 58. Elsevier Ltd, p. 101870, 01-Apr-2020.

[94] L. Wang, W. Zhou, Y. Xing, and X. Zhou, "A novel neural network model for blood pressure estimation using photoplethesmography without electrocardiogram," *J. Healthc. Eng.*, vol. 2018, 2018.

[95] J. He, P. Muntner, J. Chen, E. J. Roccella, R. H. Streiffer, and P. K. Whelton, "Factors associated with hypertension control in the general population of the United States," *Arch. Intern. Med.*, vol. 162, no. 9, pp. 1051–1058, May 2002.

[96] S. Shea, D. Misra, M. H. Ehrlich, L. Field, and C. K. Francis, "Predisposing Factors for Severe, Uncontrolled Hypertension in an Inner-City Minority Population," *N. Engl. J. Med.*, vol. 327, no. 11, pp. 776–781, Sep. 1992.

[97] H. Komine, Y. Asai, T. Yokoi, and M. Yoshizawa, "Non-invasive assessment of arterial stiffness using oscillometric blood pressure measurement," *Biomed. Eng. Online*, vol. 11, no. 1, p. 6, Feb. 2012.

[98] D. J. Hughes, C. F. Babbs, L. A. Geddes, and J. D. Bourland, "Measurements of Young's Modulus of Elasticity of the Canine Aorta with Ultrasound," *Ultrason. Imaging*, vol. 1, no. 4, pp. 356–367, 1979.

[99] J. E. Hall, J. M. Do Carmo, A. A. Da Silva, Z. Wang, and M. E. Hall, "Obesity-Induced Hypertension: Interaction of Neurohumoral and Renal Mechanisms," *Circ. Res.*, vol. 116, no. 6, pp. 991–1006, Mar. 2015.

[100] M. AlGhatrif *et al.*, "Longitudinal trajectories of arterial stiffness and the role of blood pressure: The Baltimore longitudinal study of aging," *Hypertension*, vol. 62, no. 5, pp. 934–941, Nov. 2013.

[101] A. Scuteri *et al.*, "Associations of large artery structure and function with adiposity: Effects of age, gender, and hypertension. The SardiNIA Study," *Atherosclerosis*, vol. 221, no. 1, pp. 189–197, Mar. 2012.

[102] M. Leggio *et al.*, "The relationship between obesity and hypertension: An updated comprehensive overview on vicious twins," *Hypertension Research*, vol. 40, no. 12. Nature Publishing Group, pp. 947–963, 01-Dec-2017.

[103] S. S. Najjar *et al.*, "Pulse Wave Velocity Is an Independent Predictor of the Longitudinal Increase in Systolic Blood Pressure and of Incident Hypertension in the Baltimore Longitudinal Study of Aging," *J. Am. Coll. Cardiol.*, vol. 51, no. 14, pp. 1377–1383, Apr. 2008.

[104] J. C. Philips, M. Marchand, and A. J. Scheen, "Squatting, a posture test for studying cardiovascular autonomic neuropathy in diabetes," *Diabetes and Metabolism*, vol. 37, no. 6. pp. 489–496, 01-Dec-2011.

[105] F. Rossberg and J. Peňaz, "Initial cardiovascular response on change of posture from squatting to standing," *Eur. J. Appl. Physiol. Occup. Physiol.*, vol. 57, no. 1, pp. 93–97, 1988.

[106] S. C. Barnes, N. Ball, V. J. Haunton, T. G. Robinson, and R. B. Panerai, "The cerebrocardiovascular response to periodic squat-stand maneuvers in healthy subjects: a time-domain analysis," *Am. J. Physiol. Heart Circ. Physiol.*, vol. 313, no. 6, pp. H1240–H1248, Dec. 2017.

[107] J. Zia, J. Kimball, S. Hersek, and O. T. Inan, "Modeling Consistent Dynamics of Cardiogenic Vibrations in Low-Dimensional Subspace," *IEEE J. Biomed. Heal. Informatics*, vol. 24, no. 7, pp. 1887–1898, Jul. 2020.

[108] J. Zia, J. Kimball, and O. T. Inan, "Localizing Placement of Cardiomechanical Sensors during Dynamic Periods via Template Matching," in *2020 42nd Annual International Conference of the IEEE Engineering in Medicine & Biology Society (EMBC)*, 2020, vol. 2020-July, pp. 473–476.

[109] Guanqun Zhang, Da Xu, N. B. Olivier, and R. Mukkamala, "Pulse arrival time is

not an adequate surrogate for pulse transit time in terms of tracking diastolic pressure," in *2011 Annual International Conference of the IEEE Engineering in Medicine and Biology Society*, 2011, pp. 6462–6464.

[110] C. De Ciuceis *et al.*, "Effects of weight loss on structural and functional alterations of subcutaneous small arteries in obese patients," *Hypertension*, vol. 58, no. 1, pp. 29–36, Jul. 2011.

[111] J. Ryan, S. Edney, and C. Maher, "Anxious or empowered? A cross-sectional study exploring how wearable activity trackers make their owners feel," *BMC Psychol.*, vol. 7, no. 1, p. 42, Jul. 2019.

[112] L. A. Bove, "Continuing Education Increasing Patient Engagement Through the Use of Wearable Technology," 2019.

[113] J. Greiwe and S. M. Nyenhuis, "Wearable Technology and How This Can Be Implemented into Clinical Practice," *Current Allergy and Asthma Reports*, vol. 20, no. 8. Springer, 01-Aug-2020.

[114] K. H. Lee *et al.*, "Mechano-acoustic sensing of physiological processes and body motions via a soft wireless device placed at the suprasternal notch," *Nat. Biomed. Eng.*, vol. 4, no. 2, pp. 148–158, Feb. 2020.

[115] C. M. Boutry *et al.*, "Biodegradable and flexible arterial-pulse sensor for the wireless monitoring of blood flow," *Nat. Biomed. Eng.*, vol. 3, no. 1, pp. 47–57, Jan. 2019.

[116] C. Wang *et al.*, "Monitoring of the central blood pressure waveform via a conformal ultrasonic device," *Nat. Biomed. Eng.*, vol. 2, no. 9, pp. 687–695, Sep. 2018.

[117] T. Ha *et al.*, "A Chest-Laminated Ultrathin and Stretchable E-Tattoo for the Measurement of Electrocardiogram, Seismocardiogram, and Cardiac Time Intervals," *Adv. Sci.*, vol. 6, no. 14, p. 1900290, Jul. 2019.

[118] S. Kim *et al.*, "Influence of contact pressure and moisture on the signal quality of a newly developed textile ECG sensor shirt," *Proc. 5th Int. Work. Wearable Implant. Body Sens. Networks, BSN2008, conjunction with 5th Int. Summer Sch. Symp. Med. Devices Biosensors, ISSS-MDBS 2008*, pp. 256–259, 2008.

[119] K. Taylor, C. Manlhiot, B. McCrindle, L. Grosse-Wortmann, and H. Holtby, "Poor accuracy of noninvasive cardiac output monitoring using bioimpedance cardiography [PhysioFlow®] compared to magnetic resonance imaging in pediatric patients," *Anesth. Analg.*, vol. 114, no. 4, pp. 771–775, Apr. 2012.

[120] S. Fratz *et al.*, "Guidelines and protocols for cardiovascular magnetic resonance in children and adults with congenital heart disease: SCMR expert consensus group on congenital heart disease," *J. Cardiovasc. Magn. Reson.*, vol. 15, no. 1, 2013.

[121] B. W. Jegier, P. Sekelj, P. A. M Auld, R. Simpson, and M. McGREGOR, "THE RELATION BETWEEN CARDIAC OUTPUT AND BODY SIZE*," *Hear. J first*, vol. 25, 1963.

[122] L. A. H. Critchley and J. A. J. H. Critchley, "A meta-analysis of studies using bias and precision statistics to compare cardiac output measurement techniques," *J. Clin. Monit. Comput.*, vol. 15, no. 2, pp. 85–91, 1999.

[123] P. J. Peyton and S. W. Chong, "Minimally Invasive Measurement of Cardiac Output during Surgery and Critical CareA Meta-analysis of Accuracy and Precision," *Anesthesiology*, vol. 113, no. 5, pp. 1220–1235, Nov. 2010.

[124] A. M. Weissler, R. G. Peeler, and W. H. Roehll, "Relationships between left ventricular ejection time, stroke volume, and heart rate in normal individuals and patients with cardiovascular disease," *Am. Heart J.*, vol. 62, no. 3, pp. 367–378, Sep. 1961.

[125] P. Winberg and U. Ergander, "Relationship between Heart Rate, Left Ventricular Output, and Stroke Volume in Preterm Infants during Fluctuations in Heart Rate," *Pediatr. Res. 1992 312*, vol. 31, no. 2, pp. 117–120, 1992.

[126] R. P. Lewis, S. E. Rittgers, W. F. Forester, and H. Boudoulas, "REVIEWS OF CONTEMPORARY LABORATORY METHODS A Critical Review of the Systolic Time Intervals."

[127] J. D. Bonagura and V. L. Fuentes, "Echocardiography," *Small Anim. Diagnostic Ultrasound*, pp. 217–331, Jan. 2014.

[128] M. D. Vriesendorp *et al.*, "The clinical implications of body surface area as a poor proxy for cardiac output," *https://doi.org/10.1080/24748706.2021.1968089*, Aug. 2021.

[129]   H. R. Bellsham-Revell *et al.*, "Serial Magnetic Resonance Imaging in Hypoplastic Left Heart Syndrome Gives Valuable Insight Into Ventricular and Vascular Adaptation," *J. Am. Coll. Cardiol.*, vol. 61, no. 5, p. 561, Feb. 2013.

[130]   Y. Yao *et al.*, "Unobtrusive Estimation of Cardiovascular Parameters with Limb Ballistocardiography," *Sensors (Basel).*, vol. 19, no. 13, Jul. 2019.

[131]   J. R. Kaltman, K. M. Burns, G. D. Pearson, D. C. Goff, and F. Evans, "Disparities in Congenital Heart Disease Mortality Based on Proximity to a Specialized Pediatric Cardiac Center," *Circulation*. Lippincott Williams and Wilkins, pp. 1034–1036, 24-Mar-2020.